Marine Stratocumulus Convection

Wayne H. Schubert
Joseph S. Wakefield
Ellen J. Steiner
Stephen K. Cox

Department of Atmospheric Science
Colorado State University
Fort Collins, Colorado

Colorado State University

Department of Atmospheric Science

Paper No. 273

MARINE STRATOCUMULUS CONVECTION

Wayne H. Schubert
Joseph S. Wakefield
Ellen J. Steiner
Stephen K. Cox

The research reported here has been supported by the GARP Section of the Office of Climate Dynamics, National Science Foundation Grant ATM 76-09370

Department of Atmospheric Science
Colorado State University
Fort Collins, Colorado 80523

July 1977

Atmospheric Science Paper No. 273

CONTENTS

ABSTRACT

Large areas of persistent low level marine stratocumulus clouds occur primarily over the cool eastern oceans in the strong subsidence to the east of the subtropical oceanic high pressure cells. The climatology of these areas is reviewed, after which we present a coupled convective-radiative boundary layer model of such stratocumulus convection. The model, which is a slight generalization of the cloud-topped mixed layer model of Lilly (1968), has as dependent variables the cloud top height, cloud base height, mixed layer moist static energy and total water content, the turbulent fluxes of moist static energy and total water, the cloud top jumps of moist static energy and total water, the cloud top temperature and the cloud top jump in net radiative flux. Assuming horizontally homogeneous steady state conditions we first investigate the dependence of the model variables on the large-scale divergence and sea surface temperature. Next, assuming horizontally inhomogeneous conditions we investigate by numerical integration the downstream variations which occur as boundary layer air flows through regions of varying divergence and sea surface temperature. In addition, approximate analytic solutions are given. Finally, the design of an observational program to more completely test the theory is briefly discussed.

1. Introduction

In tropical and subtropical latitudes there exists a subtype of dry climate called the cool coastal dry climate, which is classified in Köppen symbols as Bn, with the n signifying frequent fog (Nebel in German). Bn deserts are typically characterized by intense aridity, small annual and diurnal temperature ranges and high frequences of fog and low stratus. The distribution of these cool coastal dry climates is shown in figure 1. All five are bordered by cool ocean currents with upwelling. The five regions, their desert names, and the bordering ocean currents are listed in Table 1. Figure 2 shows the four year

TABLE 1. The five principal cool coastal dry climates, their accompanying desert names, and their bordering cool ocean currents.

Region	Desert	Ocean Current
Coastal California and Mexico	Sonoran	California
Coastal Equador, Peru and Chile	Peru and Atacama	Peru or Humboldt
Coastal northwestern Africa	Sahara	Canaries
Coastal southwestern Africa	Namib	Benguela
Coastal northeastern Africa	Somali	Somali

mean (1967-70) January relative cloud cover (Miller and Feddes, 1971). Figure 3 shows the same field for July. Figures 2 and 3 indicate that the Bn deserts lie primarily on the borders of extensive stratocumulus regimes which occupy the strong subsidence regions to the east of the subtropical oceanic high pressure cells.[1] The persistent low level stratocumulus clouds occupy large portions of the eastern Pacific and eastern Atlantic Oceans but apparently only a small portion of the

[1]Coastal northeastern Africa is the exception.

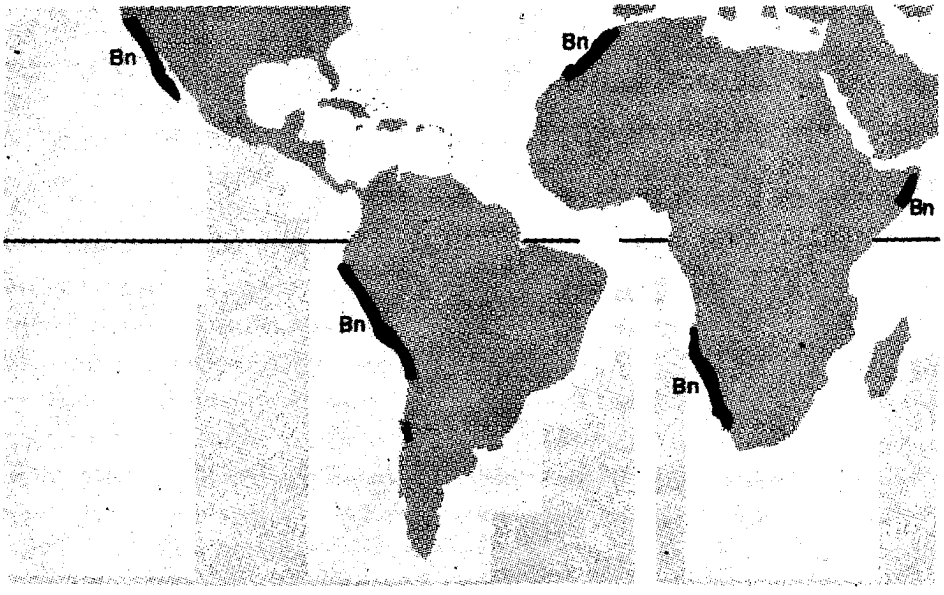

Figure 1. Distribution of the five principal cool coastal dry climates (Bn). After Trewartha (1968).

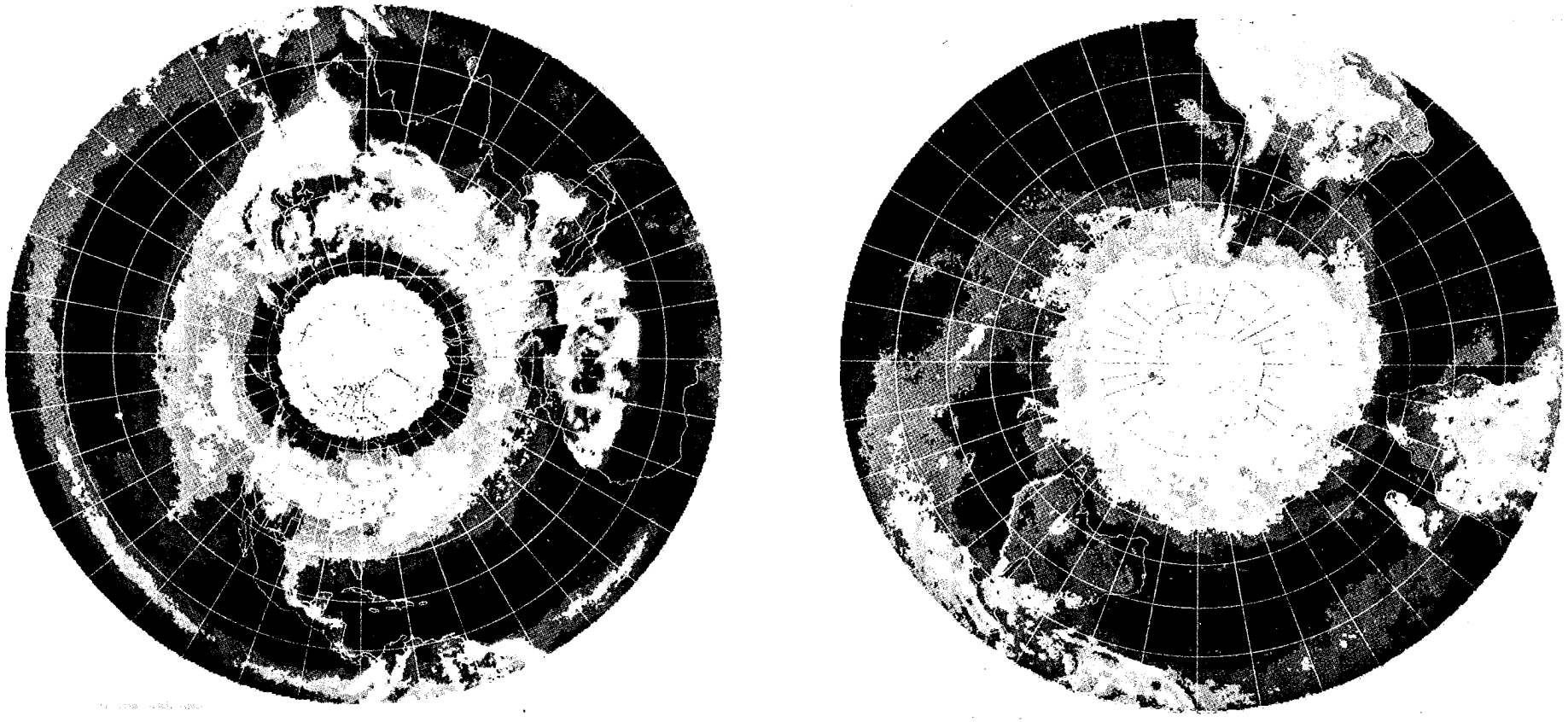

Figure 2. Mean January relative cloud cover (from Miller and Feddes, 1971).

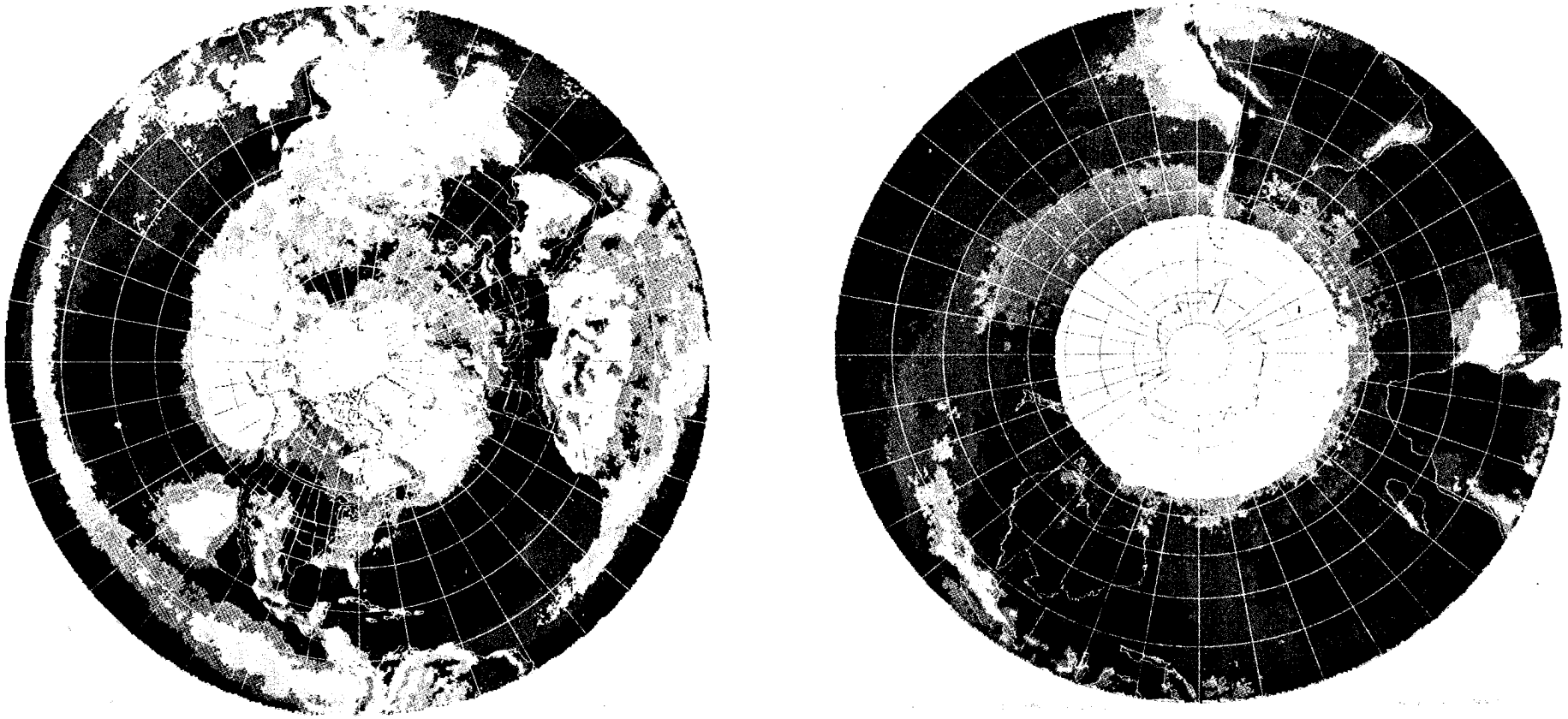

Figure 3. Mean July relative cloud cover (from Miller and Feddes, 1971).

western Indian Ocean. These areas of marine stratocumulus convection are most extensive in the northern hemisphere summer, when the upward motion in the ITCZ and the downward motion in the subtropical highs is strongest. Let us now examine each of these areas in more detail.

1.1 Coastal Oregon, California and Mexico

In Table 2 we present precipitation data for coastal Oregon, California and Mexico between about 46°N and 15°N. The most arid station in an annual sense is Ensenada with 161 mm. North of Ensenada all stations show little summertime precipitation. While a summertime minimum in precipitation occurs between Astoria and Ensenada, a summertime maximum occurs between La Paz and Tapachula. This is consistent with figure 3 which shows that in July the stratocumulus regime does not extend east of about 115°W. The area east and south of La Paz is under the influence of summertime tropical disturbances and is, in fact, an area of frequent tropical storms and hurricanes--on the average eleven in the July - Sept. period (Gunther, 1977). If these tropical cyclones move northwest toward the stratocumulus regime they usually dissipate rapidly as they encounter lower sea surface temperatures. A rare exception was hurricane Kathleen (September 1976), the first hurricane since 1939 to enter the southern California region.

A typical example of the eastern North Pacific stratocumulus regime is shown in figures 4 and 5. The temperature and moisture profiles shown in figure 5 are from an NCAR Electra[1] sounding at 37.8°N, 125.0°W and within one hour of the satellite image. The sounding

[1]This data is discussed more fully in section 6.

TABLE 2. Mean monthly precipitation (in mm) for stations along coastal Oregon, California and Mexico. Data for this and the following four tables was taken primarily from U.S. Dept. of Commerce (1959, 1968).

Station	Period of Record	Latitude	Longitude	Elevation	Jan	Feb	Mar	Apr	May	Jun	Jul	Aug	Sep	Oct	Nov	Dec	Year
Astoria, Oregon	12 years	46.2°N	123.9°W	3 m	302	218	194	127	69	74	29	41	70	182	284	267	1857
North Bend, Oregon	29 years	43.4°N	124.2°W	4 m	261	212	194	98	70	43	11	13	44	141	217	266	1570
Crescent City, California	15 years	41.8°N	124.2°W	17 m	338	255	214	112	92	42	23	13	44	178	193	273	1777
Eureka, California	1951-60	40.8°N	124.2°W	24 m	215	160	122	62	57	22	2	4	21	69	125	182	1041
San Francisco, California	1951-60	37.6°N	122.4°W	27 m	119	83	62	40	16	3	T	T	9	14	41	109	496
Monterey Peninsula, California	12 years	36.6°N	121.9°W	68 m	88	55	40	31	11	2	0	1	8	9	35	62	342
Los Angeles, California	1951-60	33.9°N	118.4°W	37 m	106	51	44	42	7	1	T	1	1	6	31	38	328
San Diego, California	1951-60	32.7°N	117.2°W	11 m	58	32	41	25	5	2	T	2	3	9	18	26	221
Ensenada, Mexico	1951-60	31.9°N	116.6°W	15 m	38	21	16	20	8	T	2	2	0	15	19	20	161
La Paz, Mexico	1951-60	24.2°N	110.2°W	18 m	14	1	3	3	1	8	22	28	48	14	3	26	171
Mazatlan, Mexico	1951-60	23.2°N	106.4°W	78 m	18	4	7	2	T	30	211	182	218	87	7	10	776
Manzanillo, Mexico	1951-60	19.1°N	104.3°W	8 m	13	12	1	10	19	148	163	236	355	172	16	6	1151
Acapulco, Mexico	1951-60	16.8°N	99.9°W	3 m	16	T	T	2	51	266	317	205	414	184	53	11	1519
Salina Cruz, Mexico	1951-60	16.2°N	95.2°W	56 m	7	3	3	T	34	309	234	161	231	62	5	7	1056
Tapachula, Mexico	1951-60	14.9°N	92.3°W	168 m	4	4	19	99	264	440	366	336	487	430	61	7	2517

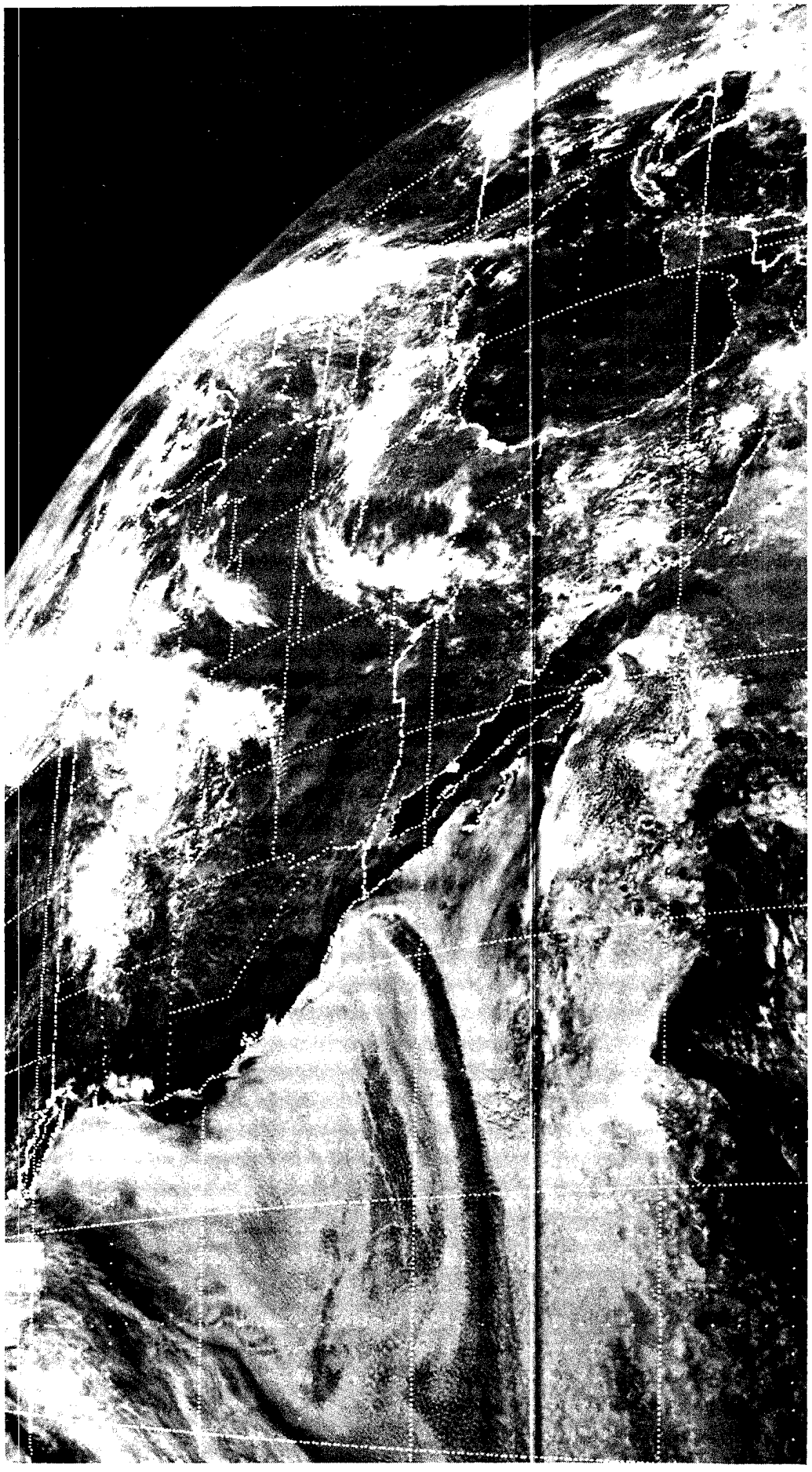

Figure 4. SMS/GOES visible image for 1615Z, 17 June 1976.

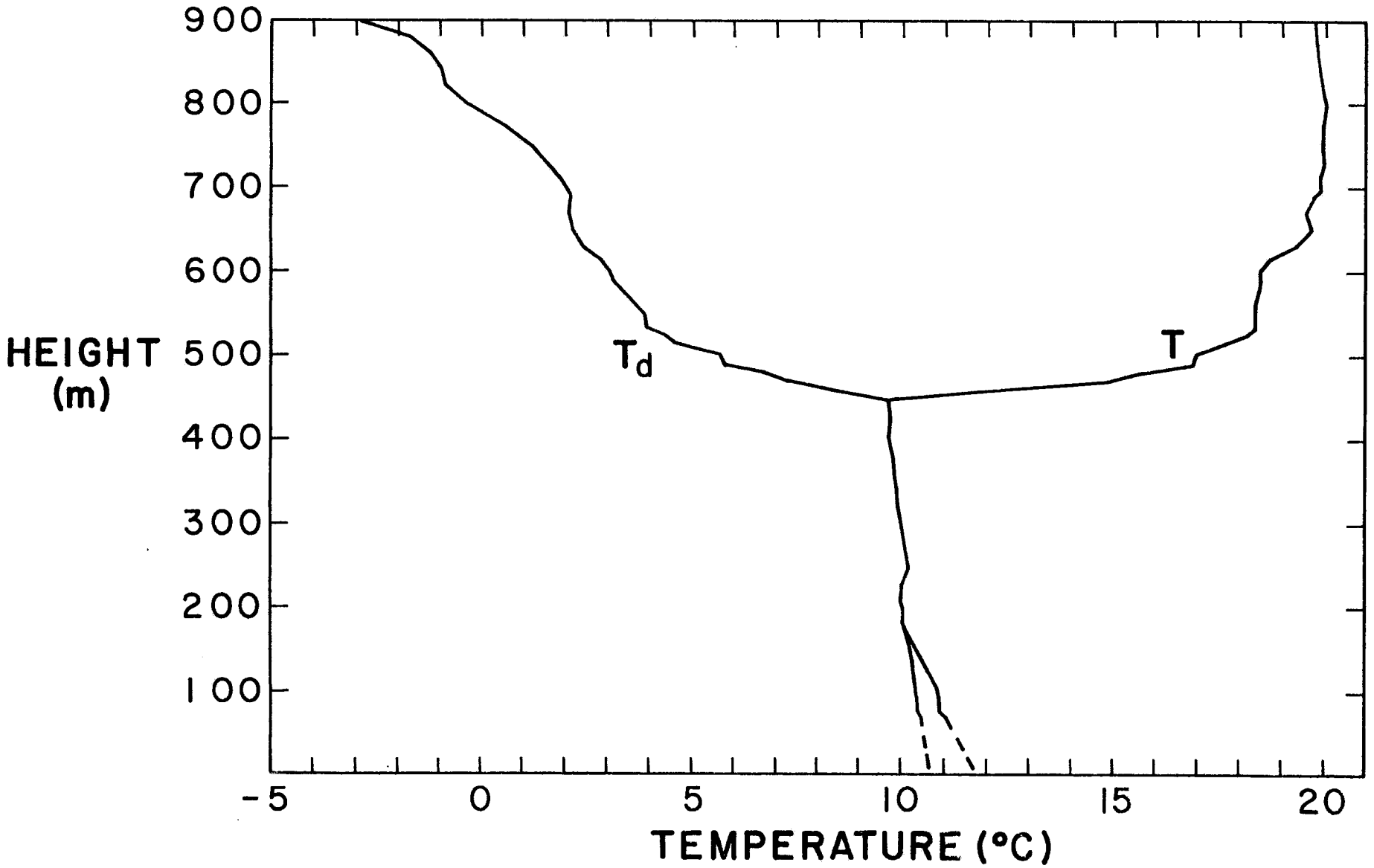

Figure 5a. Temperature and dew point data from an NCAR Electra sounding at 37.8°N and 125.0°W and between 1522 and 1526Z. Dashed lines below 50 m are extrapolations.

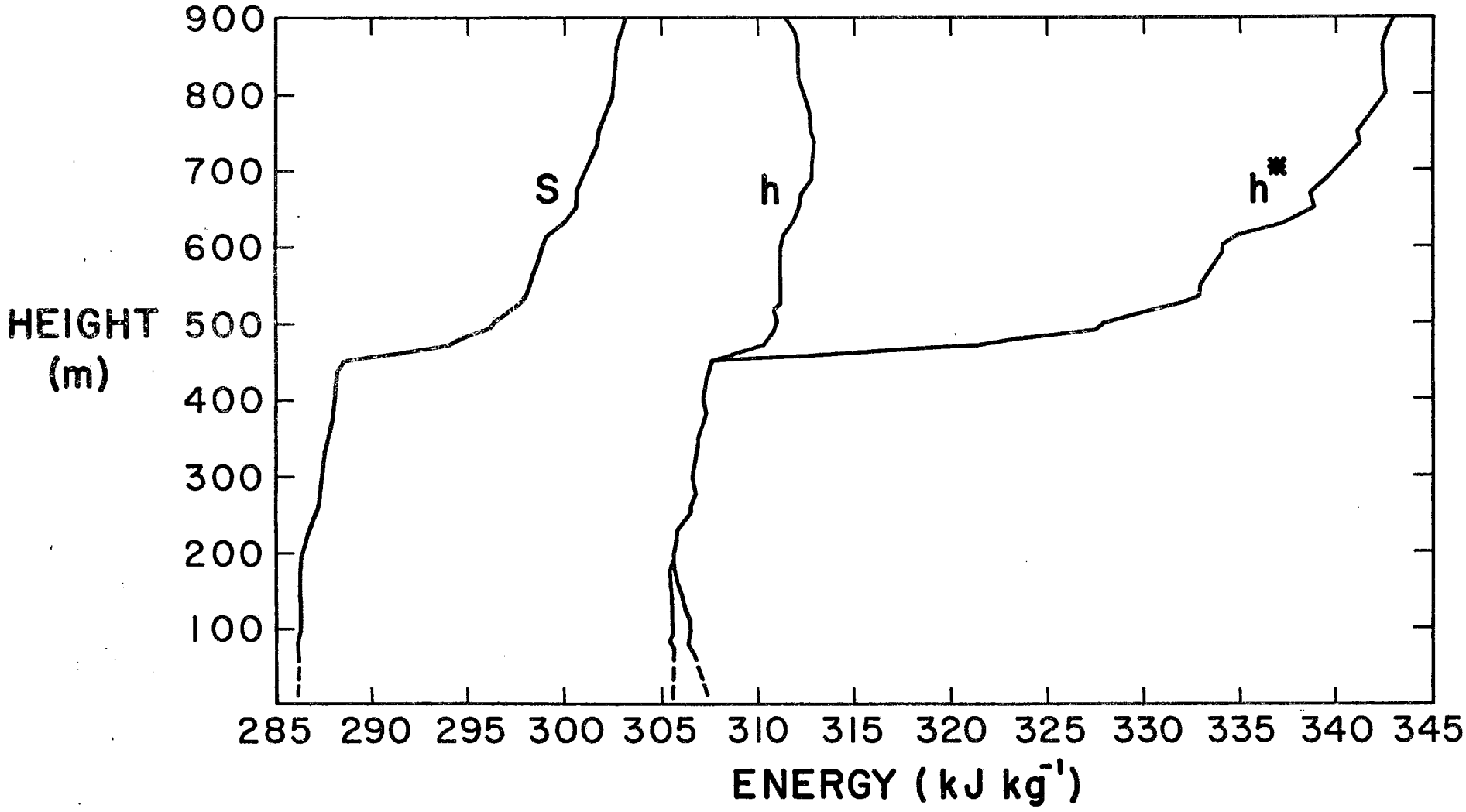

Figure 5b. Dry static energy, moist static energy and saturation static energy data from an NCAR Electra sounding at 37.8°N and 125.0°W and between 1522 and 1526Z. Dashed lines below 50 m are extrapolations.

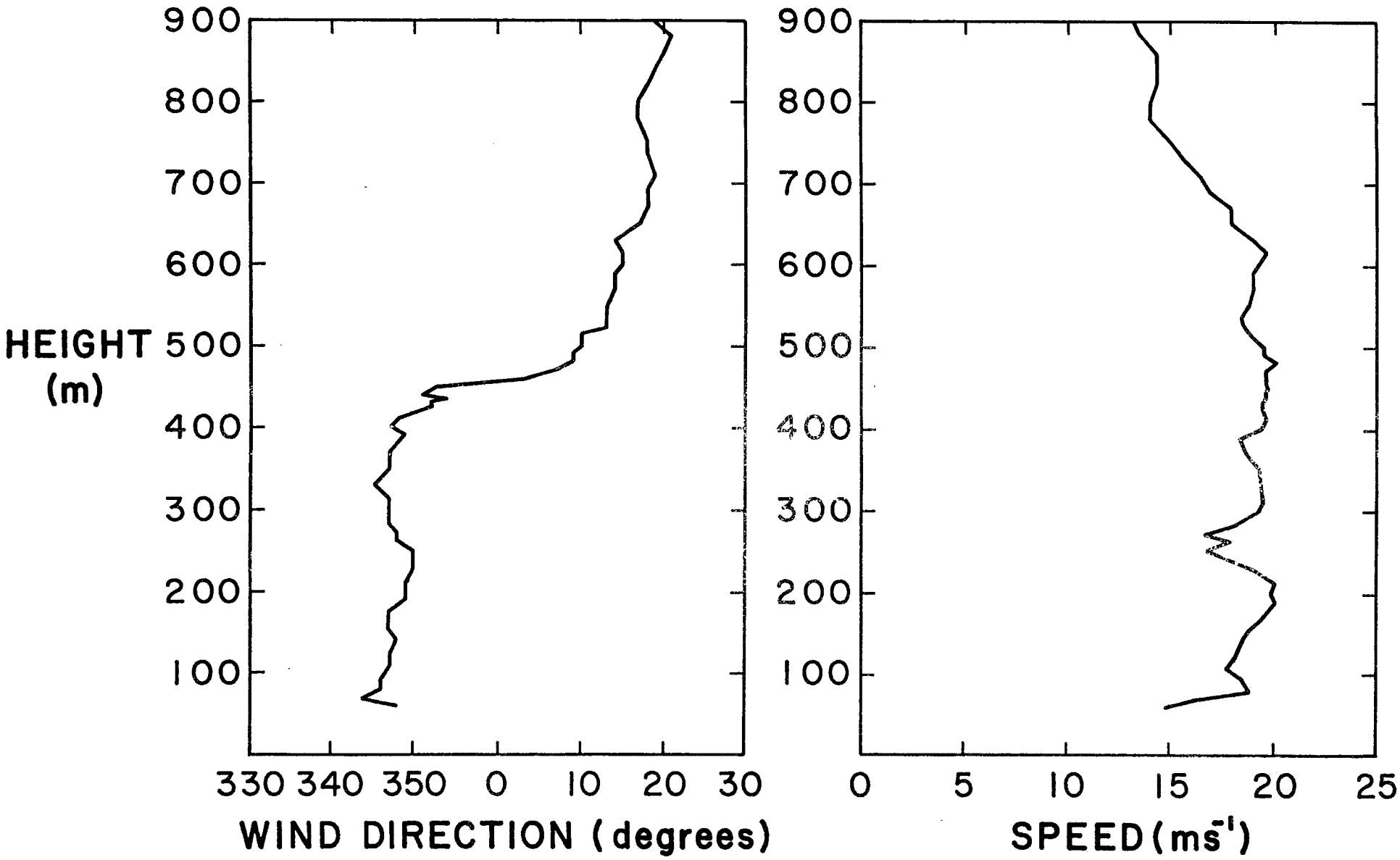

Figure 5c. Wind direction and speed data from an NCAR Electra sounding at 37.8°N and 125.0°W and between 1522 and 1526Z.

shows the structure of the mixed layer and the inversion layer quite well. The subcloud layer is dry adiabatic, the cloud layer is moist adiabatic, and the inversion layer is extremely stable, with a potential temperature increase of about 11°C in 10 mb. The sea surface temperature is very near the surface air temperature. Radiosonde observations tend to considerably smooth such a structure.

1.2 Coastal Equador, Peru and Chile

Precipitation data for coastal Equador, Peru and Chile is shown in Table 3. The table shows that aridity exists between about 5°S and 30°S and is particularly intense between 18°S and 24°S. Even Guayaquil and San Cristobal, which are both very near the equator, experience very little precipitation from August to November. The Peruvian-Chilean desert is the most arid and the latitudinally most extensive of the five primary Bn deserts. An annual rainfall of under 120 mm is maintained along a thin coastal strip about 25° latitude in length. Two unique features of this region are the presence of high mountains close to the coast and the existence of a coastline which bends continuously into rather than away from the atmospheric and oceanic circulations.

A typical example (1545Z, 31 August 1975) of a northern hemisphere summer GOES visible image is shown in figure 6. Note that at this time, when there is considerable tropical storm activity in the northern hemisphere, the eastern South Atlantic stratocumulus regime extends northward across the equator. This is consistent with the very arid August - September conditions at Guayaquil and San Cristobal. Southward, between 30°S and 40°S, the stratocumulus regime breaks up as

TABLE 3. Mean precipitation (mm) for stations along coastal Equador, Peru and Chile.

Station	Period of Record	Latitude	Longitude	Elevation	Jan	Feb	Mar	Apr	May	Jun	Jul	Aug	Sep	Oct	Nov	Dec	Year
San Cristobal, Galapagos Is.	1951-60	0.9°S	89.6°W	6 m	39	155	124	106	28	4	12	7	5	7	6	14	507
Guayaquil, Equador	1951-60	2.2°S	79.9°W	6 m	185	259	255	219	57	10	11	1	T	2	1	23	1023
El Alto, Peru	1951-60	4.3°S	81.2°W	270 m	5	9	12	11	2	T	1	T	T	T	T	1	41
Lambayeque, Peru	1951-60	6.7°S	79.9°W	18 m	2	3	1	4	1	T	T	T	T	1	2	1	15
Lima, Peru	1951-60	12.1°S	77.0°W	137 m	1	T	1	T	1	3	3	4	4	2	1	1	21
Arica, Chile	1941-50	18.5°S	70.4°W	29 m	T	T	0	0	0	T	T	T	T	T	0	0	1
Antofagasta, Chile	1951-60	23.5°S	70.4°W	122 m	0	0	0	0	0	0	T	T	0	0	0	0	T
Coquimbo, Chile	1951-60	29.9°S	71.4°W	27 m	0	0	3	3	34	20	19	16	6	2	T	2	105
Valparaiso, Chile	1951-60	33.0°S	71.6°W	41 m	2	0	3	17	82	96	72	50	19	4	T	4	349
Valdivia, Chile	1951-60	39.8°S	73.2°W	13 m	106	50	96	178	437	371	452	319	225	98	82	72	2486
Punta Galera, Chile	1951-60	40.0°S	73.7°W	40 m	98	48	149	188	449	311	416	368	268	122	92	68	2577
Bahia Felix, Chile	1951-60	53.0°S	74.1°W	15 m	395	325	482	389	323	301	397	392	312	425	417	375	4533

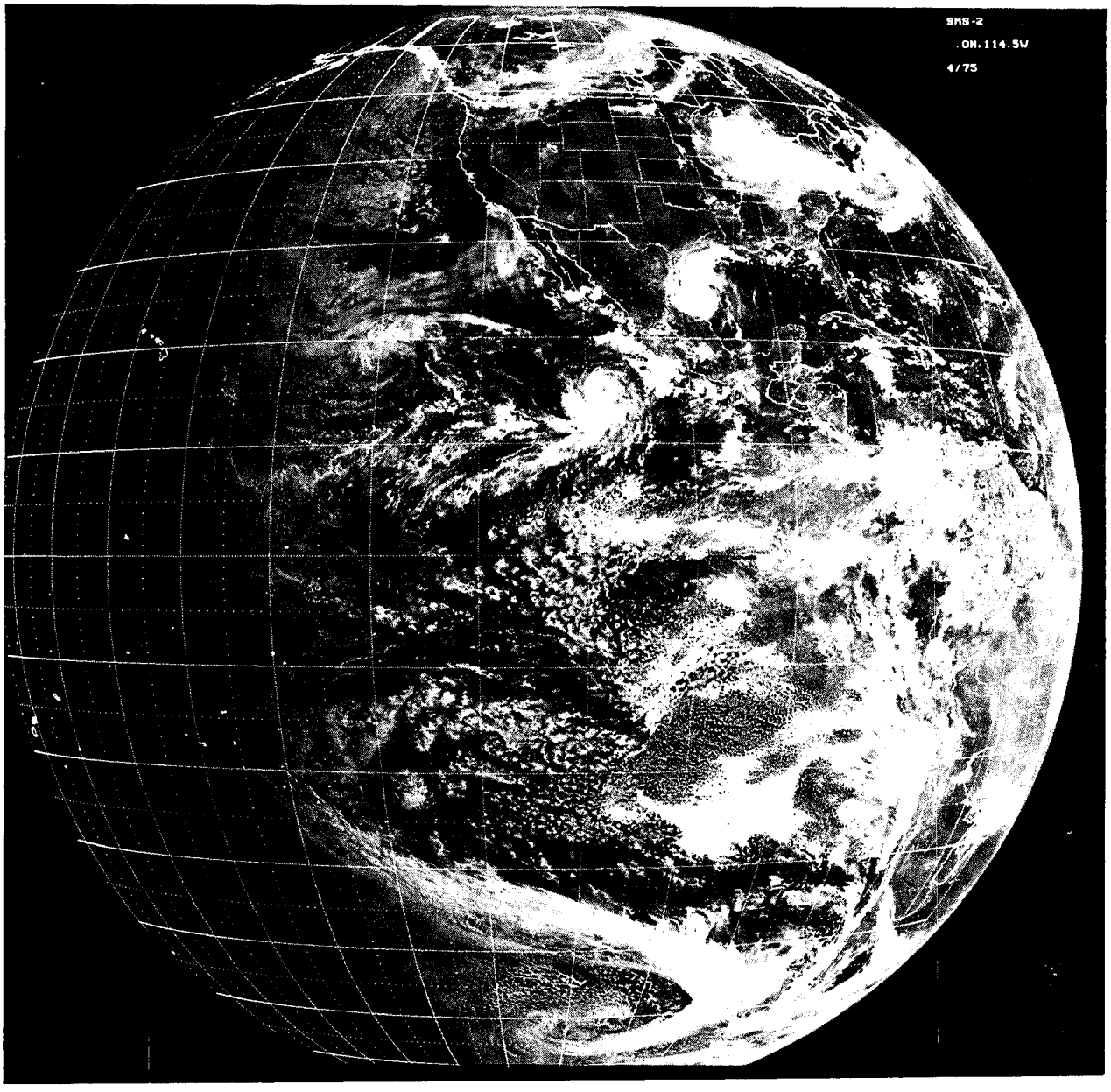

Figure 6. Typical (1545Z, 31 August 1975) full disc SMS/GOES visible image showing northern hemisphere tropical storm activity and the eastern South Atlantic stratocumulus regime.

wintertime cyclones hit the coast of southern Chile. This is consistent with the wet August - September conditions south of Valparaiso.

It should be pointed out that the precipitation data for northern Peru has high interannual variability. Normally in December the southeast trades and the coastal upwelling weaken and warm water appears between Guayaquil and El Alto. This is associated with increased rainfall in the first few months of the year. During occasional major El Nino events the warm water appears considerably farther south causing torrential rains at normally arid stations. For example, during March of the 1972 El Nino event, El Alto recorded 587 mm of precipitation.

1.3 Coastal northwestern Africa

Table 4 gives precipitation data for coastal northwestern Africa, the Canary Islands, and the Cape Verde Islands. The most arid stations lie between 28°N and 21°N. This includes the coast of Spanish Sahara, which is known for active upwelling (La Violette, 1974). A typical example (0900Z, 12 August 1974) of a GATE SMS visible image is shown in figure 7. The large stratocumulus area off the coast of northwestern Africa extends southward almost to the GATE array. The stratocumulus area off the coast of southwestern Africa is seen to extend northward almost to the equator. Figure 7 also shows the mean July - September precipitation for coastal and island stations and for GATE A/B and B scale ships. It is apparent that the low level stratocumulus clouds are associated with low precipitation amounts.

TABLE 4. Mean monthly precipitation (in mm) for stations along coastal northwestern Africa.

Station	Period of Record	Latitude	Longitude	Elevation	Jan	Feb	Mar	Apr	May	Jun	Jul	Aug	Sep	Oct	Nov	Dec	Year
Rabat, Morocco	1921-55	34.0°N	6.8°W	65 m	66	64	66	43	28	8	<2	<2	10	48	84	86	507
Casablanca, Morocco	1908-55	33.6°N	7.7°W	164 m	53	48	56	36	23	5	0	<2	8	38	66	71	406
Porto Santo, Madeira Islands	1951-60	33.0°N	16.3°W	45 m	65	52	41	23	11	3	2	7	9	38	63	62	376
Safi, Morocco	1902-19,1926-55	32.3°N	9.3°W	65 m	51	38	41	23	13	3	0	<2	5	38	53	64	331
Agadir, Morocco	1934-55	30.4°N	9.6°W	50 m	43	28	25	18	3	<2	<2	<2	5	23	36	43	230
Sidi Ifni, Morocco	1951-60	29.4°N	10.2°W	66 m	30	22	11	11	1	1	T	1	3	13	21	35	149
Fuerteventura, Canary Islands	1951-60	28.5°N	13.9°W	228 m	16	19	11	4	1	1	0	1	6	7	26	26	118
Santa Cruz de Tenerife, Canary Islands	1951-60	28.4°N	16.2°W	46 m	48	51	40	12	2	T	0	T	4	49	52	68	326
Las Palmas, Canary Islands	1951-60	27.9°N	15.4°W	22 m	28	30	15	7	4	1	0	T	5	22	47	46	205
Tarfaia, Morocco	1941-54	27.9°N	12.9°W	20 m	8	5	5	<2	<2	<2	<2	<2	8	<2	15	8	61
Villa Cisneros, Spanish Sahara	1951-60	23.7°N	15.9°W	10 m	2	2	2	0	0	T	0	2	10	3	3	9	33
Port Etienne, Mauritania	1951-60	20.9°N	17.0°W	8 m	2	2	3	1	T	T	1	4	9	7	4	3	36
Nouakchott, Mauritania	1951-60	18.1°N	15.9°W	5 m	2	1	T	T	T	2	13	64	58	11	5	16	172
Mindelo, Cape Verde Is.	1951-60	16.9°N	25.0°W	15 m	2	8	T	0	T	0	7	24	41	54	30	10	176
Sal, Cape Verde Is.	1951-60	16.7°N	23.0°W	55 m	2	2	1	0	0	0	18	20	27	16	10	13	109
Praia, Cape Verde Is.	1951-60	14.9°N	23.5°W	35 m	2	4	0	0	0	0	9	38	86	84	35	12	270

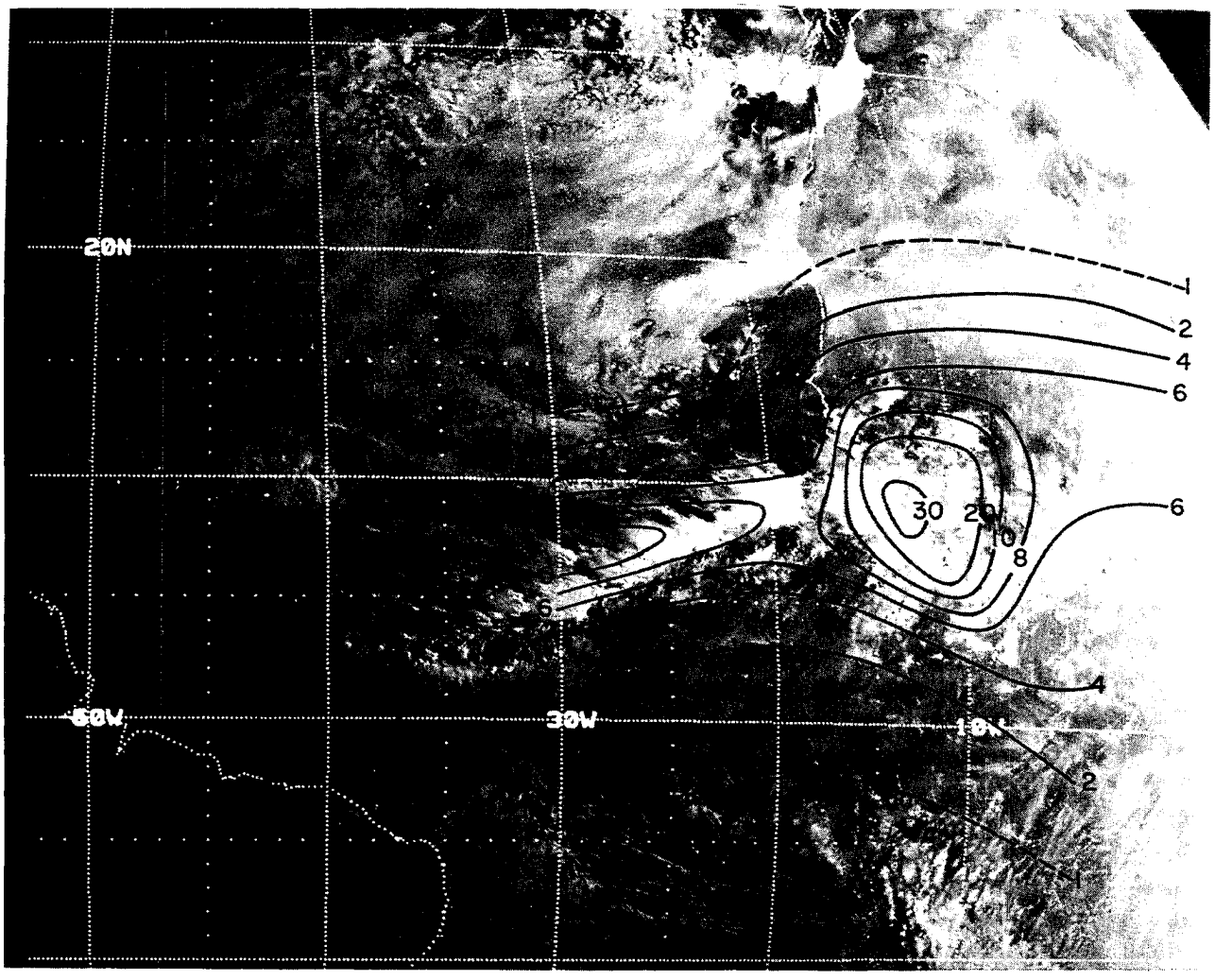

Figure 7. Typical (0900Z, 12 August 1974) SMS visible image taken during GATE. The image shows the stratocumulus area off the coast of northwestern Africa, the northern extent of the stratocumulus area off the coast of southwestern Africa, and a region of disturbed conditions between. Also shown is July-September mean precipitation (mm day^{-1}) for coastal and island stations and for GATE ships.

1.4 Coastal southwestern Africa

Precipitation data for the coast of southwestern Africa is shown in table 5. Between 15°S and 30°S the mean annual precipitation is less than about 60 mm. Between 22°S and 27°S the aridity is particularly intense with mean annual precipitation around 15 mm. Although the mean annual precipitation increases rapidly north of 15°S, table 5 reveals that aridity extends far equatorward during June-September. Also shown in table 5 is data for Ascension Island (7.9°S, 14.4°W). Although it lies on the western edge of the stratocumulus regime, Ascension Island's fairly arid character suggests that it is also under the influence of the south Atlantic high pressure cell and the cool Benguela current.

1.5 Coastal northeastern Africa

The region of coastal northeastern Africa and the western Arabian Sea exhibits extreme seasonal differences. In winter northeasterly flow dominates while in summer both the oceanic and atmospheric circulations are reversed. The summertime oceanic situation is characterized by intense upwelling (Warren et al., 1966; Leetmaa, 1972), while the summertime atmospheric situation is characterized by strong divergent southwesterly flow (see figure 8, taken from Ramage, 1966, and figure 9, taken from Flohn et al., 1968). According to Trewartha (1961) there is a high incidence of fog along the Somalia coast in the summer months while fog is rare in December and January. Precipitation data for this region is given in Table 6.

TABLE 5. Mean precipitation (mm) for stations along coastal southwestern Africa.

Station	Period of Record	Latitude	Longitude	Elevation	Jan	Feb	Mar	Apr	May	Jun	Jul	Aug	Sep	Oct	Nov	Dec	Year
Pointe Noire, Congo	1935-51	4.8°S	11.9°E	17 m	168	205	222	194	100	1	0	2	14	135	164	145	1350
Banana, Congo	1951-57	6.0°S	12.4°E	2 m	93	113	123	109	68	2	0	1	6	38	117	77	747
Luanda, Angola	1879-91, 1894-1903	8.8°S	13.2°E	51 m	30	37	81	129	16	0	0	1	2	6	30	23	355
Lobito, Angola	1911-12,1914-21	12.4°S	13.5°E	1 m	13	40	75	31	3	0	0	0	1	9	22	45	239
Benguela, Angola	1944-52	12.6°S	13.4°E	10 m	10	53	92	74	9	0	0	1	1	10	18	30	298
Mocâmedes, Angola	1913-18,1920-26	15.2°S	12.2°E	45 m	7	6	14	11	0	0	0	0	0	1	2	2	43
Swakopmund, Namibia	1898-1913,1945-55	22.7°S	14.5°E	19 m	2	2	2	2	1	0	0	1	0	1	1	2	14
Walvis Bay, Namibia	1926,1931-38	23.0°S	14.5°E	7 m	0	1	6	2	1	0	0	0	0	1	1	0	12
Luderitz, Namibia	1902-13,1941-55	26.6°S	15.1°E	23 m	1	3	1	1	3	2	1	2	2	0	0	1	17
Alexander Bay, South Africa	1931-59	28.6°S	16.5°E	12 m	1	2	7	4	8	4	7	4	3	2	3	2	47
Port Nolloth, South Africa	1880-1950	29.2°S	16.9°E	104 m	2	2	5	5	9	8	9	8	5	3	3	2	61
Cape Town, South Africa	1842-1950	33.9°S	18.5°E	12 m	16	14	19	53	91	102	98	82	58	39	24	19	615
Ascension Island	1951-60	7.9°S	14.4°W	17 m	3	3	12	20	14	19	14	12	8	9	4	5	123

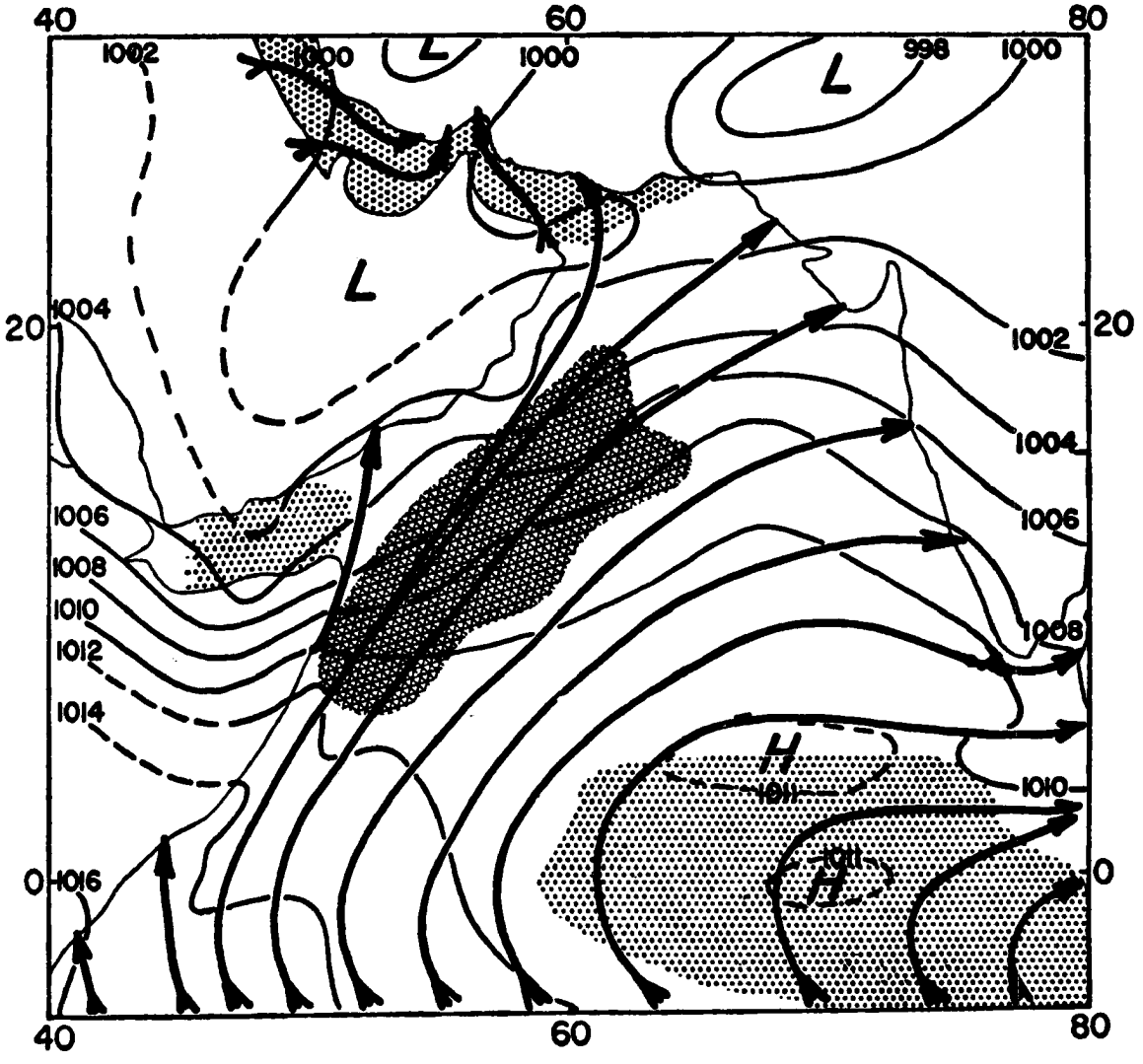

Figure 8. August mean sea level pressure and mean resultant winds. Speeds less than 10 kt stippled, greater than 25 kt hatched. After Ramage (1966).

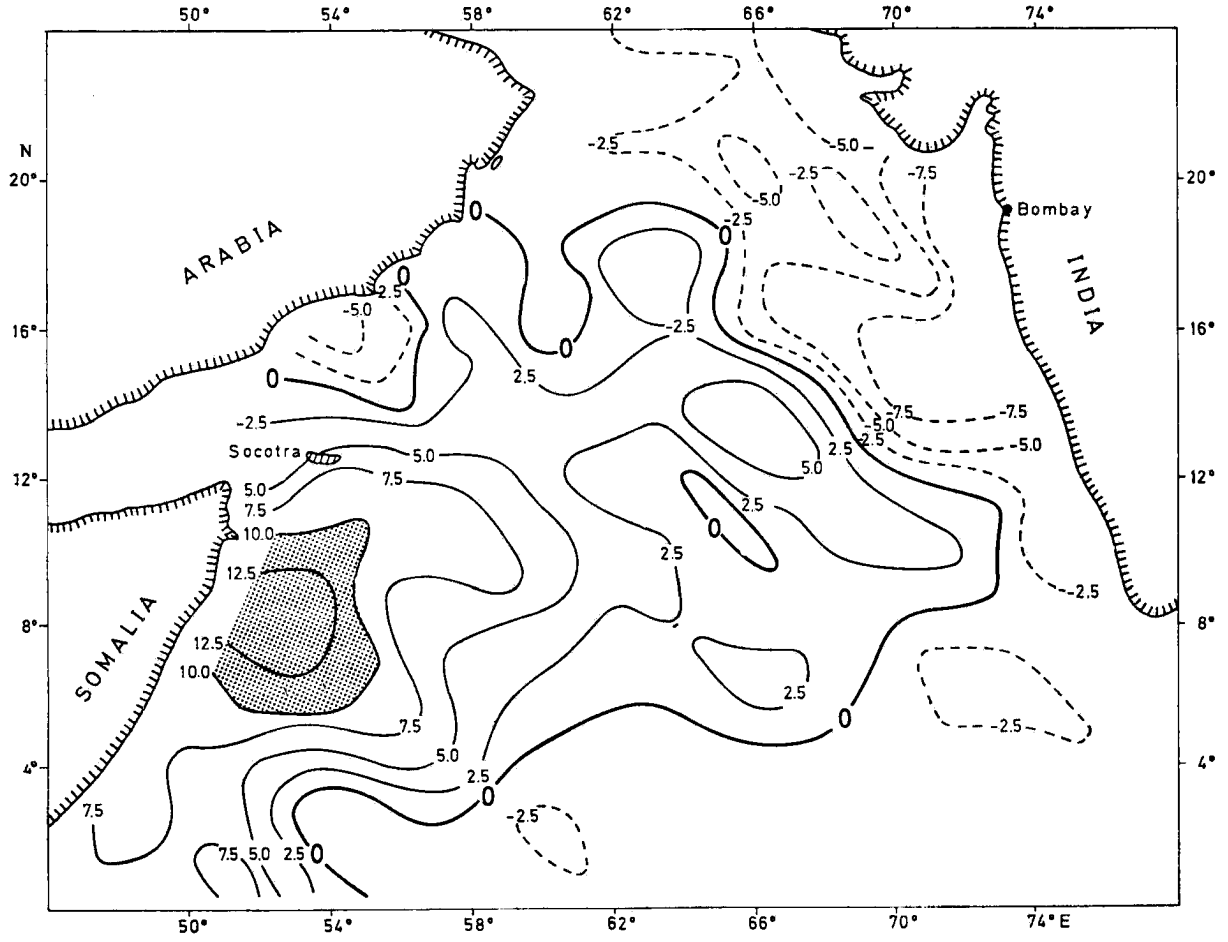

Figure 9. Mean July divergence of surface winds. After Flahn et al. (1968).

TABLE 6. Mean precipitation (mm) for stations along coastal northeastern Africa.

Station	Period of Record	Latitude	Longitude	Elevation	Jan	Feb	Mar	Apr	May	Jun	Jul	Aug	Sep	Oct	Nov	Dec	Year
Socotra, Socotra	3 years	12.4°N	53.7°E	?	3	3	10	0	3	30	0	0	3	10	51	81	194
Bosaso, Somali Republic	1951-60	11.3°N	49.2°E	2 m	0	0	0	T	0	0	0	0	0	6	5	0	11
Obbia, Somali Republic	1932-39	5.3°N	48.5°E	15 m	13	0	8	20	33	0	T	T	3	38	25	25	165
Mogadisho, Somali Republic	1951-60	2.0°N	45.4°E	10 m	1	0	11	103	63	72	60	26	10	18	46	12	422
Kismayu, Somali Republic	1951-60	0.4°S	42.4°E	10 m	T	0	T	23	102	63	59	12	8	8	9	4	288
Lamu, Kenya	40 years	2.3°S	40.9°E	?	5	2	20	124	361	170	69	41	30	41	33	28	924

1.6 Other stratocumulus regions

Although we have discussed only the five primary Bn deserts and their associated cloud systems, we do not mean to imply that stratocumulus clouds are limited to these areas. For example, stratocumulus often occur near the coast of Australia (Paltridge, 1974; Platt, 1976), during wintertime cold air outbreaks over the Kuroshio current (e.g. Ninomiya, 1975; Nitta, 1976; Lenschow and Agee, 1976), the Gulf Stream, and the Great Lakes (Lenschow, 1973). A typical example of a cold air outbreak over the Kuroshio current during AMTEX '75 is shown in figure 10a. The DMSP visible image taken at 0255Z, 16 February 1975 (Lenschow and Agee, 1976) shows the extensive stratocumulus deck associated with the outbreak, which lasted about three days (15-17 February) when a low pressure system developed east of Japan. Surface winds and inversion base (Ninomiya, 1976) for 00Z 16 February are shown in figure 10b. Note the rapid deepening of the boundary layer as the air flows over the sea surface temperature pattern shown in figure 10c.

1.7 Outline

A theoretical framework for the study of marine stratocumulus convection was first presented by Lilly (1968). Some aspects of Lilly's model have been studied by Schubert (1976), Deardorff (1976), Arakawa (1975), and Randall (1976). Schubert (1976) studied horizontally homogeneous steady state and time dependent solutions to the model, Deardorff (1976) discussed the entrainment relation, and Arakawa (1975) and Randall (1976) included the model in a generalized planetary boundary layer parameterization for the UCLA GCM. In the remainder of this paper we shall attempt to further extend Lilly's cloud-topped mixed layer model.

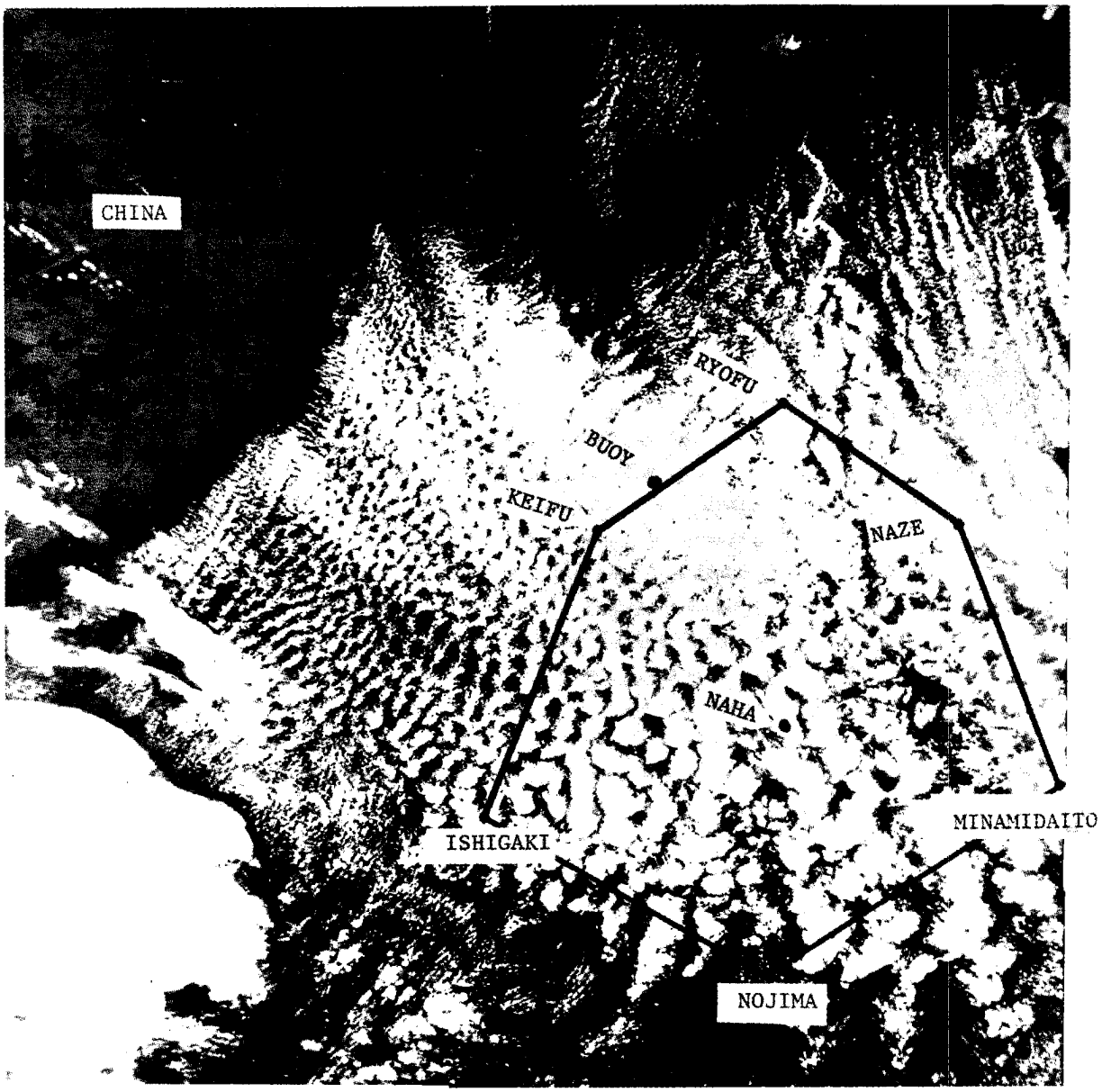

Figure 10a. DMSP visible image taken at 0255Z, 16 February 1975 showing extensive stratocumulus deck associated with a cold air outbreak. Also shown is the AMTEX hexagonal network. After Lenschow and Agee (1976).

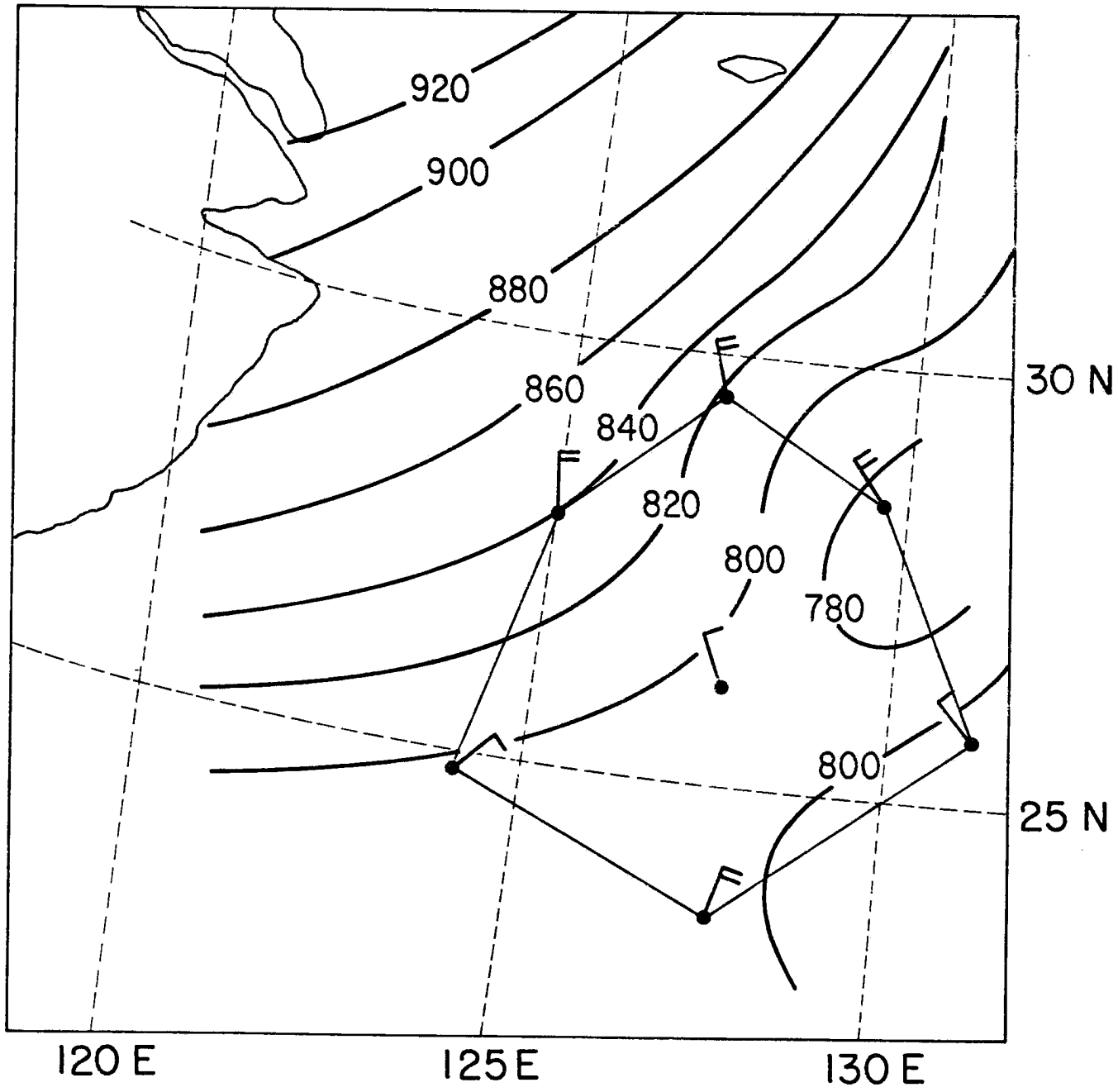

Figure 10b. Horizontal distribution of the pressure (mb) at the inversion base at 00Z, 16 February 1975. After Ninomiya (1976). Also shown are the 00Z-06Z surface winds.

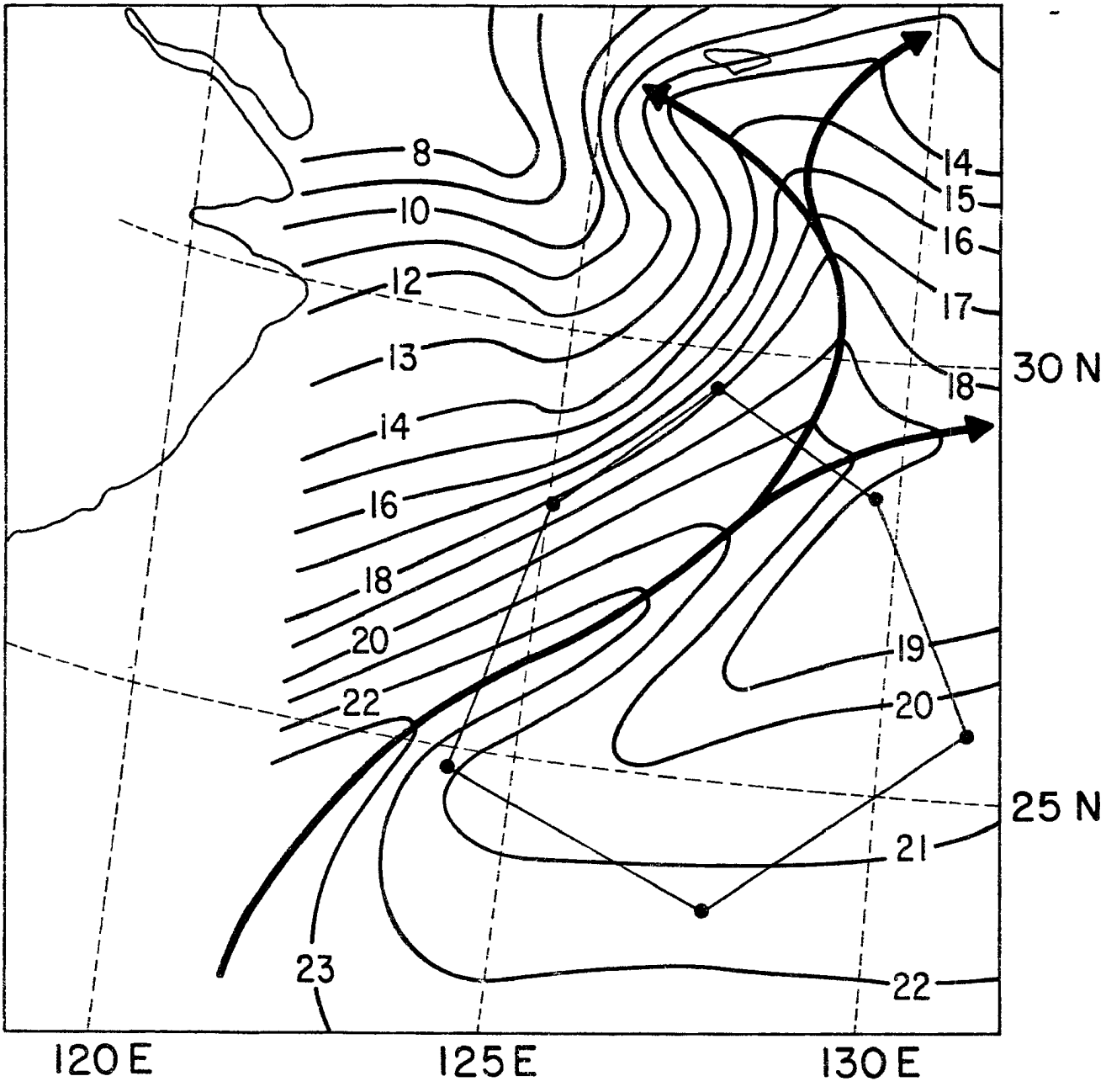

Figure 10c. Position of the Kuroshio Current and the mean sea surface temperatures for February 1968 (from Lenschow, 1972). For present purposes this mean map can be regarded as identical to the AMTEX '75 map presented by the Japanese Oceanographic Group (1975).

In section 2 we extend Lilly's model to include horizontal advection in a natural coordinate system and also to include a simple but coupled radiative model. In section 3 we study the influence of large-scale divergence and sea surface temperature on the horizontally homogeneous steady state solutions. Sections 4 and 5 present both numerical and analytical results for horizontally inhomogeneous conditions. Finally, in section 6 we discuss the design of observational programs to expand our knowledge of marine stratocumulus convection.

2. Governing equations for a cloud-topped mixed layer

In a non-saturated mixed layer the dry static energy $s = c_p T + gz$ and the water vapor mixing ratio q are constant with height up to the top of the mixed layer z_B, and the lifting condensation level z_C lies above z_B. In a cloud-topped mixed layer the moist static energy $h = c_p T + gz + Lq$ and the total water mixing ratio $q+\ell$ are constant with height up to the top of the mixed layer z_B, and the lifting condensation level z_C lies below z_B. If h and $q+\ell$ are constant with height in the mixed layer, it follows that the same is true for $s-L\ell$. The temperature and moisture fields in the mixed layer are known if any two of the three quantities h, $q+\ell$ and $s-L\ell$ are known. Although we shall occasionally use $s-L\ell$, most of our discussion will be in terms of h and $q+\ell$.

The dependent variables of the cloud-topped mixed layer model we shall now present are listed in the first column of Table 7. In addition the required constants and externally specified parameters are listed in the second and third columns. The dependent variables are functions of the horizontal coordinates and time. We shall use a natural coordinate system in which x denotes distance in the downstream direction. The individual time derivative is then given by $\frac{\partial}{\partial t} + V \frac{\partial}{\partial x}$, where V is the speed of the horizontal wind. Riehl et al. (1951) and Kraus (1968) have shown that the wind speed and direction over the Eastern North Pacific in summer are nearly constant with height in the lower layers. Thus, we shall assume that there is no turning of the wind with height and no change of wind speed with height. The horizontal projections of all trajectories are then coincident with the surface

TABLE 7. Dependent variables, constants and externally specified parameters of the cloud-topped mixed layer model.

Dependent Variables		Constants		Externally Specified Parameters	
cloud top height	z_B	see (2.11)	b	large-scale divergence	D
cloud base height	z_C	specific heat at constant pressure	c_p	wind speed	V
mixed layer moist static energy	h_M	bulk transfer coefficient	C_T	saturation moist static energy at sea surface temperature and pressure	h_S^*
mixed layer total water mixing ratio	$(q+\ell)_M$	gravity	g	saturation mixing ratio at sea surface temperature and pressure	q_S^*
surface moist static energy flux	$(\overline{w'h'})_S$	scale height	H	moist static energy just above cloud top	$h(z_B^+)$
cloud top moist static energy flux	$(\overline{w'h'})_B$	entrainment parameter	k	water vapor mixing ratio just above cloud top	$q(z_B^+)$
surface water vapor flux	$(\overline{w'q'})_S$	latent heat of condensation	L	downward long-wave flux just above cloud top	$F_L^{\downarrow}(z_B^+)$
cloud top total water flux	$\overline{w'(q'+\ell')}_B$	see (2.19)	β	cloud top jump in short-wave flux	ΔF_S
cloud top moist static energy jump	Δh	see (2.19)	γ		
cloud top total water jump	$\Delta(q+\ell)$	see (2.16)	δ		
cloud top temperature	$T(z_B^-)$	see (2.19)	ε		
cloud top jump in net radiative flux	ΔF_R	density	ρ		
		Stefan-Boltzman constant	σ		

trajectories. We need not distinguish between winds at cloud top, in the mixed layer, or at the surface.

2.1 Governing equations for the convective model

With the above assumptions the mixed layer budgets of moist static energy and total water are

$$\frac{\partial h_M}{\partial t} + V \frac{\partial h_M}{\partial x} = \frac{(\overline{w'h'})_S - (\overline{w'h'})_B}{z_B} , \tag{2.1}$$

$$\frac{\partial (q+\ell)_M}{\partial t} + V \frac{\partial (q+\ell)_M}{\partial x} = \frac{(\overline{w'q'})_S - \overline{w'(q'+\ell')}_B}{z_B} . \tag{2.2}$$

These equations state that local changes of h_M and $(q+\ell)_M$ are caused by horizontal advection by the known wind V and by the vertical convergence of the turbulent fluxes. Because the layer is mixed the turbulent fluxes are linear with height in the layer and jump to zero above z_B.

The surface turbulent fluxes of h and q are given by

$$(\overline{w'h'})_S = C_T V [h_S^* - h_M] , \tag{2.3}$$

$$(\overline{w'q'})_S = C_T V [q_S^* - (q+\ell)_M] . \tag{2.4}$$

These equations relate the surface fluxes to the transfer coefficient C_T, the surface wind speed V, and the sea-air differences, where h_S^* and q_S^* are the saturation values of h and q at the sea surface temperature and pressure.

Application of the budget equations for h and $q+\ell$ to the infinitesimally thin layer at the cloud top yields

$$\left(\frac{\partial z_B}{\partial t} + V\frac{\partial z_B}{\partial x} - w_B\right)\Delta h + (\overline{w'h'})_B = \rho^{-1}\Delta F_R \ , \qquad (2.5)$$

$$\left(\frac{\partial z_B}{\partial t} + V\frac{\partial z_B}{\partial x} - w_B\right)\Delta(q+\ell) + \overline{w'(q'+\ell')}_B = 0 \ , \qquad (2.6)$$

where w_B is the large-scale vertical velocity at z_B, Δh and $\Delta(q+\ell)$ are jumps across z_B, and ΔF_R is the jump in the radiative flux across z_B. These equations are the cloud top jump conditions on moist static energy and total water. When multiplied by the density, ρ, both (2.5) and (2.6) contain the quantity $\rho\left(\frac{\partial z_B}{\partial t} + V\frac{\partial z_B}{\partial x} - w_B\right)$, which is the net mass flowing into the mixed layer per unit horizontal area per unit time. Such a mass flux into the mixed layer can be due to a local increase in the depth of the mixed layer with time, a horizontal flow across the top of the mixed layer when it deepens in the downstream direction, a large-scale subsidence, or more generally, a combination of these three effects. Non-turbulent air flowing into the mixed layer from above instantaneously changes its moist static energy by an amount Δh and its total water content by an amount $\Delta(q+\ell)$, where

$$\Delta h = h(z_B+) - h_M \ , \qquad (2.7)$$

$$\Delta(q+\ell) = q(z_B+) - (q+\ell)_M \ , \qquad (2.8)$$

$h(z_B+)$ and $q(z_B+)$ being known functions of z_B. According to (2.5), the instantaneous change in moist static energy is due to discontinuities in both the turbulent moist static energy flux and the radiative flux, while according to (2.6), the instantaneous change in total water content is due to a discontinuity in the turbulent total water flux.

Equations (2.5) and (2.6) can be regarded as predictive equations for z_B. In order that they predict z_B in a consistent manner,

$$\frac{L\Delta(q+\ell)}{\Delta h}\,(\overline{w'h'})_B - L\overline{w'(q'+\ell')}_B = \frac{L\Delta(q+\ell)}{\Delta h}\,\rho^{-1}\Delta F_R \,. \qquad (2.9)$$

The cloud base height z_C is approximately given in terms of the mixed layer total water content $(q+\ell)_M$ and the saturation mixing ratio of the air just above the surface q_o^* as

$$\frac{z_C}{H} = \frac{q_o^* - (q+\ell)_M}{b} = \frac{(1+\gamma)[q_S^* - (q+\ell)_M] - \frac{\gamma}{L}[h_S^* - h_M]}{b}, \qquad (2.10)$$

where b is given by

$$b = \kappa\varepsilon\gamma + p\left(\frac{\partial q^*}{\partial p}\right)_T , \qquad (2.11)$$

ε and γ are defined in (2.19), and the scale height H and reference pressure p are assumed constant.

Lilly (1968) has argued that the turbulent energy balance sets maximum and minimum bounds on the entrainment. The entrainment relation,

$$\frac{k}{z_B}\int_0^{z_B} \overline{w's_v'}\,dz + \tfrac{1}{2}(1-k)(\overline{w's_v'})_{min} = 0 \,, \qquad (2.12)$$

is a weighted average of Lilly's maximum entrainment relation,

$$\int_0^{z_B} \overline{w's_v'}\,dz = 0 \quad \text{but} \quad \overline{w's_v'} \neq 0 \text{ somewhere}, \qquad (2.13)$$

and his minimum entrainment relation,

$$(\overline{w's_v'})_{min} = 0 \quad \text{but} \quad \int_0^{z_B} \overline{w's_v'}\, dz > 0 \ , \tag{2.14}$$

where $\overline{w's_v'}$ is the turbulent flux of virtual dry static energy and $(\overline{w's_v'})_{min}$ is the minimum value of this flux. The weighting factor k lies between zero and unity. The factor ½ in the second term of (2.12) is somewhat arbitrary and has been included so that (2.12) reduces to the conventional

$$(\overline{w's_v'})_B = -k(\overline{w's_v'})_S \tag{2.15}$$

in the nonsaturated case. Omission of the factor ½ simply results in a revised interpretation of the parameter k.

If the effects of both water vapor and liquid water on buoyancy are included in the definition of the virtual dry static energy, then the virtual dry static energy s_v is related to the dry static energy s, the water vapor mixing ratio q, and the liquid water mixing ratio ℓ by

$$s_v = s + c_p T(\delta q - \ell) \ , \tag{2.16}$$

where $\delta = 0.608$ and T is a constant reference temperature. Since $\overline{w'\ell'}$ vanishes in the subcloud layer while in the cloud layer $\overline{w'q'}$ and $\overline{w'h'}$ are related by

$$L\overline{w'q'} = \frac{\gamma}{1+\gamma}\overline{w'h'} \quad \text{for} \quad z_C < z < z_B \ , \tag{2.17}$$

the turbulent virtual dry static energy flux can be expressed as

$$\overline{w's_v'} = \begin{cases} \beta\, \overline{w'h'} - \varepsilon L\overline{w'(q'+\ell')} & z_C < z < z_B \\ \overline{w'h'} - (1-\varepsilon\delta)L\overline{w'(q'+\ell')} & 0 < z < z_C \ , \end{cases} \tag{2.18}$$

where

$$\beta = \frac{1 + \gamma\varepsilon(\delta+1)}{1+\gamma} , \qquad \gamma = \frac{L}{c_p}\left(\frac{\partial q^*}{\partial T}\right)_p , \qquad \varepsilon = \frac{c_p T}{L} . \tag{2.19}$$

Since h and $(q+\ell)$ are constant with height in the mixed layer, their turbulent fluxes must be linear functions of height so that

$$\overline{w'h'} = (1 - \frac{z}{z_B})(\overline{w'h'})_S + \frac{z}{z_B}(\overline{w'h'})_B , \tag{2.20}$$

$$\overline{w'(q'+\ell')} = (1 - \frac{z}{z_B})(\overline{w'q'})_S + \frac{z}{z_B}\overline{w'(q'+\ell')}_B . \tag{2.21}$$

Substitution of (2.18), (2.20) and (2.21) into (2.12) results in an expression which relates z_B, z_C, $(\overline{w'h'})_S$, $(\overline{w'h'})_B$, $(\overline{w'q'})_S$, and $\overline{w'(q'+\ell')}_B$,

$$\left\{\beta\left[1-\left(\frac{z_C}{z_B}\right)^2\right] + \left(\frac{z_C}{z_B}\right)^2\right\}(\overline{w'h'})_B - \left\{\varepsilon\left[1-\left(\frac{z_C}{z_B}\right)^2\right] + (1-\varepsilon\delta)\left(\frac{z_C}{z_B}\right)^2\right\}L\overline{w'(q'+\ell')}_B$$

$$+\left\{\beta\left(\frac{z_B-z_C}{z_B}\right)^2 + \left[1-\left(\frac{z_B-z_C}{z_B}\right)^2\right]\right\}(\overline{w'h'})_S - \left\{\varepsilon\left(\frac{z_B-z_C}{z_B}\right)^2 + (1-\varepsilon\delta)\left[1-\left(\frac{z_B-z_C}{z_B}\right)^2\right]\right\}L(\overline{w'q'})_S$$

$$+\frac{1-k}{k}\min\left\{\begin{array}{c} \beta(\overline{w'h'})_B - \varepsilon L\overline{w'(q'+\ell')}_B \\ \left[\frac{z_B-z_C}{z_B}(\overline{w'h'})_S + \frac{z_C}{z_B}(\overline{w'h'})_B\right] - (1-\varepsilon\delta)L\left[\frac{z_B-z_C}{z_B}(\overline{w'q'})_S + \frac{z_C}{z_B}\overline{w'(q'+\ell')}_B\right] \\ (\overline{w'h'})_S - (1-\varepsilon\delta)L(\overline{w'q'})_S \end{array}\right\} = 0 . \tag{2.22}$$

Since $\overline{w's_v'}$ is linear with height in the subcloud and cloud layers but discontinuous at cloud base, it would appear that the minimum in $\overline{w's_v'}$

could occur at the top of the cloud layer z_B, the bottom of the cloud layer z_{C+}, the top of the subcloud layer z_{C-}, or the bottom of the subcloud layer z = 0. However, the possibility of the minimum occurring at z_{C+} can be excluded by using (2.17), (2.18) and (2.19) to show that

$$(\overline{w's_v'})_{z_{C+}} - (\overline{w's_v'})_{z_{C-}} = [1 - \varepsilon(\delta+1)]\,[L\overline{w'(q'+\ell')}_{z_C} - \frac{\gamma}{1+\gamma}(\overline{w'h'})_{z_C}]$$

$$= [1 - \varepsilon(\delta+1)]L(\overline{w'\ell'})_{z_{C+}} \quad . \qquad (2.23)$$

Since $[1 - \varepsilon(\delta+1)] > 0$ and $(\overline{w'\ell'})_{z_{C+}} > 0$, the virtual dry static energy flux is larger at z_{C+} than at z_{C-}, and only the remaining three possibilities are shown in the large bracket of (2.22).

2.2 Governing equations for the radiative model

Boundary layer convection is often driven by the upward virtual temperature flux from a warm underlying surface. This is usually the case for summertime convection over dry land (e.g. Deardorff, 1974 a,b), for subcloud layer convection beneath trade cumulus clouds over much of the tropics (e.g. Pennel and LeMone, 1974; LeMone and Pennel, 1976), and for wintertime cold air outbreaks over warm water surfaces (e.g. Lenschow, 1973; and Lenschow and Agee, 1976). However, in the stratocumulus regimes which border the cool coastal Bn climates, the virtual temperature flux at the surface is usually only weakly positive or is even negative, and yet the boundary layer is quite turbulent. Thus, cloud-topped mixed layers are often driven or at least partially driven not by heating from below but by cooling from above.

In this subsection we are concerned with the determination of the important ΔF_R term in (2.5). Since we have neglected any radiative heating or cooling which might occur in (2.1), the ΔF_R term in (2.5) is the only place radiation enters the convective model. The jump in the net radiative flux at cloud top consists of the sum of the jump in the long-wave flux and the jump in the short-wave flux, i.e.

$$\Delta F_R = \Delta F_L + \Delta F_S \ . \tag{2.24}$$

In this paper we consider ΔF_S as externally specified. Thus, let us consider the cloud top jump in the long-wave flux.

Idealized curves of the upward and downward long-wave radiative fluxes in and near a stratocumulus cloud are shown in figure 11. The downward long-wave flux $F_L^{\downarrow}$ changes sharply at cloud top while the upward flux $F_L^{\uparrow}$ changes considerably less sharply at cloud base. The net upward long wave flux, defined by

$$F_L = F_L^{\uparrow} - F_L^{\downarrow} \ , \tag{2.25}$$

is also shown in figure 11. The time rate of temperature change due to long-wave radiation is given by $-\frac{1}{\rho c_p}\frac{\partial F_L}{\partial z}$, the vertical profile of which is shown on the right of figure 11. Since we are considering only the cloud top long-wave cooling, we need only know the jump in the net long-wave flux at cloud top, i.e.

$$\Delta F_L = F_L(z_{B+}) - F_L(z_{B-}) \ . \tag{2.26}$$

Since $F_L(z_{B-})$ vanishes, we can rewrite (2.26) as

$$\Delta F_L = F_L(z_{B+}) = F_L^{\uparrow}(z_{B+}) - F_L^{\downarrow}(z_{B+}) \ . \tag{2.27}$$

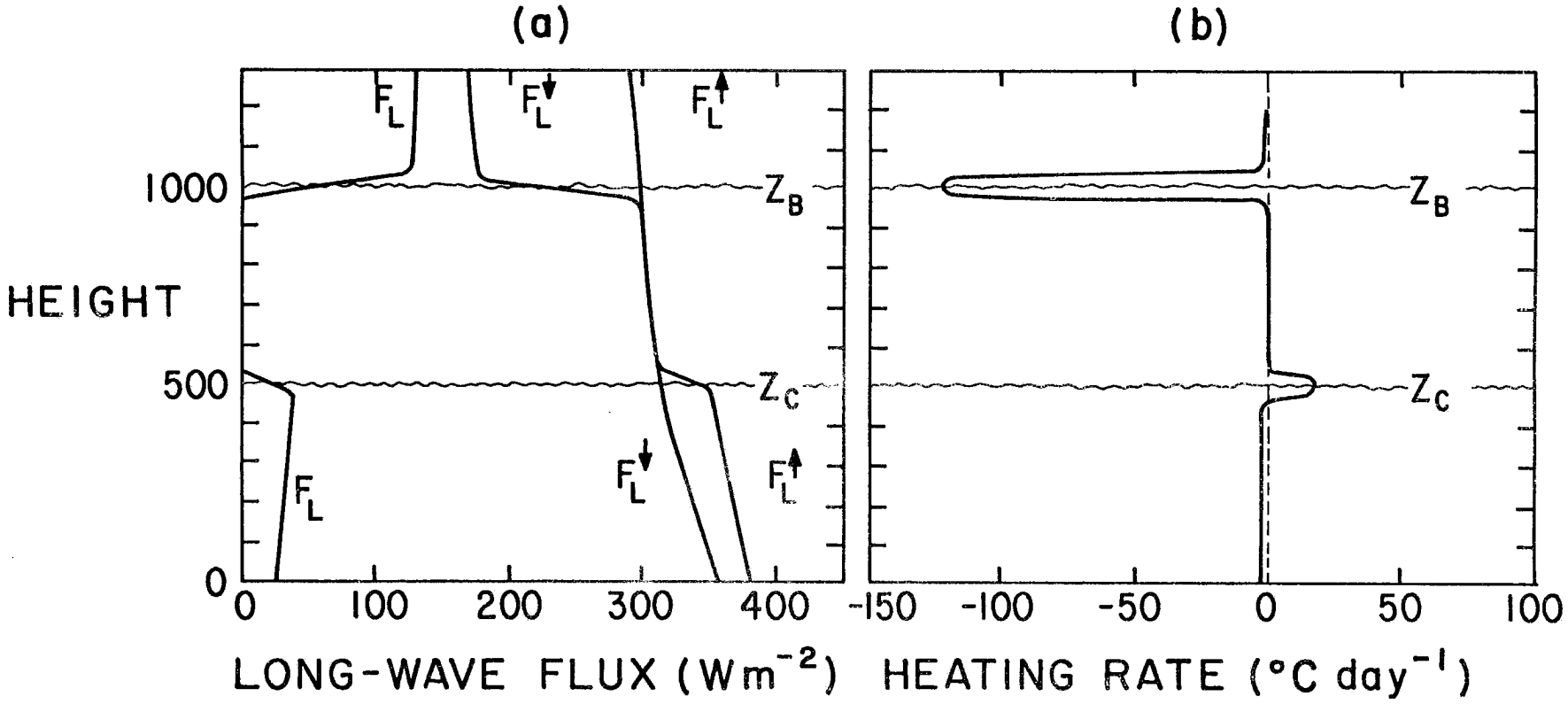

Figure 11. (a) Idealized profiles of the upward and downward long-wave radiative fluxes in and near a stratocumulus cloud. (b) Resulting heating rate. Values on the abscissa and ordinate are meant to be only roughly indicative. The warming at cloud base and the cooling in the subcloud layer are neglected in the present model.

If $F_L^{\uparrow}(z_{B+})$ is assumed to be the blackbody flux at the cloud top temperature, then

$$\Delta F_L = \sigma T^4(z_{B-}) - F_L^{\downarrow}(z_{B+}) \ . \tag{2.28}$$

The cloud top temperature $T(z_{B-})$ can be related to the model variables h_M, $(q+\ell)_M$, z_B and z_C as follows. The dry static energy at cloud top is equal to the dry static energy at cloud base plus the change which occurs when following a moist adiabat from cloud base to cloud top, i.e.

$$s(z_{B-}) = s(z_C) + \left(\frac{\partial s}{\partial z}\right)_{h^*}(z_B - z_C) \ . \tag{2.29}$$

Since it can be shown that

$$\left(\frac{\partial s}{\partial z}\right)_{h^*} = \frac{L}{1+\gamma}\frac{b}{H} \ , \tag{2.30}$$

and since $s(z_C)$ is equal to $h_M - L(q+\ell)_M$, we can rewrite (2.29) as

$$T(z_{B-}) = \frac{1}{c_p}\left[h_M - L(q+\ell)_M + \frac{L}{1+\gamma}\frac{b}{H}(z_B - z_C) - gz_B\right] \ . \tag{2.31}$$

Equation (2.31) gives the cloud top temperature in terms of h_M, $(q+\ell)_M$, z_B and z_C.

Combining (2.24) and (2.28) we obtain

$$\Delta F_R = \sigma T^4(z_{B-}) - F_L^{\downarrow}(z_{B+}) + \Delta F_S \ . \tag{2.32}$$

Thus, if $F_L^{\downarrow}(z_{B+})$ and ΔF_S are known, ΔF_R can be computed from model variables by using (2.31) and (2.32).

2.3 Summary of the combined convective-radiative model

The combined convective-radiative model consists of the surface flux relations (2.3) and (2.4), the cloud base relation (2.10), the definitions (2.7) and (2.8), the cloud top temperature and radiation relations (2.31) and (2.32), the entrainment relation (2.22), the consistency relation (2.9), the mixed layer budgets (2.1) and (2.2) and the cloud top jump condition (2.5). These form a closed set of twelve equations in the twelve unknowns listed in the first column of Table 7. The constants and externally specified parameters required to integrate the model are listed in the second and third columns of Table 7. The governing equations of the combined convective-radiative model can now be arranged for numerical integration as follows:

$$(\overline{w'h'})_S = C_T V[h_S^* - h_M] \ , \tag{2.33}$$

$$(\overline{w'q'})_S = C_T V[q_S^* - (q+\ell)_M] \ , \tag{2.34}$$

$$\frac{z_C}{H} = \frac{(1+\gamma)[q_S^* - (q+\ell)_M] - \frac{\gamma}{L}[h_S^* - h_M]}{b} \ , \tag{2.35}$$

$$\Delta h = h(z_{B+}) - h_M \ , \tag{2.36}$$

$$\Delta(q+\ell) = q(z_{B+}) - (q+\ell)_M \ , \tag{2.37}$$

$$T(z_{B-}) = \frac{1}{c_p}\left[h_M - L(q+\ell)_M + \frac{Lb}{(1+\gamma)H}(z_B - z_C) - gz_B\right] \ , \tag{2.38}$$

$$\Delta F_R = \sigma T^4(z_{B-}) - F_L^{\downarrow}(z_{B+}) + \Delta F_S \ , \tag{2.39}$$

$$\begin{bmatrix} a_{11} & a_{12} \\ a_{21} & a_{22} \end{bmatrix} \begin{bmatrix} (\overline{w'h'})_B \\ L\overline{w'(q'+\ell')}_B \end{bmatrix} = \begin{bmatrix} b_1 \\ b_2 \end{bmatrix} \ , \tag{2.40, 2.41}$$

$$\frac{dh_M}{dt} = \frac{(\overline{w'h'})_S - (\overline{w'h'})_B}{z_B} , \tag{2.42}$$

$$\frac{d(q+\ell)_M}{dt} = \frac{(\overline{w'q'})_S - \overline{w'(q'+\ell')}_B}{z_B} , \tag{2.43}$$

$$\frac{dz_B}{dt} = -Dz_B + \frac{\rho^{-1}\Delta F_R - (\overline{w'h'})_B}{\Delta h} . \tag{2.44}$$

Equations (2.40) and (2.41) are simply a shorthand notation for (2.22) and (2.9). Given initial conditions on h_M, $(q+\ell)_M$ and z_B, the system (2.33) - (2.44) can be numerically integrated. A single computation cycle is as follows:

1. Compute the surface fluxes $(\overline{w'h'})_S$ and $(\overline{w'q'})_S$ from (2.33) and (2.34).
2. Compute cloud base z_C from (2.35).
3. Compute the cloud top jumps in moist static energy and total water from (2.36) and (2.37).
4. Compute the cloud top temperature from (2.38) and then the jump in net radiative flux from (2.39).
5. Compute the cloud top fluxes $(\overline{w'h'})_B$ and $\overline{w'(q'+\ell')}_B$ from the two by two system (2.40) and (2.41).
6. Predict new values of h_M, $(q+\ell)_M$ and z_B from (2.42), (2.43) and (2.44).

The above procedure is straightforward except for step 5. The two by two system (2.40) - (2.41) relates z_B, z_C, $(\overline{w'h'})_S$, $(\overline{w'h'})_B$, $(\overline{w'q'})_S$, $\overline{w'(q'+\ell')}_B$, Δh, $\Delta(q+\ell)$ and ΔF_R. When beginning step 5 we regard z_B, z_C, $(\overline{w'h'})_S$, $(\overline{w'q'})_S$, Δh, $\Delta(q+\ell)$ and ΔF_R as known. Then

(2.40) - (2.41) can be regarded as two equations in the two unknowns $(\overline{w'h'})_B$ and $\overline{w'(q'+\ell')}_B$. However, because of the form of (2.22), the coefficient matrix and the right hand side column vector in (2.40) - (2.41) are unknown until the location of the minimum $\overline{w's_v'}$ is known, i.e. until $(\overline{w'h'})_B$ and $\overline{w'(q'+\ell')}_B$ are known. Thus (2.40) - (2.41) have a somewhat implicit form. Our procedure is to first assume that the minimum $\overline{w's_v'}$ occurs at z_B, solve (2.40) - (2.41) for $(\overline{w'h'})_B$ and $\overline{w'(q'+\ell')}_B$, then using (2.18) check to see if the minimum $\overline{w's_v'}$ actually occurs at z_B. This procedure is repeated for assumptions that the minimum $\overline{w's_v'}$ occurs at z_C- and at the surface. If one and only one of these three possibilities does not lead to a contradiction, we have found the unique solution. It is possible that no solution exists or that more than one solution exists. We have not encountered any problems with existence or uniqueness and have found minimum $\overline{w's_v'}$ fluxes at either the top of the subcloud layer or at the surface.

In section 4 we shall use the above procedure to numerically integrate the system (2.33) - (2.44) under varying sea surface temperature and large-scale divergence. But before studying the horizontally inhomogeneous solutions let us gain deeper insight into model behavior by considering horizontally homogeneous steady state solutions.

3. Horizontally homogeneous steady state solutions

Under steady state horizontally homogeneous conditions the turbulent fluxes of h and $q+\ell$ are constant with height and equal to their surface values. Thus, we can omit the subscript notation from $\overline{w'h'}$ and $\overline{w'(q'+\ell')}$. The subscript notation must be retained on $\overline{w's_v'}$ since this flux is discontinuous at cloud base. In this section it will prove useful to linearize the first term on the right hand side of (2.39), so that

$$\Delta F_R = \sigma T_o^4 \left\{1 + \frac{4}{T_o}\left[T(z_{B+}) - T_o\right]\right\} - F_L^{\downarrow}(z_{B+}) + \Delta F_S \ , \qquad (3.1)$$

where T_o is a constant reference temperature. Typically, the linearization of the blackbody flux results in an underestimate of the upward flux $F_L^{\uparrow}(z_{B+})$ of less than 1% for cloud top temperatures within 10°C of the reference temperature.

Equations (2.3), (2.4), (2.5), (2.7) and (2.31) can now be combined to give

$$\overline{w'h'} = \left(1 + \frac{C_T V}{Dz_B} + \frac{4\sigma T_o^3}{(1+\gamma)\rho c_p Dz_B}\right)^{-1} C_T V$$

$$\cdot \left\{h_S^* - h(z_{B+}) + \frac{1}{\rho D z_B}\left[\sigma T_o^4 + 4\sigma T_o^3\left\{T_S - T_o + \left(\frac{Lb}{(1+\gamma)gH} - 1\right)\frac{g}{c_p} z_B\right\} - F_L^{\downarrow}(z_{B+}) + \Delta F_S\right]\right\} \ , \qquad (3.2)$$

where T_S is the sea surface temperature. Equations (2.4), (2.6) and (2.8) can be combined to give

$$L\overline{w'(q'+\ell')} = \left(1 + \frac{C_T V}{Dz_B}\right)^{-1} C_T V L \left\{q_S^* - q(z_{B+})\right\} \ . \qquad (3.3)$$

With the help of (2.3) and (2.4), the cloud base relation (2.8) can be written

$$\frac{z_C}{H} = (LbC_T V)^{-1}[(1+\gamma)L\overline{w'(q'+\ell')} - \gamma\overline{w'h'}] \ . \tag{3.4}$$

From (2.16) the turbulent fluxes of virtual dry static energy just below cloud top and at the surface are related to $\overline{w'h'}$ and $L\overline{w'(q'+\ell')}$ by

$$(\overline{w's_v'})_B = \beta\overline{w'h'} - \varepsilon L\overline{w'(q'+\ell')} \ , \tag{3.5}$$

$$(\overline{w's_v'})_S = \overline{w'h'} - (1-\varepsilon\delta)L\overline{w'(q'+\ell')} \ . \tag{3.6}$$

The entrainment relation (2.7) takes the form

$$\frac{1-k}{2k}(\overline{w's_v'})_S + (\overline{w's_v'})_B + \frac{z_C}{z_B}\left[(\overline{w's_v'})_S - (\overline{w's_v'})_B\right] = 0 \ . \tag{3.7}$$

Equations (3.2) - (3.7) can be regarded as a closed system in the unknowns z_B, z_C, $\overline{w'h'}$, $L\overline{w'(q'+\ell')}$, $(\overline{w's_v'})_B$ and $(\overline{w's_v'})_S$. In order to reduce this system to a single equation in z_B, we could use (3.4) to eliminate z_C, (3.5) and (3.6) to eliminate $(\overline{w's_v'})_B$ and $(\overline{w's_v'})_S$, and then (3.2) and (3.3) to eliminate $\overline{w'h'}$ and $L\overline{w'(q'+\ell')}$. The resulting equation for z_B is implicit, and, due to its complicated form, is not presented here. We have chosen to compute solutions to the system (3.2) - (3.7) in the following manner:

1. Make an initial guess for z_B.
2. From the current guess of z_B, compute $\overline{w'h'}$ and $L\overline{w'(q'+\ell')}$ from (3.2) and (3.3).
3. Compute z_C, $(\overline{w's_v'})_B$ and $(\overline{w's_v'})_S$ from (3.4), (3.5) and (3.6).

4. If (3.7) is satisfied to within some tolerable error, a solution has been obtained. If not, use the secant method on (3.7) to make an improved estimate of z_B and return to step 2.

We have used this method to compute horizontally homogeneous steady state solutions for sea surface temperatures between 13°C and 18°C and large-scale divergences between 1×10^{-6} and 6×10^{-6} s^{-1}. For those constants which require a reference temperature and/or pressure we have used a reference temperature 4.5°C colder than the sea surface temperature and a reference pressure 4.5 kPa lower than the surface pressure, which is assumed to be 102 kPa. Typical values of the constants are listed in the left column of Table 8. Values of the externally specified parameters are listed in the right column of the table. The functions $h(z_{B+})$ and $q(z_{B+})$ were determined from the mean July 1967-70 Oakland sounding (U. S. Dept. of Commerce, 1967-70) and are plotted in Figures 12a and 12b. The $s(z_B+)$ and $T(z_B+)$ profiles implied by the $h(z_B+)$ and $q(z_B+)$ profiles are shown in Figures 12c and 12d. The function $F_L^{\downarrow}(z_B+)$ was determined by using the same mean July Oakland sounding as input to the long-wave transfer model of Cox (1973). $F_L^{\downarrow}(z_{B+})$ is shown in Figure 13. For ΔF_S we have used the daily averaged value suggested by Lilly (1968).

The results for the horizontally homogeneous steady state case with $k = 0.2$ are shown in Figures 14-18. These figures show isolines of the various model outputs as functions of the large-scale divergence and sea surface temperature. Figure 14a shows that the boundary layer deepens as the large-scale divergence decreases and the sea

TABLE 8. Constants and externally specified parameters. For those constants which depend on a reference temperature and/or pressure, only typical values are given.

Constants	Externally Specified Parameters
$c_p = 1004.5\ Jkg^{-1}K^{-1}$	$1 \times 10^{-6} \leq D \leq 6 \times 10^{-6} s^{-1}$
$C_T = 0.0015$	$V = 7\ ms^{-1}$
$g = 9.80\ ms^{-2}$	$310.29 \leq h_S^* \leq 324.13\ Jkg^{-1}$
$k = 0.2$	$9.27 \leq q_S^* \leq 12.8\ gkg^{-1}$
$\delta = 0.608$	$h(z_{B+}) = 314.4 + 0.00187\ z_B$ $(kJkg^{-1})$
$\sigma = 5.67 \times 10^{-8}\ Wm^{-2}K^{-4}$	$q(z_{B+}) = 4.38 - 0.000614\ z_B$ (gkg^{-1})
	$F_L^{\downarrow}(z_{B+}) = 339.4 - 0.0398\ z_B$ (Wm^{-2})
Constants which depend on reference temperature and/or pressure	$\Delta F_S = 22.3\ Wm^{-2}$
$b = 0.0359$	
$H = 8307\ m$	
$L = 2.47 \times 10^6\ Jkg^{-1}$	
$\beta = 0.533$	
$\gamma = 1.34$	
$\varepsilon = 0.115$	
$\rho = 1.22\ kgm^{-3}$	

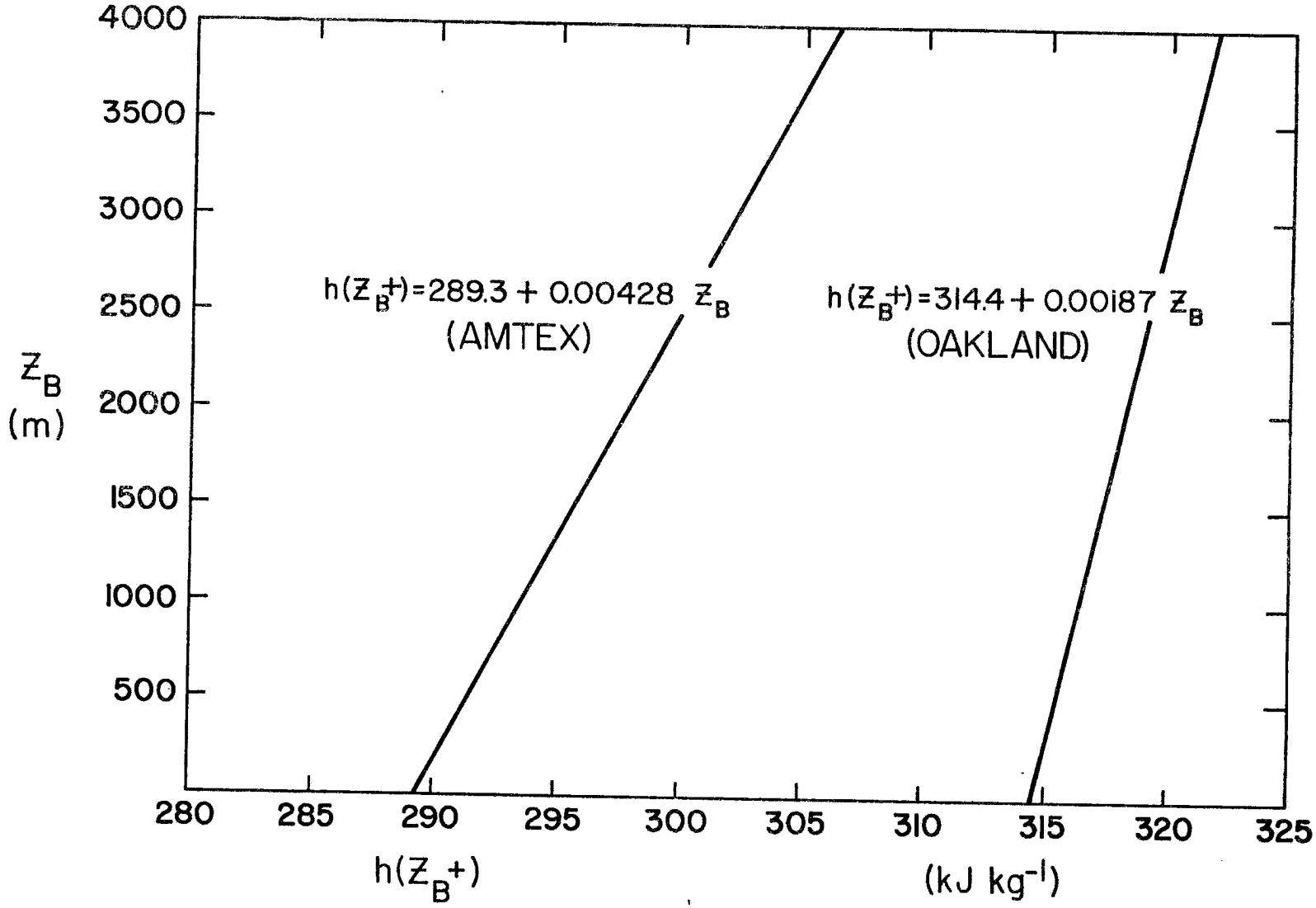

Figure 12a. Moist static energy $h(z_{B+})$ above the mixed layer for the eastern North Pacific as determined from the mean July 1967-70 Oakland sounding and for the East China Sea (AMTEX) as determined from the average of the 00Z and 06Z 16 February 1975 soundings at Ryofu, Naha, and Nojima. The AMTEX case is discussed in section 4.4.

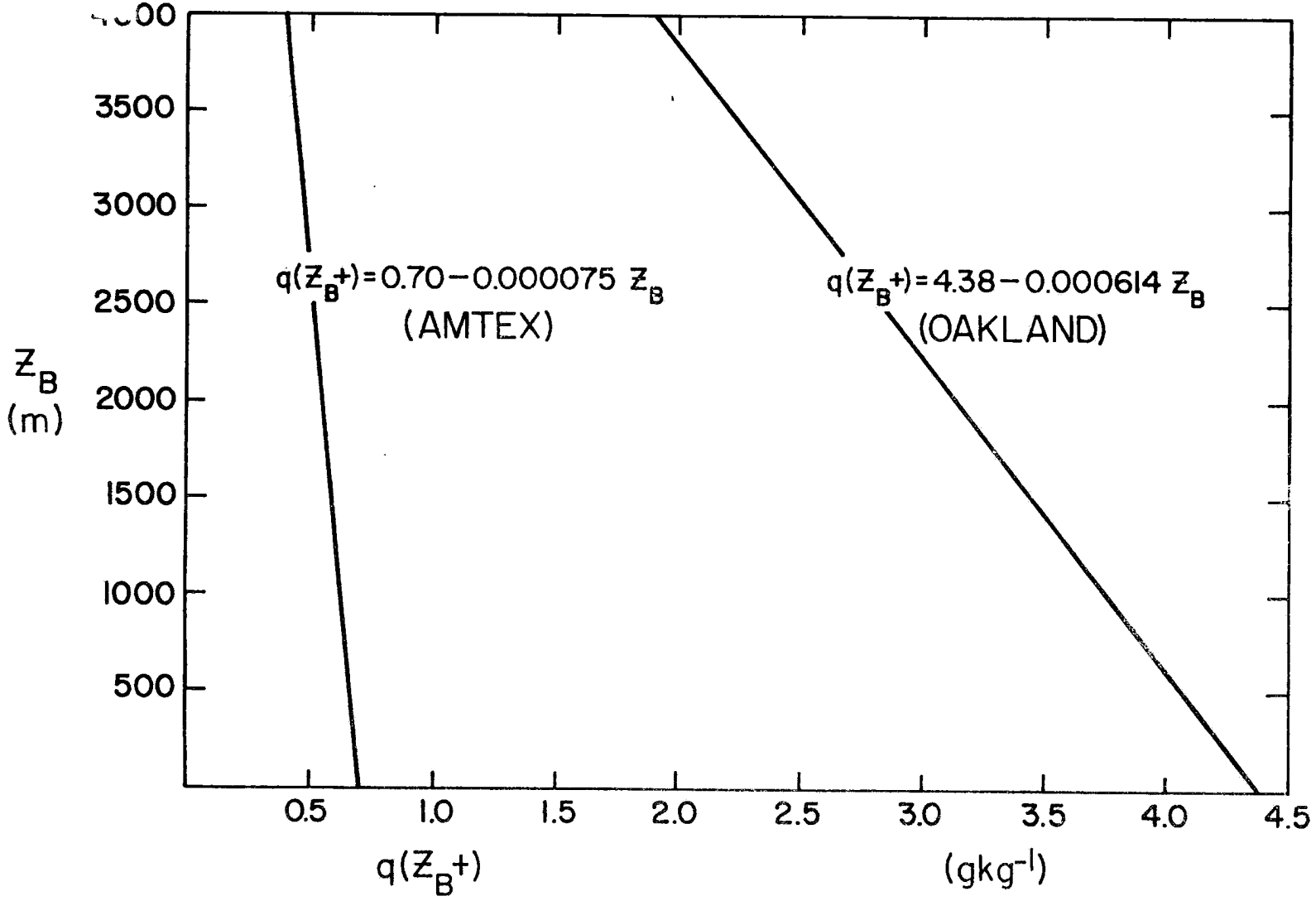

Figure 12b. Water vapor mixing ratio $q(z_{B+})$ above the mixed layer for the eastern North Pacific as determined from the mean July 1967-70 Oakland sounding and for the East China Sea (AMTEX) as determined from the average of the 00Z and 06Z 16 February 1975 soundings at Ryofu, Naha, and Nojima. The AMTEX case is discussed in section 4.4.

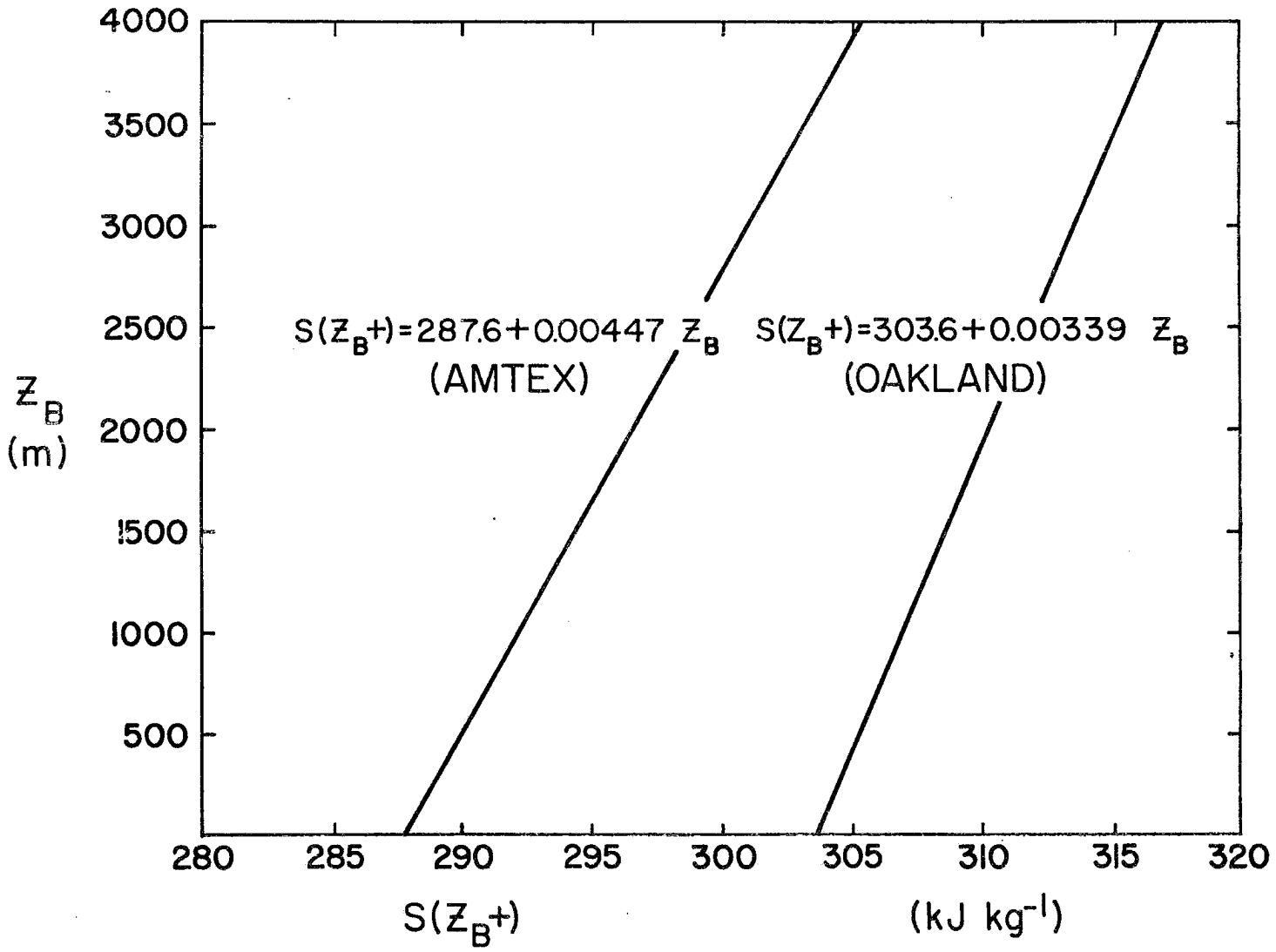

Figure 12c. Dry static energy $s(z_{B+})$ above the mixed layer for the eastern North Pacific as determined from the mean July 1967-70 Oakland soundings and for the East China Sea (AMTEX) as determined from the average of the 00Z and 06Z 16 February 1975 soundings at Ryofu, Naha, and Nojima. The AMTEX case is discussed in section 4.4.

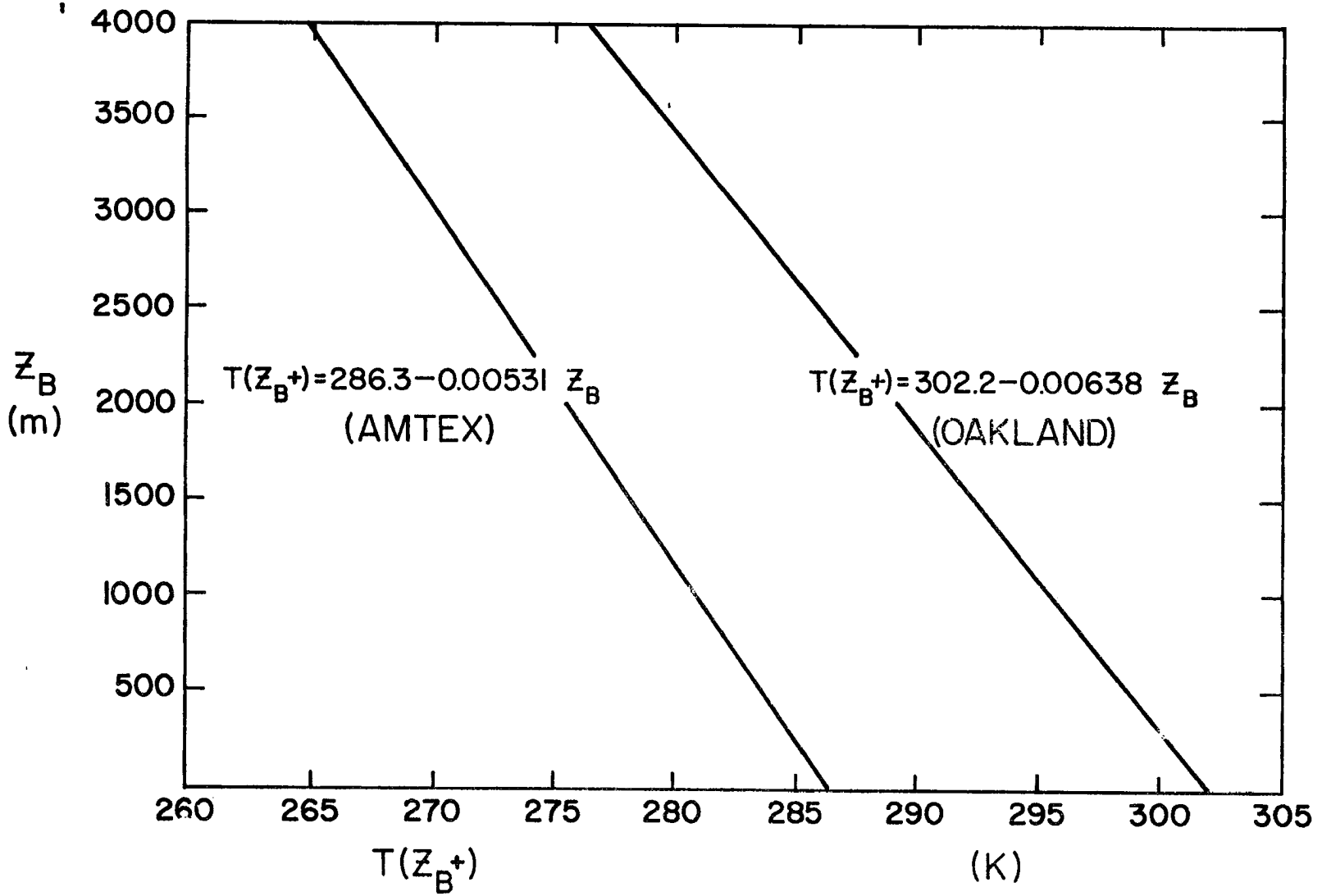

Figure 12d. Temperature $T(z_{B+})$ above the mixed layer for the eastern North Pacific as determined from the mean July 1967-70 Oakland sounding and for the East China Sea (AMTEX) as determined from the average of the 00Z and 06Z 16 February 1975 soundings at Ryofu, Naha, and Nojima. The AMTEX case is discussed in section 4.4.

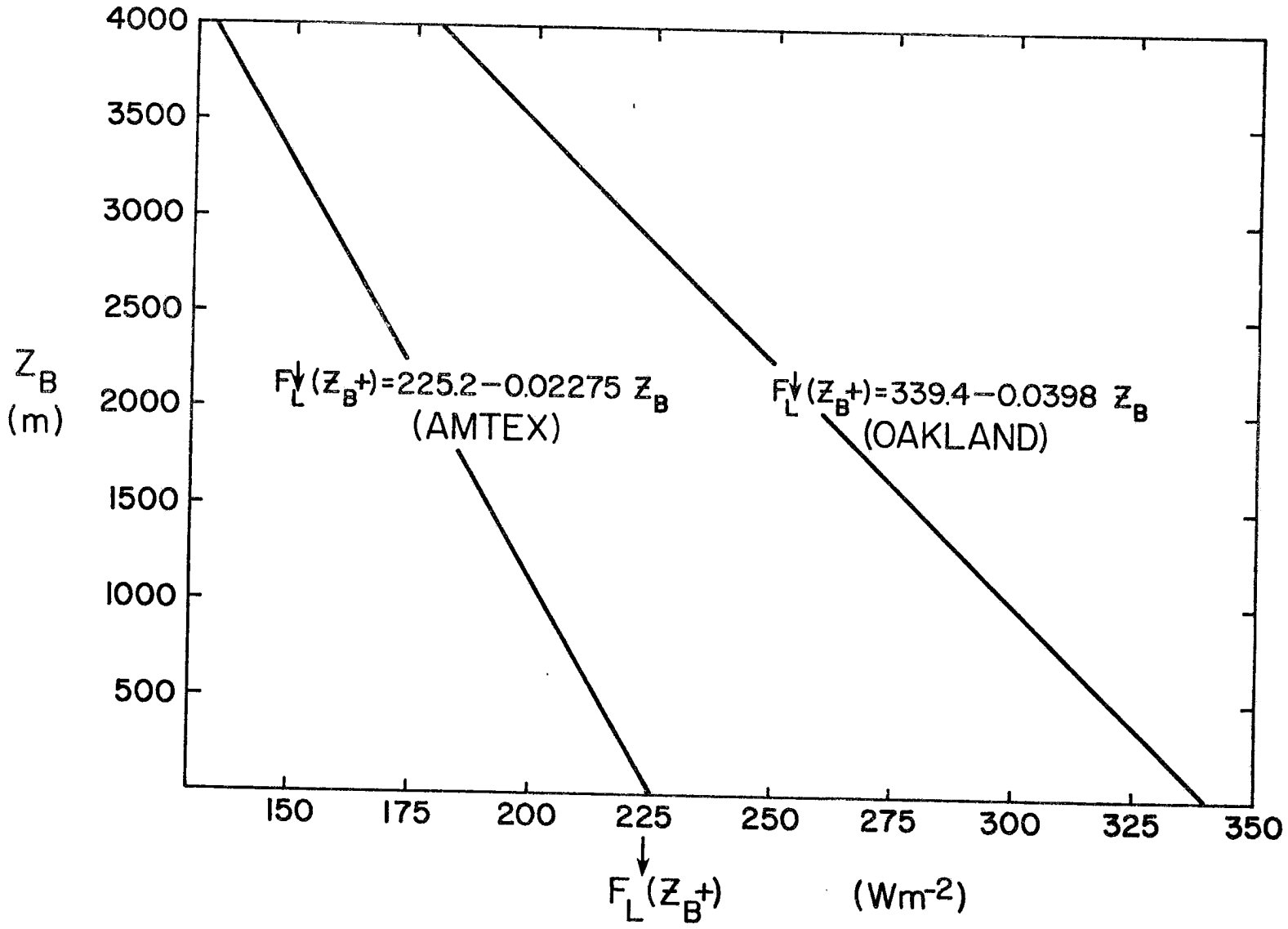

Figure 13. The downward long-wave flux at cloud top as determined by the long-wave transfer model of Cox (1973) using the same temperature and moisture data used in figure 12. Because the wintertime AMTEX situation is so much colder and drier, the corresponding downward long-wave flux is much smaller.

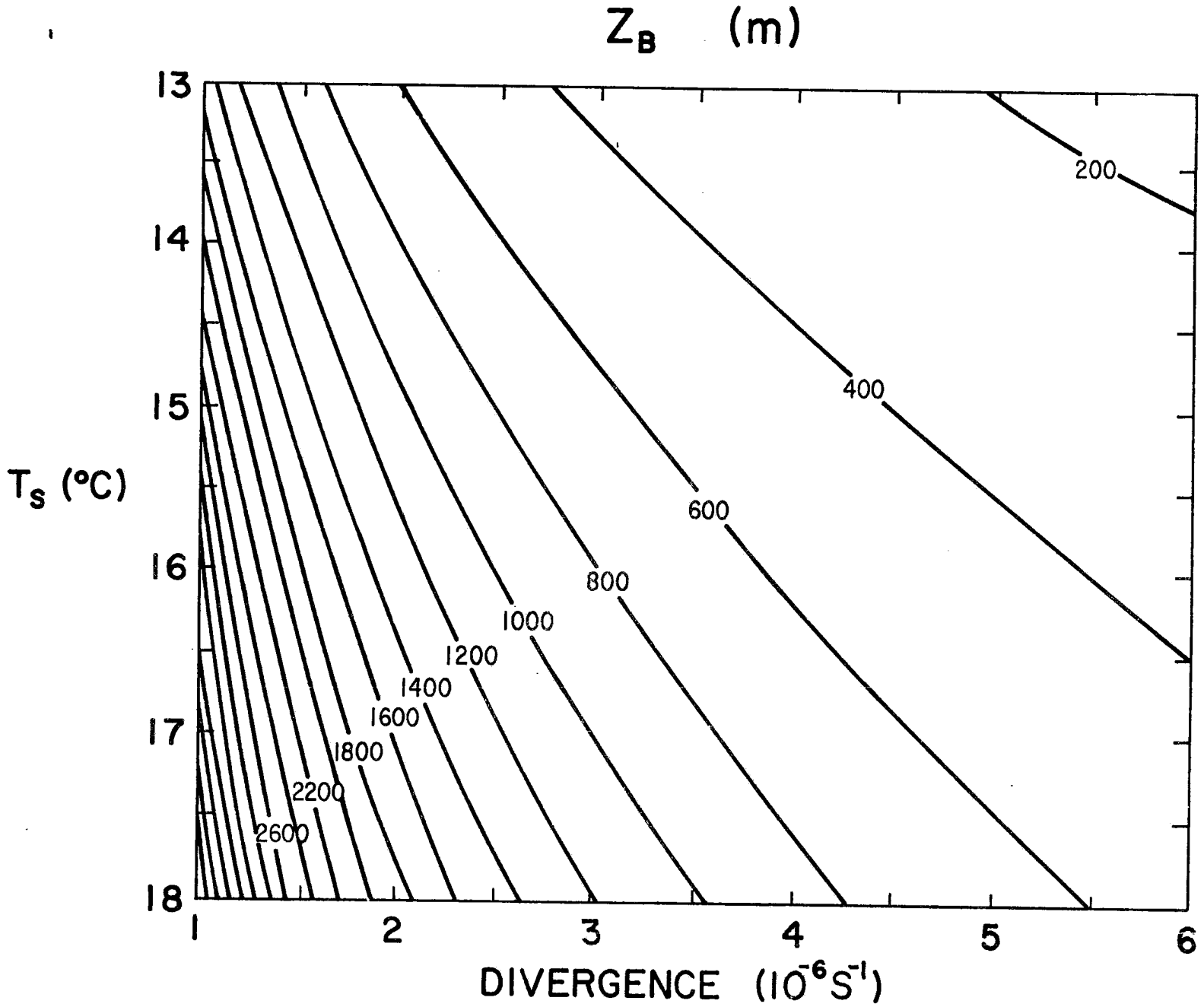

Figure 14a. Isolines of the cloud top height z_B for various large-scale divergences and sea surface temperatures. All other externally specified parameters and constants are given in Table 8.

surface temperature increases. Roughly speaking (see Schubert, 1976, section 3), the boundary layer depth is inversely proportional to the large-scale divergence so that halving the divergence approximately doubles the depth of the boundary layer. Thus, when the large-scale divergence is changed the mixed layer depth changes until an approximately equal cloud top subsidence rate is found (i.e. Dz_B is approximately invariant). Figure 14b shows the cloud base height, which increases as the large-scale divergence decreases and the sea surface temperature increases. The variation of cloud base height is much less than cloud top height so that the appearance of the cloud depth field (Figure 14c) is remarkably similar to that of the cloud top field (Figure 14a).

The upward long-wave flux off cloud top, the downward long-wave flux just above cloud top and the discontinuity in net radiative flux are shown in Figure 15. The upward long-wave flux off cloud top depends on $T(z_{B-})$, which in turn depends on h_M, $(q+\ell)_M$, z_C and z_B as given by (2.31). Most of the variation of $F_L^{\uparrow}(z_{B+})$ is simply related to the fact that $T(z_{B-})$ decreases as cloud top increases. $F_L^{\downarrow}(z_{B+})$ is simply a linear function of z_B as given in Table 8. Thus the isolines of $F_L^{\downarrow}(z_{B+})$ are parallel to the isolines of z_B given in Figure 14a. The discontinuity in the net radiative flux (Figure 15c) is simply $F_L^{\uparrow}(z_{B+}) - F_L^{\downarrow}(z_{B+}) - \Delta F_S$. Since $F_L^{\downarrow}(z_{B+})$ decreases with z_B faster than $F_L^{\uparrow}(z_{B+})$ does, the discontinuity in the net radiative flux increases as z_B increases.

Figure 16 shows the dependence of the mixed layer moist static energy and total water mixing ratio on the divergence and sea surface

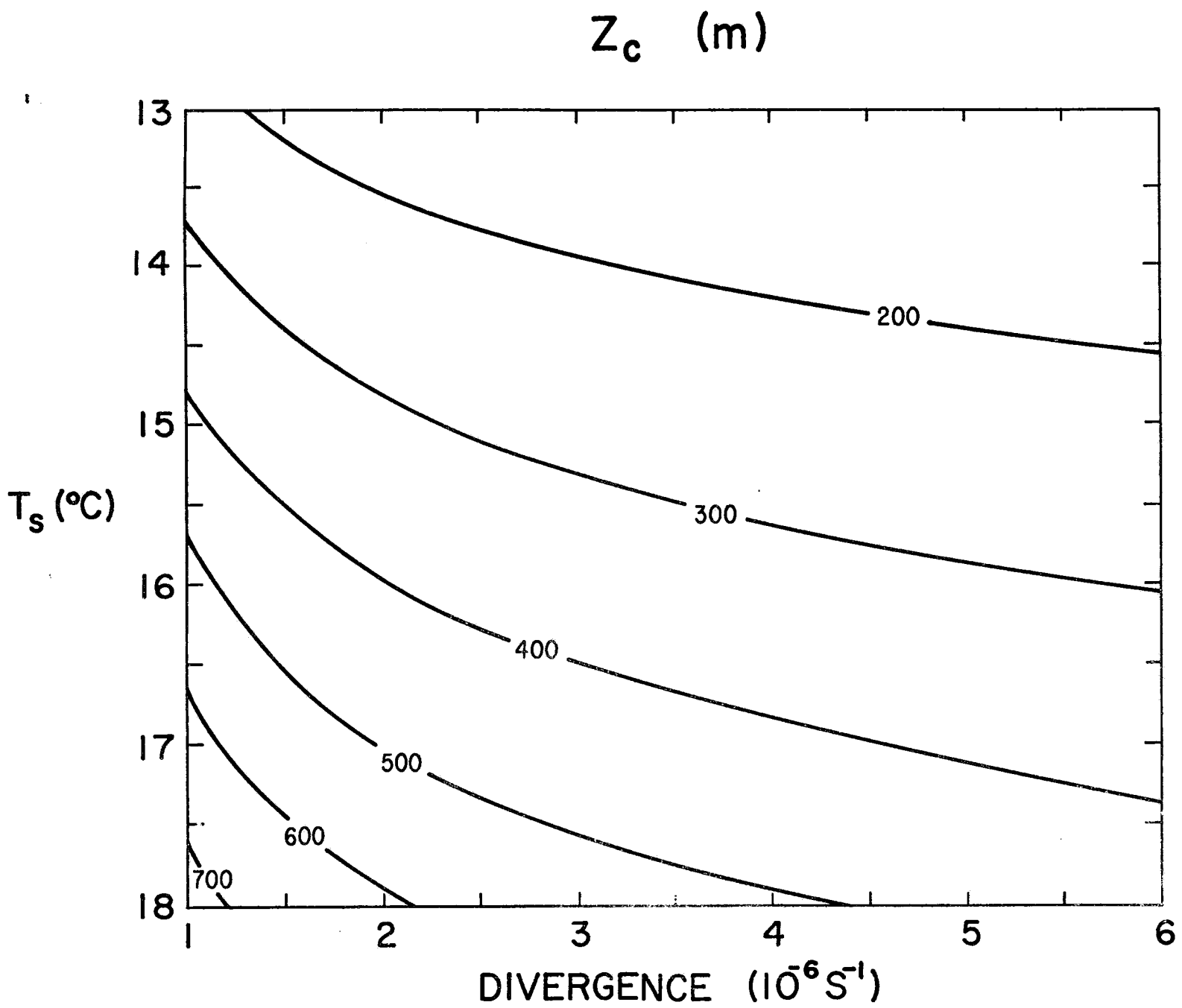

Figure 14b. Isolines of the cloud base height z_c for various large-scale divergences and sea surface temperatures.

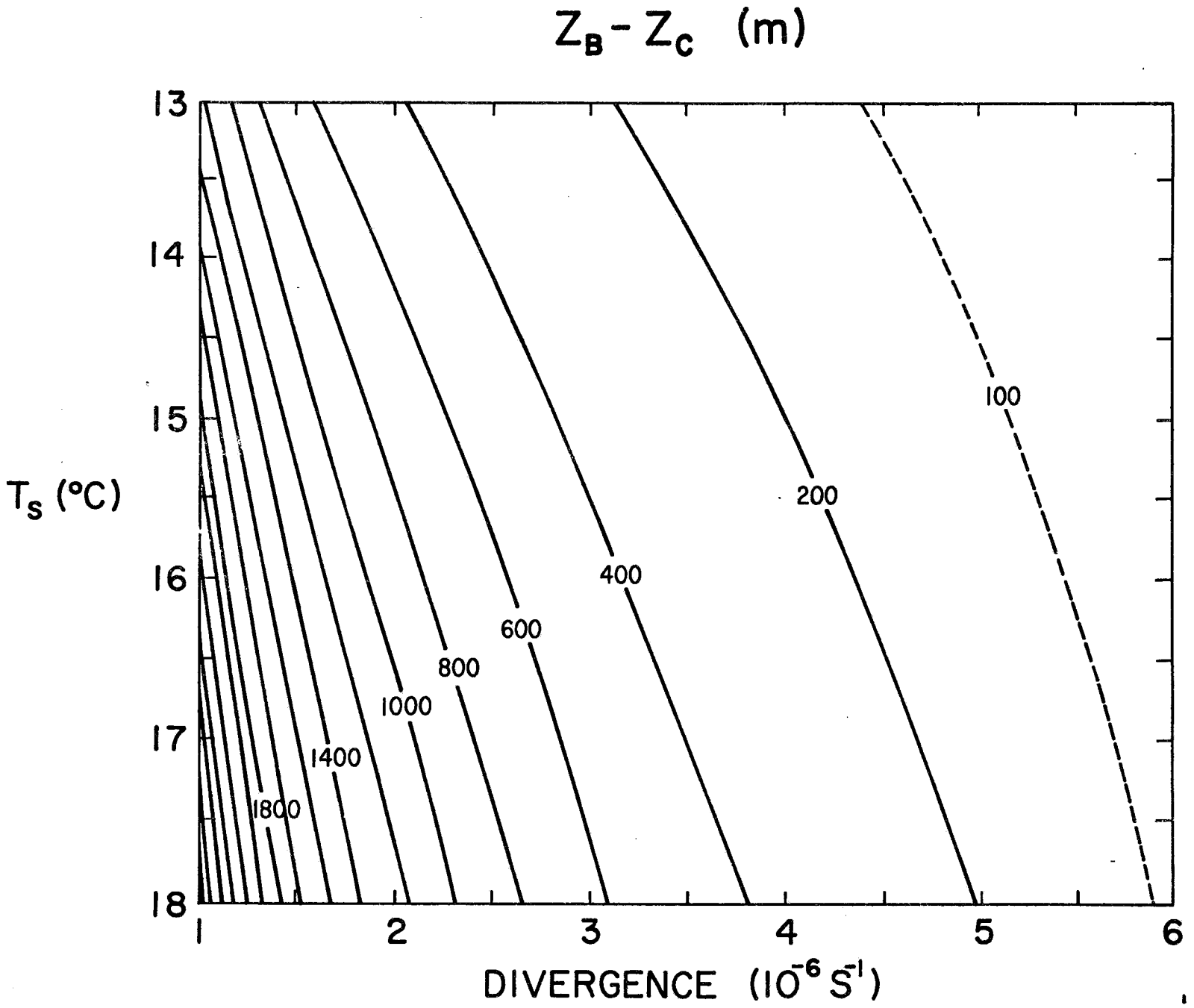

Figure 14c. Isolines of the cloud depth $z_B - z_C$ for various large-scale divergences and sea surface temperatures.

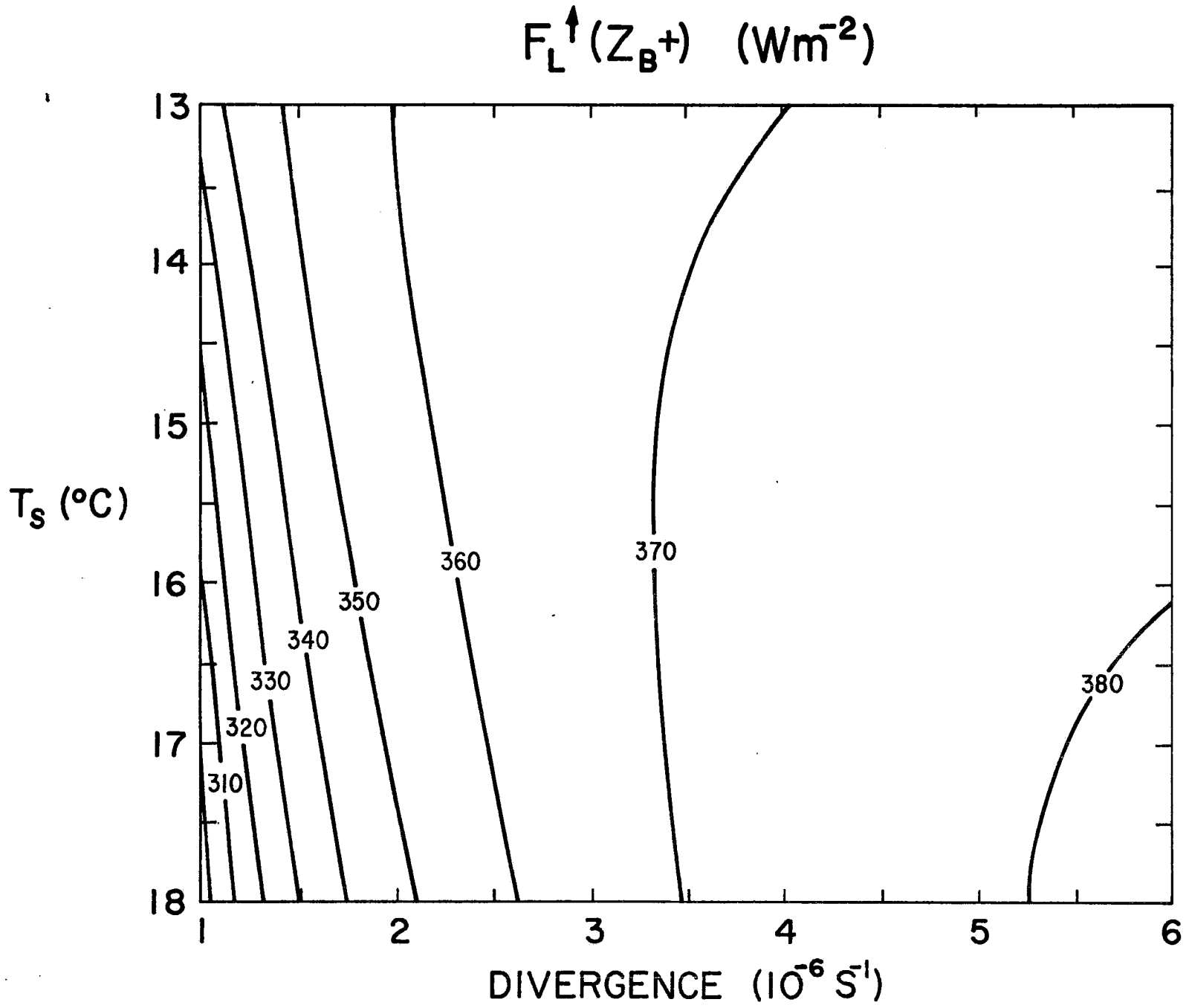

Figure 15a. Isolines of the upward long-wave flux off cloud top $F_L^{\uparrow}(z_{B+})$, which is simply the blackbody flux at $T(z_{B-})$.

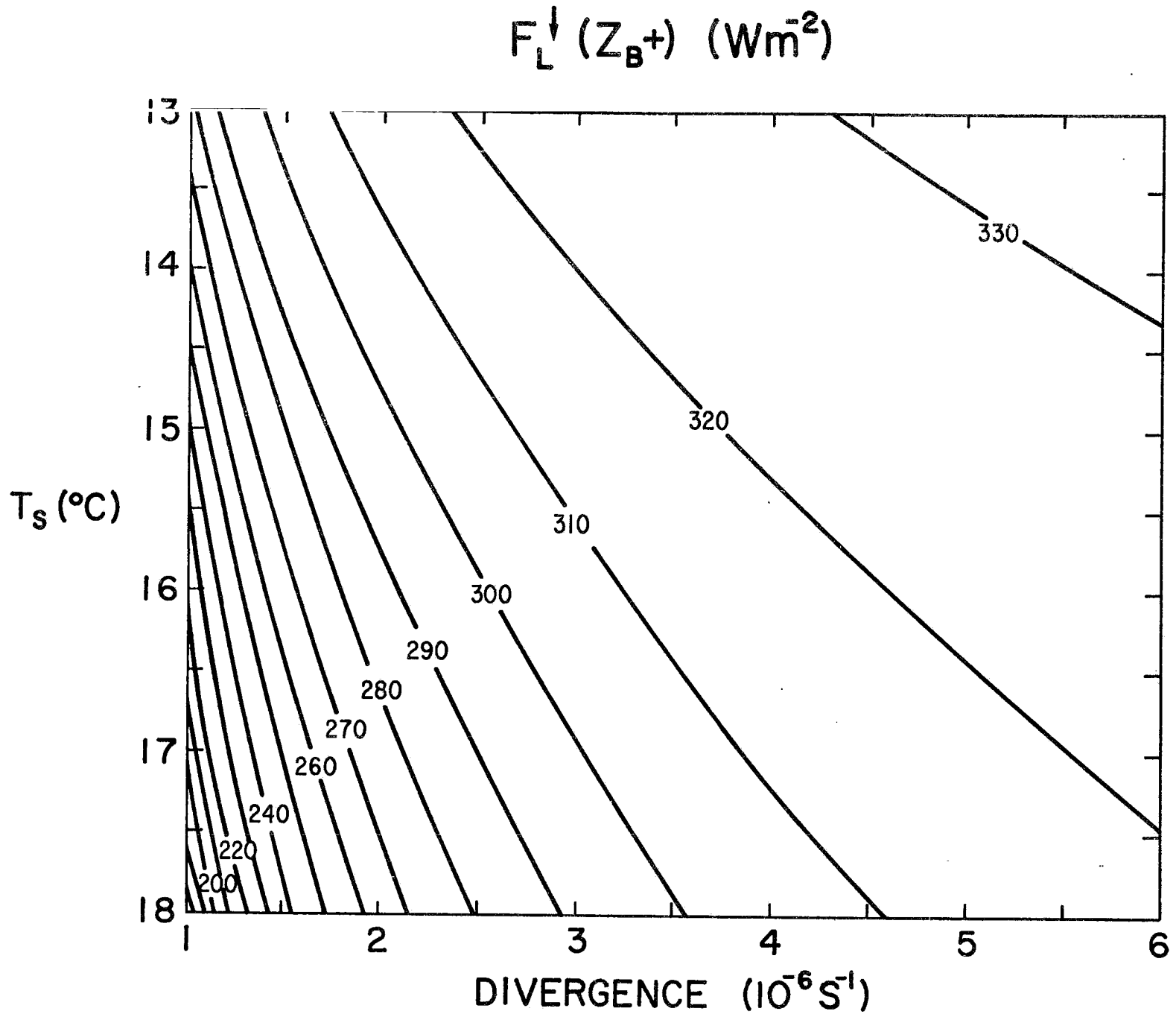

Figure 15b. Isolines of the downward long-wave flux just above cloud top $F_L^{\downarrow}(z_{B^-})$, which was determined from the long-wave transfer model of Cox (1973).

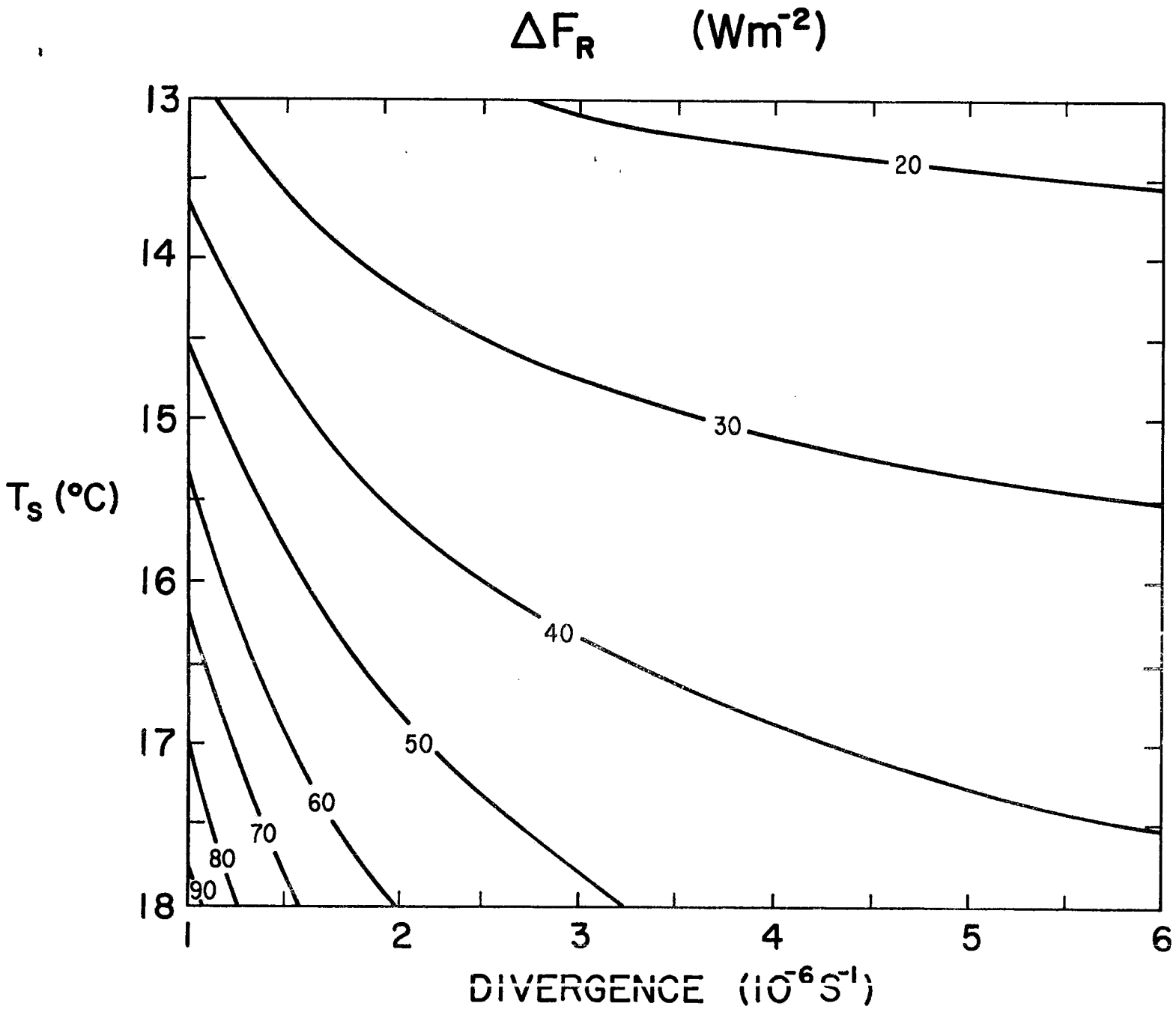

Figure 15c. Isolines of the discontinuity in the net radiative flux ΔF_R, which is simply $F_L^{\uparrow}(z_{B+}) - F_L^{\downarrow}(z_{B+}) + \Delta F_S$.

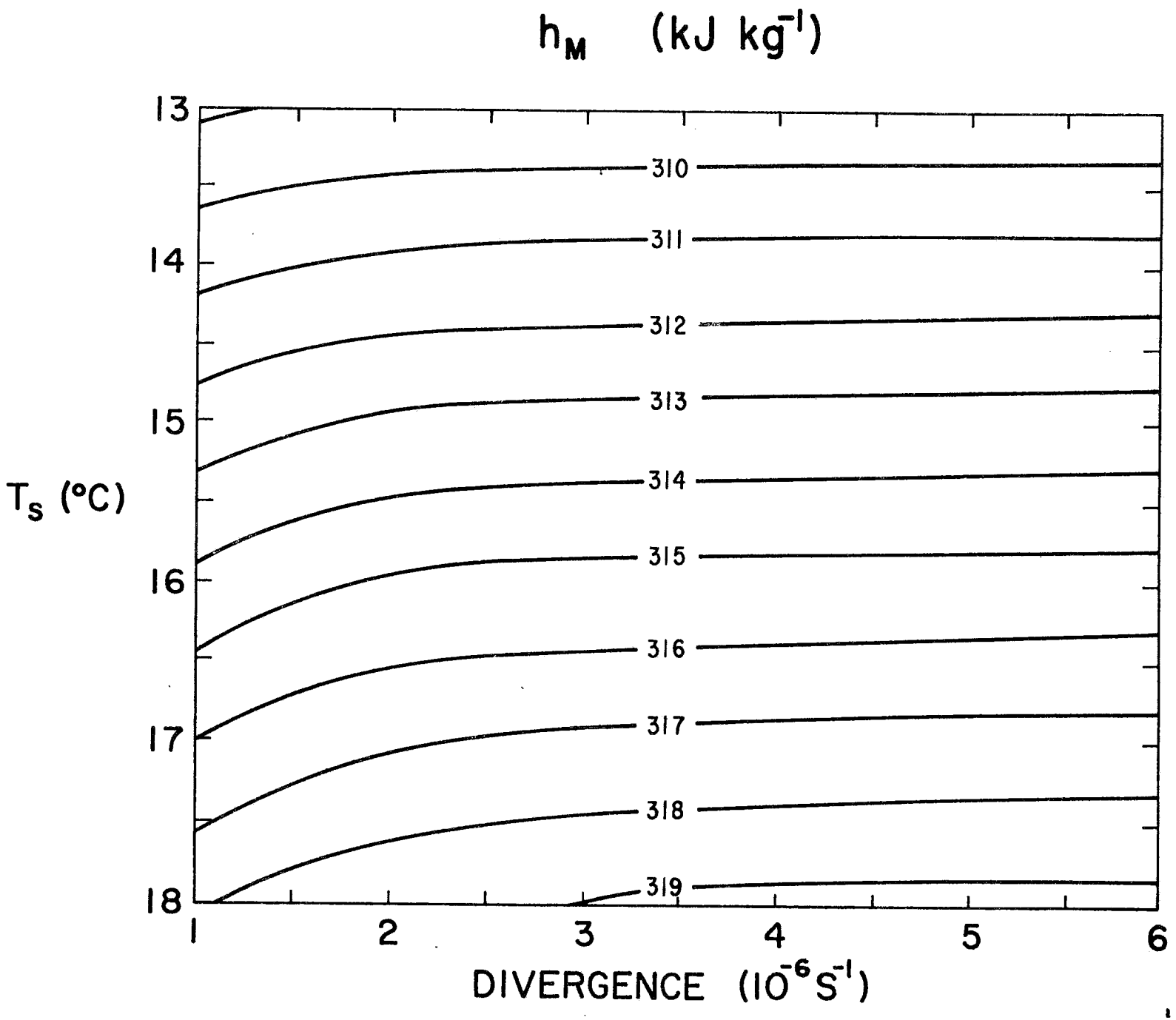

Figure 16a. Isolines of the mixed layer moist static energy h_M.

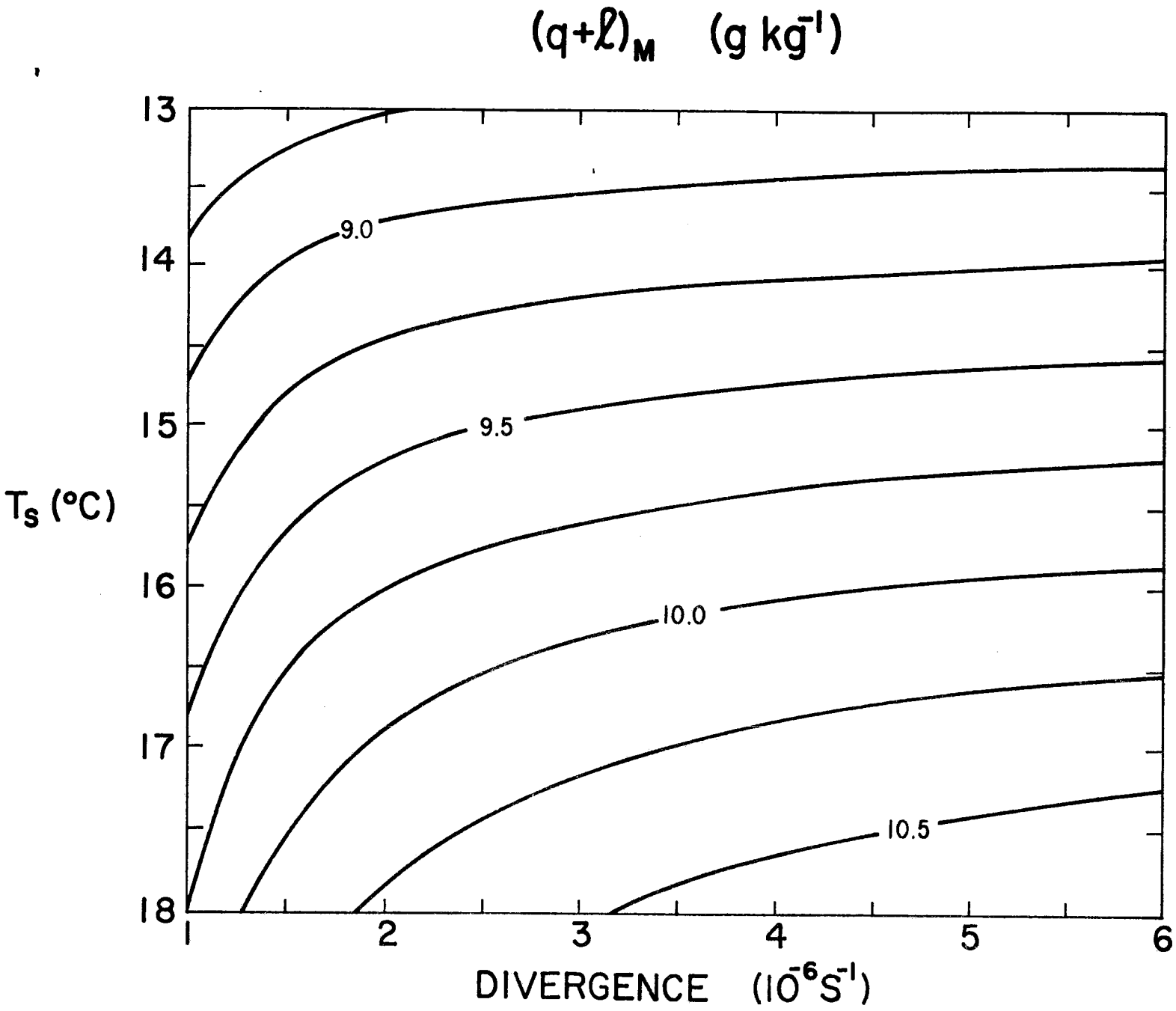

Figure 16b. Isolines of the mixed layer total water mixing ratio $(q+\ell)_M$.

temperature. Except for very small divergences both h_M and $(q+\ell)_M$ are fairly independent of the divergence.

The cloud top jumps of moist static energy and temperature are shown in Figure 17. The temperature inversion at cloud top tends to be quite large (between 8 and 16°C). However, even with such strong temperature inversions the extremely dry air above cloud top can lead to a negative jump in the moist static energy across cloud top. As discussed by Lilly (1968), a cloud-topped mixed layer with $\Delta h < 0$ is possibly unstable. A crude argument is as follows. If a parcel of air just above z_B with moist static energy $h(z_{B+})$ is displaced downward across z_B and mixed with a parcel of cloud layer air with moist static energy h_M, the resulting parcel has intermediate moist static energy, $h(z_{B+}) < h_{parcel} < h_M$. If the resulting parcel is saturated, the difference between h_{parcel} and h_M (which is equal to h* in the cloud layer) is proportional to the temperature difference between parcel and environment, i.e. the parcel buoyancy.[1] Since $h_{parcel} < h_M$, negative buoyancy and instability results. Since this instability mechanism is not recognized by Lilly's model, results with $\Delta h < 0$ must be interpreted with caution. Figure 17a indicates that, with the external parameters specified in Table 8, stable horizontally homogeneous steady state stratocumulus clouds are limited to conditions with sea surface temperatures colder than about 16-17°C.

The turbulent fluxes of moist static energy, total water, liquid water static energy and virtual dry static energy are shown in Figure 18. The fluxes of moist static energy (Figure 18a) and total water

[1]This argument neglects virtual temperature effects.

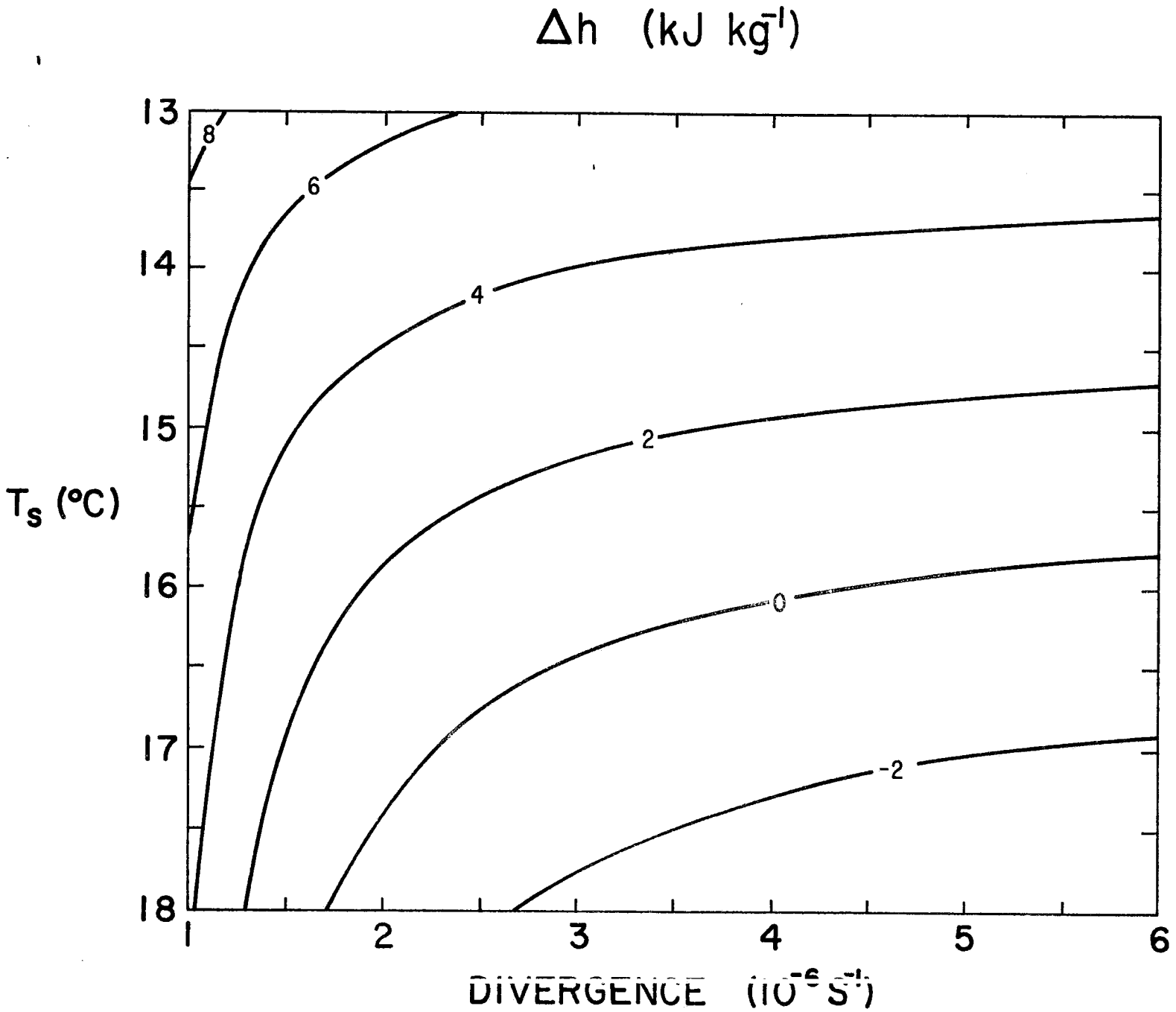

Figure 17a. Isolines of the cloud top jump of moist static energy. The possibility of instability (see text) exists in the region where $\Delta h < 0$.

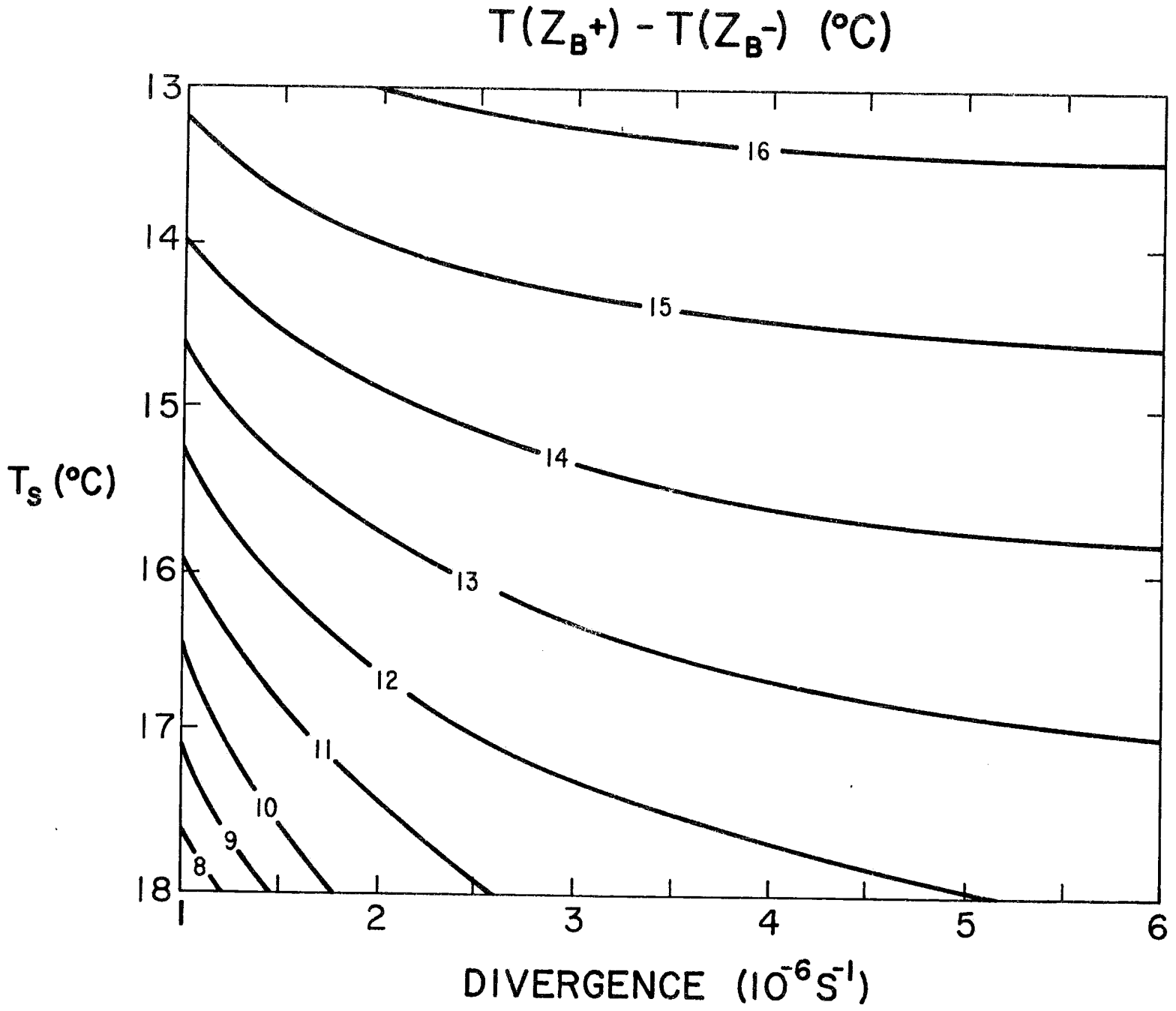

Figure 17b. Isolines of the cloud top jump of temperature.

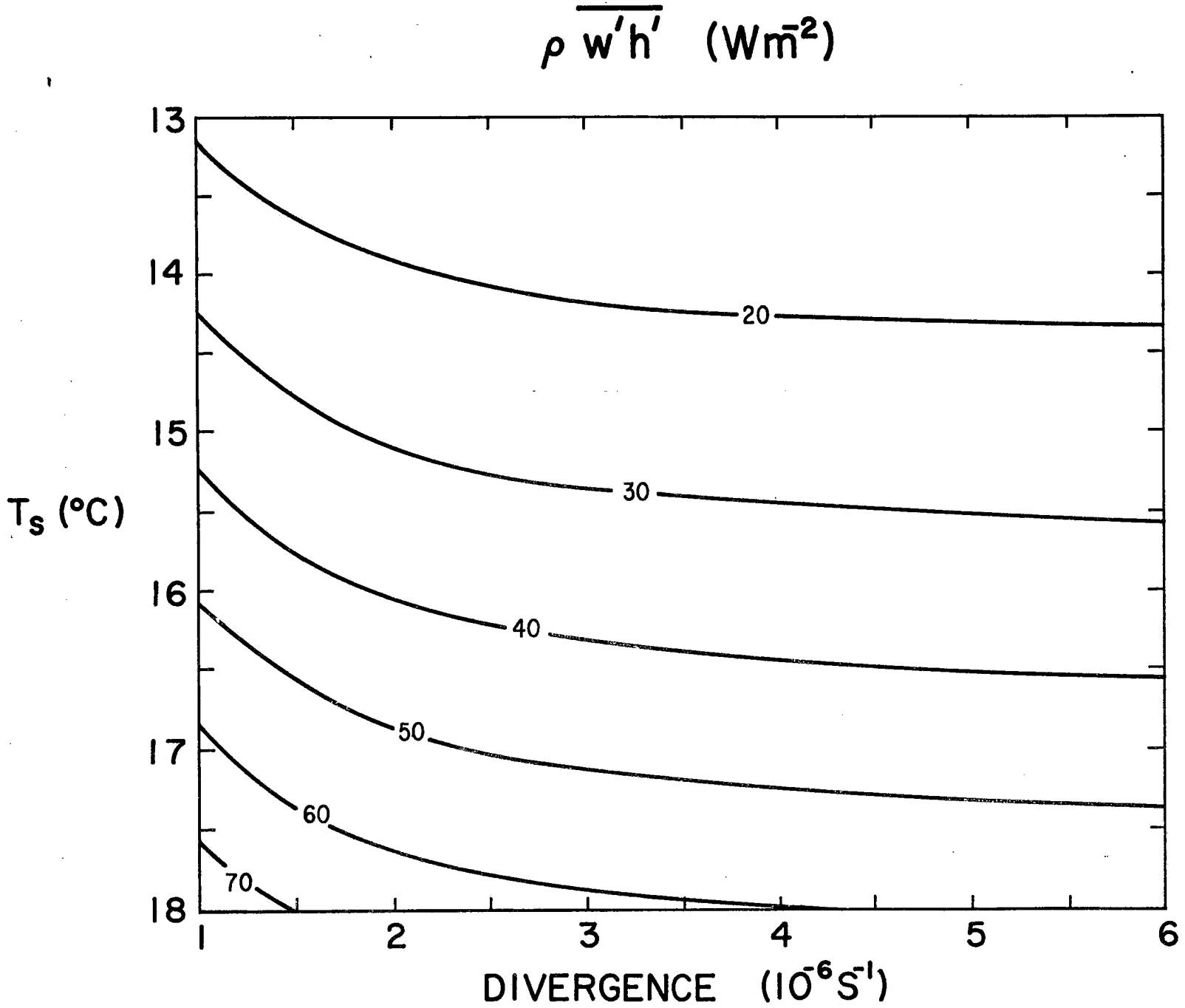

Figure 18a. Isolines of the turbulent flux of moist static energy $\rho\overline{w'h'}$.

(Figure 18b) are fairly independent of divergence except for small values of divergence. The total water flux everywhere exceeds the moist static energy flux, which leads to a negative flux of liquid water static energy (Figure 18c), i.e. a negative heat flux at the surface. There is considerable increase in both $\rho\overline{w'h'}$ and $\rho L\overline{w'(q'+\ell')}$ as sea surface temperature increases. The cloud layer and subcloud layer fluxes of virtual dry static energy (Figures 18d and 18e) are simply computed from (3.5) and (3.6). The subcloud layer flux is always negative and there is a considerable jump to positive values of virtual dry static energy flux in the cloud layer.

The virtual dry static energy flux is not the only flux which is discontinuous across cloud base. The heat flux $\overline{w's'}$, the water vapor flux $\overline{w'q'}$ and the liquid water flux $\overline{w'\ell'}$ are all discontinuous across cloud base as can easily be seen through the use of (2.17). Although the three basic fluxes $\overline{w's'}$, $\overline{w'q'}$, and $\overline{w'\ell'}$ are all discontinuous across z_C, they are discontinuous in such a way that $\overline{w'h'}$, $L\overline{w'(q'+\ell')}$, and hence $\overline{w'(s'-L\ell')}$, are continuous across z_C, as shown schematically in Figure 19. The turbulent flux discontinuities across z_B are readily understandable since the turbulent fluxes in the air above z_B must vanish. However, understanding the turbulent flux discontinuities across z_C is more difficult since these discontinuities are not accompanied by discontinuities in s, q or ℓ. For example, since $L\overline{w'q'}$ jumps to a lower value and $L\overline{w'\ell'}$ jumps from zero to a positive value across z_C, there is a finite amount of condensation in the infinitesimally thin layer centered at cloud base. The net condensation at cloud base is balanced by the net evaporation at cloud top. This may at first

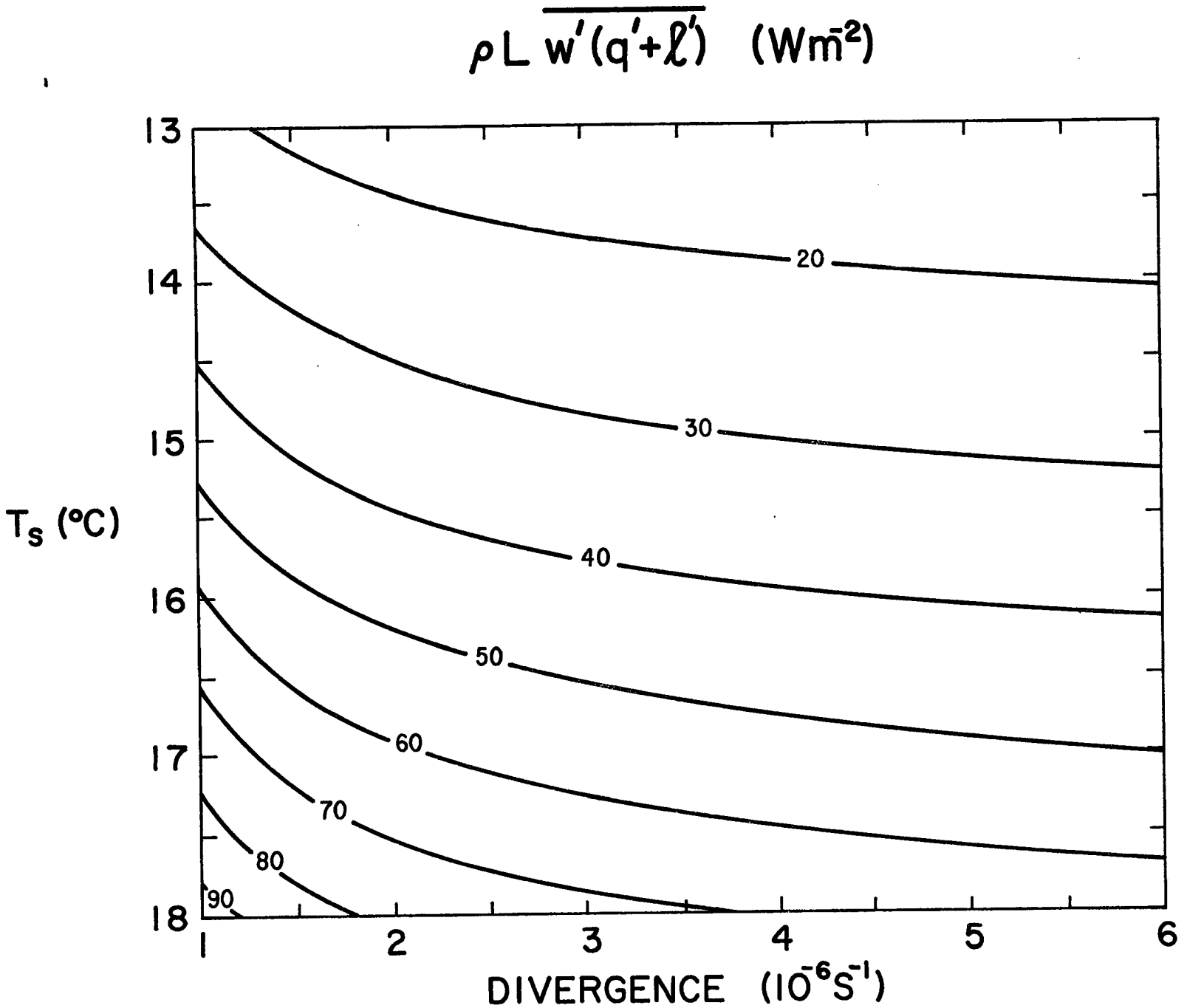

Figure 18b. Isolines of the turbulent flux of total water $\rho L\overline{w'(q'+\ell')}$.

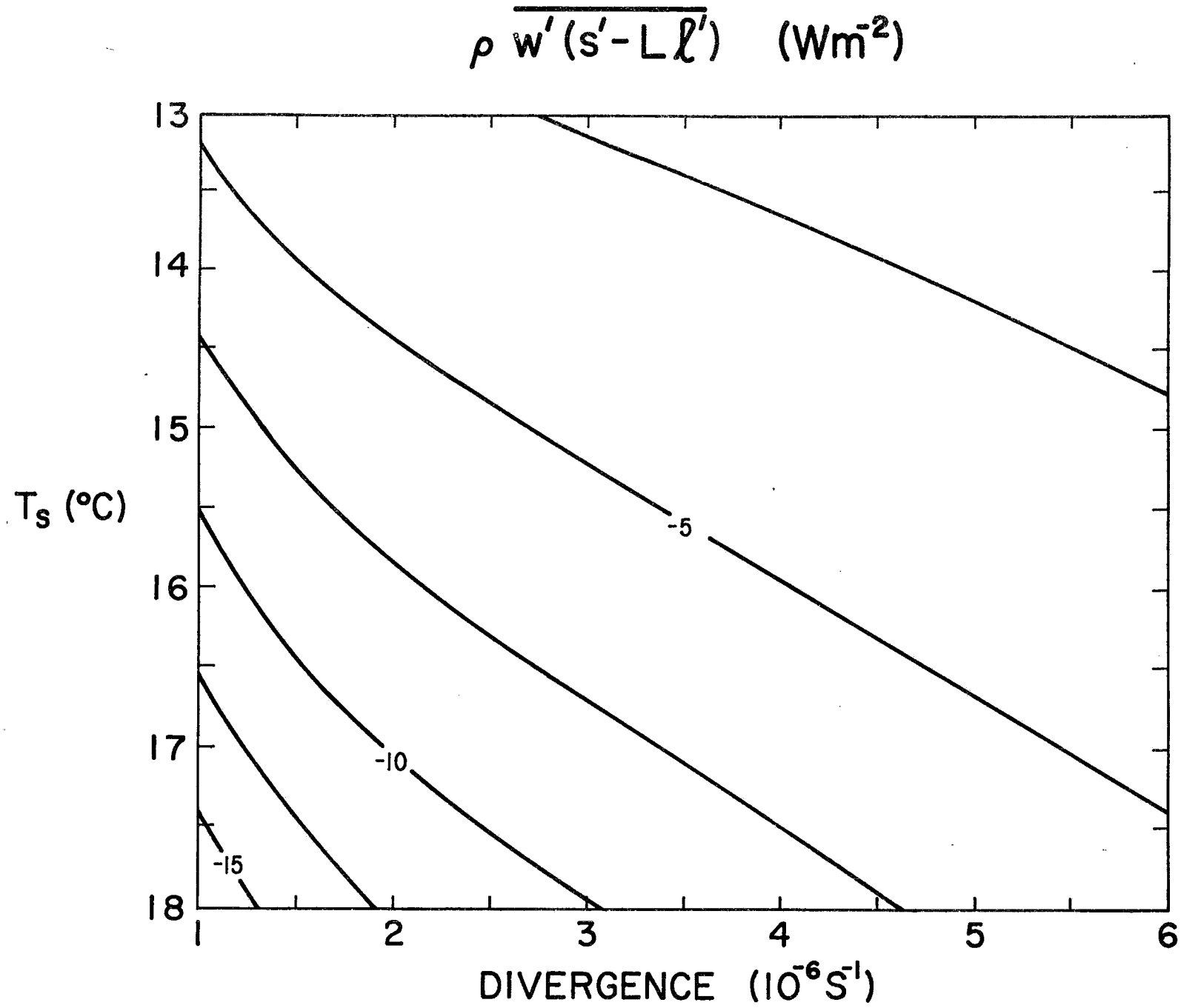

Figure 18c. Isolines of the turbulent flux of liquid water static energy $\rho\overline{w'(s'-L\ell')}$.

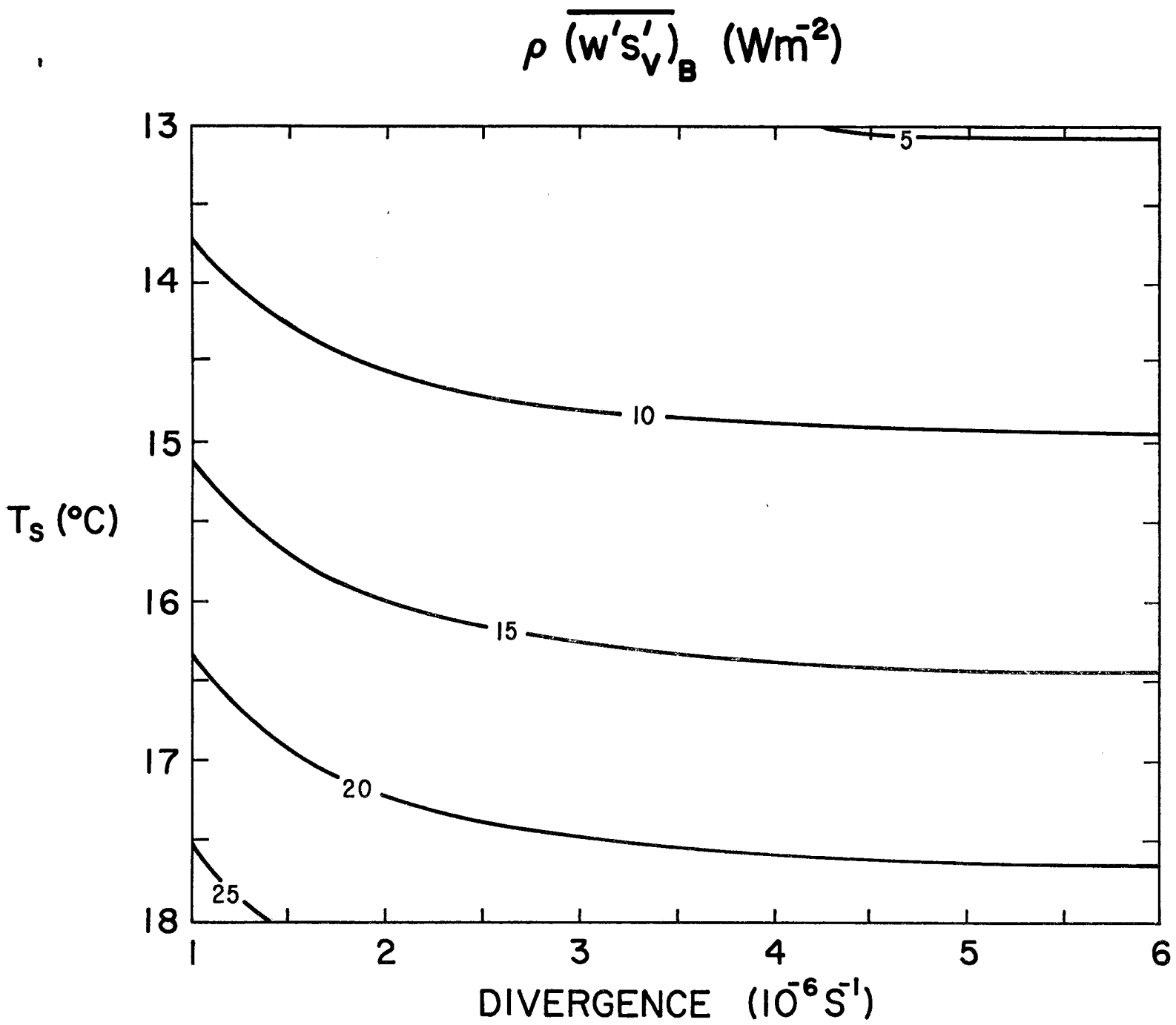

Figure 18d. Isolines of the turbulent flux of virtual dry static energy at cloud top $\rho(\overline{w's_v'})_B$.

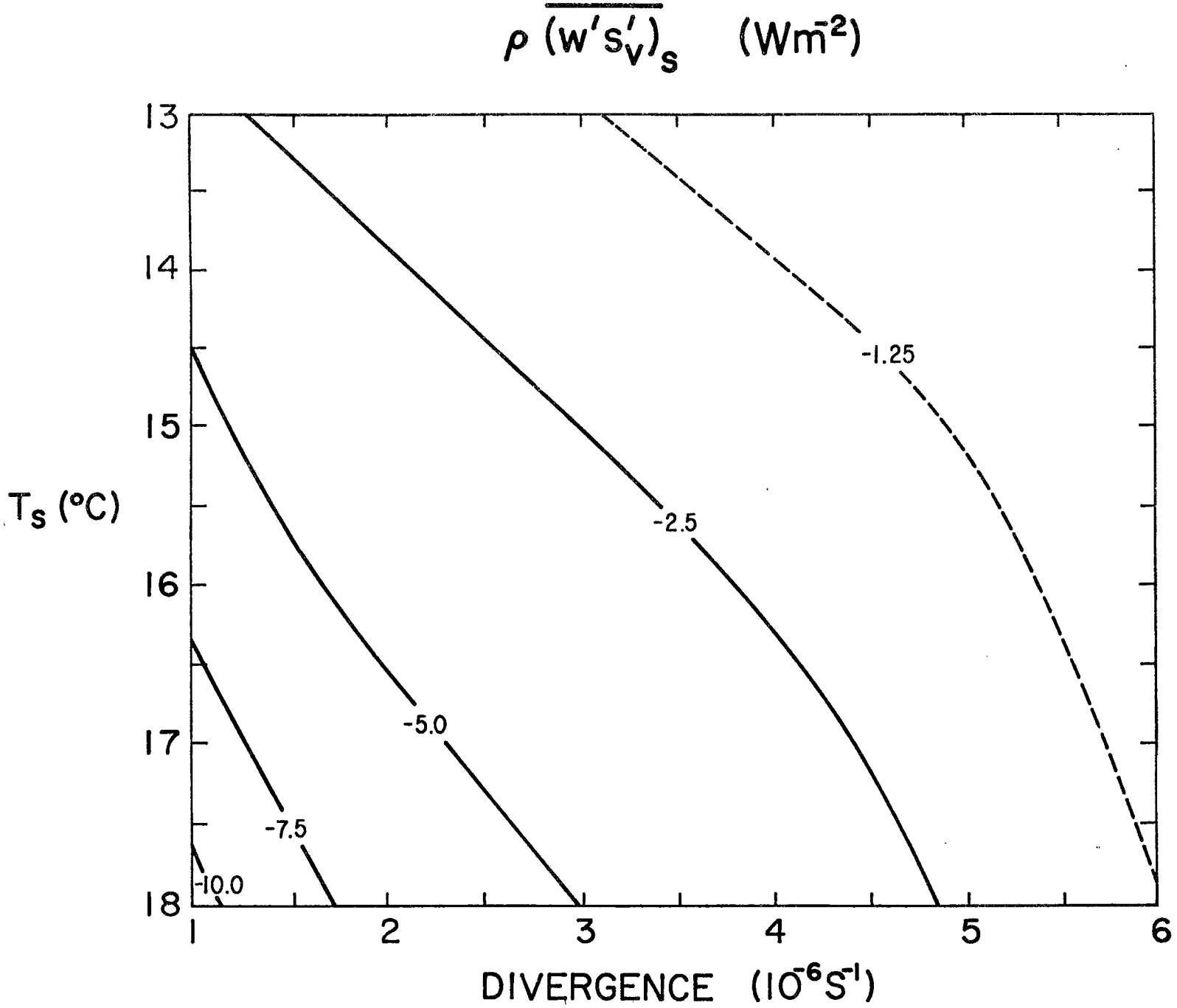

Figure 18e. Isolines of the turbulent flux of virtual dry static energy at the surface $\rho\overline{(w's'_v)}_s$.

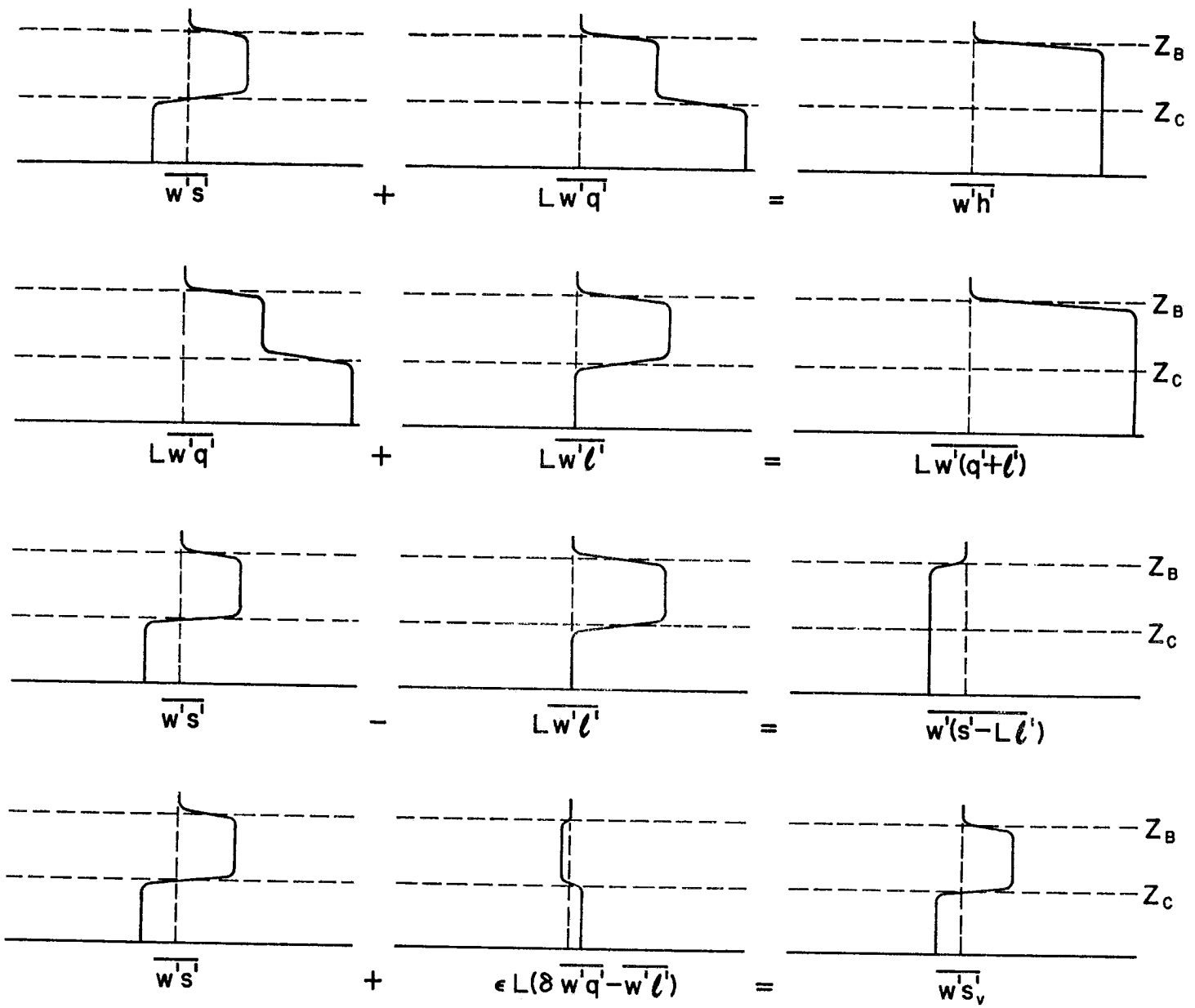

Figure 19. Profiles of the three basic fluxes $\overline{w's'}$, $L\overline{w'q'}$ and $L\overline{w'\ell'}$ and their combinations to form $\overline{w'h'}$, $L\overline{w'(q'+\ell')}$ and $\overline{w'(s'-L\ell')}$. These profiles are typical of steady state horizontally homogeneous conditions.

sight seem strange, but it can be understood in terms of a convective element model. Although a convective element model is not explicit in the theory, let us proceed to interpret the jumps in $\overline{w's'}$, $L\overline{w'q'}$, and $L\overline{w'\ell'}$ at z_C in terms of such a model.

Consider a parcel of air which is circulating in the mixed layer. Figures 20 and 21 illustrate schematically the parcel paths of the energy and moisture parameters and their associated fluxes. The conservative quantities h and $(q+\ell)$ (and their difference $s-L\ell$) are shown in Figure 20. The nonconservative quantities s, q and ℓ, which are somewhat more complicated, are shown in Figure 21. As the parcel ascends along a dry adiabat from the ocean surface it conserves s, q and ℓ (which is zero) until it reaches z_{C-}, a point just below z_C. At this point, the parcel is saturated and its further ascent is along a wet adiabat. Along the wet adiabat s and ℓ increase and q decreases, all in such a way that h, $(q+\ell)$ and $(s-L\ell)$ are conserved. When the saturated and water bearing parcel crosses z_B, it mixes with some of the warm and dry air above z_B. The warmth of the entrained air tends to warm the parcel but its dryness tends to cool the parcel by evaporating enough liquid water to maintain saturation. In addition to this evaporative cooling, the parcel is also cooled radiatively since the air below is cloudy and the air above is clear. The sum of the evaporative and radiative cooling overwhelms the entrainment warming and the parcel begins descent along a wet adiabat at a lower temperature, a lower water vapor mixing ratio, and a lower liquid water mixing ratio. Since the liquid water mixing ratio is lower, the wet adiabatic descent cannot continue to z_{C-} but terminates at z_{C+}, a point just

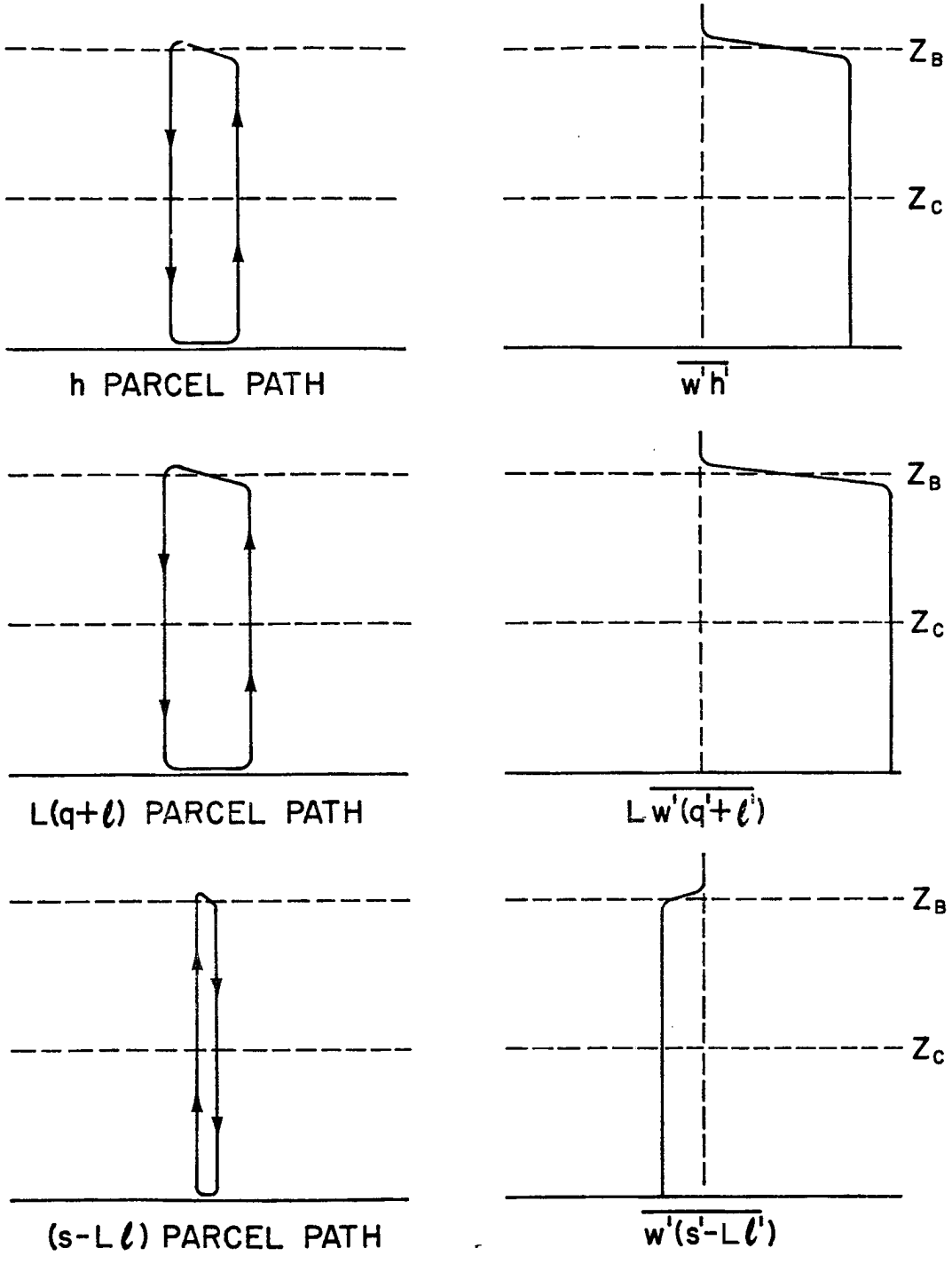

Figure 20. Typical parcel paths of the conservative quantities h, L(q+ℓ) and s-L and the resulting fluxes $\overline{w'h'}$, $L\overline{w'(q'+\ell')}$ and $\overline{w'(s'-L\ell')}$.

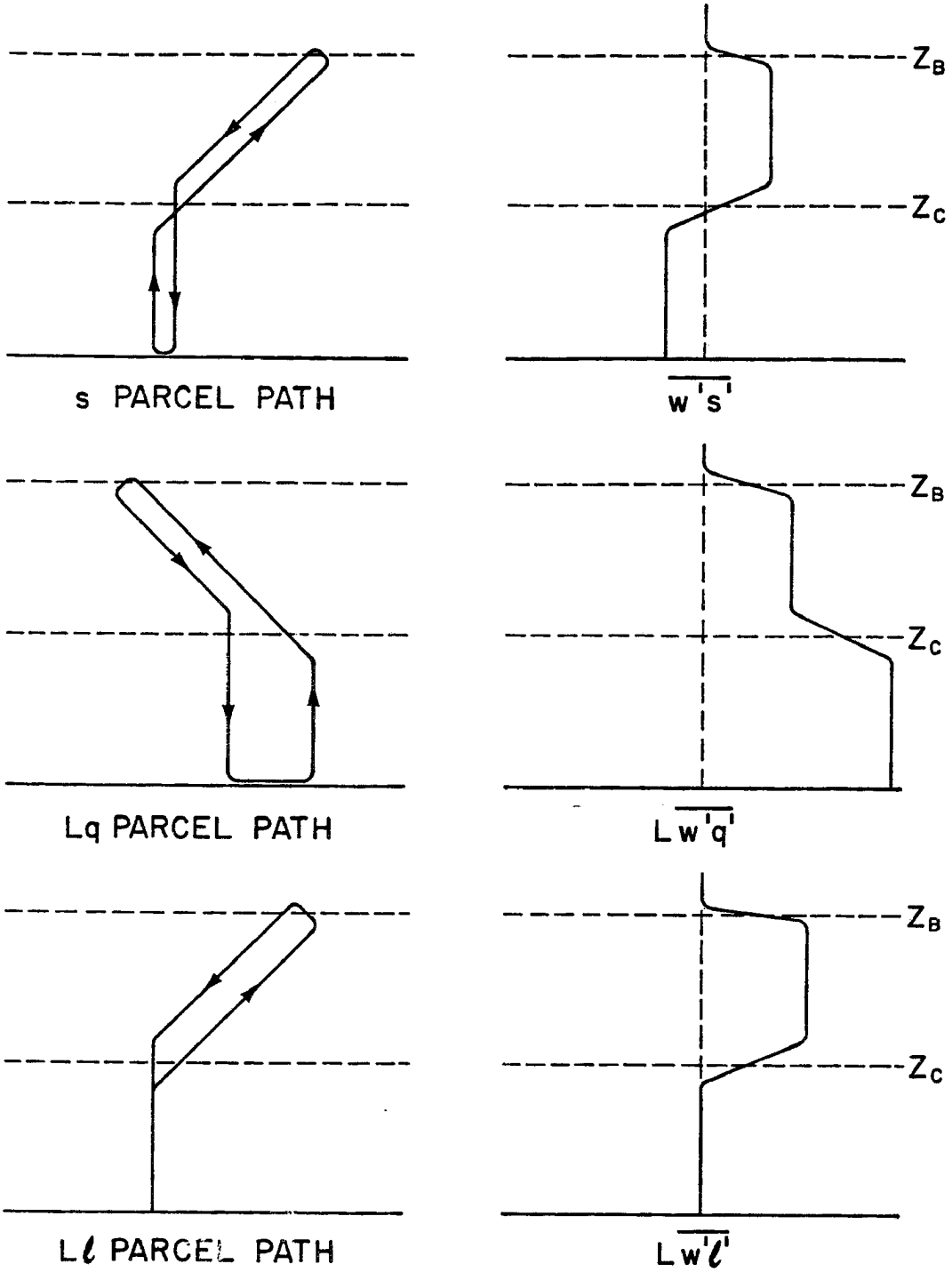

Figure 21. Typical parcel paths of the nonconservative quantities s, Lq and Lℓ and the resulting fluxes $\overline{w's'}$, $\overline{Lw'q'}$ and $\overline{Lw'\ell'}$. Note that in the major portion of the cloud there is no net condensation and $\overline{Lw'\ell'}$ is constant with height. The net condensation at cloud base is balanced by the net evaporation at cloud top.

above z_C. Descent below z_{C+} is along a dry adiabat with s, q and ℓ (which is again zero) being conserved. Upon arriving at the surface the descending parcel gives up heat to the ocean and receives water vapor from the ocean, and then begins another circuit.

If the mixed layer is horizontally homogeneous and is in a locally steady state, every parcel circuit is identical. This is the situation illustrated in Figures 19-21. If the mixed layer is not horizontally homogeneous or is not in a locally steady state, parcel circuits are not identical and the mixed layer may be changing its h_M, $(q+\ell)_M$, z_B, etc. We shall discuss the horizontally inhomogeneous situation further in section 4.

A prediction of the horizontally homogeneous steady state theory is that $\overline{w's_v'}$ is negative below cloud base, i.e. upward moving parcels in the subcloud layer are virtually colder than downward moving parcels at the same level. If upward moving subcloud layer parcels are negatively buoyant, how are they accelerated upward from the sea surface? The answer to this question must lie in the pressure field associated with the convective cells. Under the anelastic approximation this nonhydrostatic pressure field can be computed from a diagnostic equation if the temperature and motion fields are known (e.g. equation (32) of Ogura and Phillips, 1962, or equation (2.4) of Arnason et al., 1968). This pressure field, along with the associated temperature, motion, cloud base and cloud top fields, are shown schematically in Figure 22. Air near the surface is accelerated toward the updraft and upward against negative buoyancy by low pressure in the updraft near cloud base. If one computes the correlation of this pressure pattern with

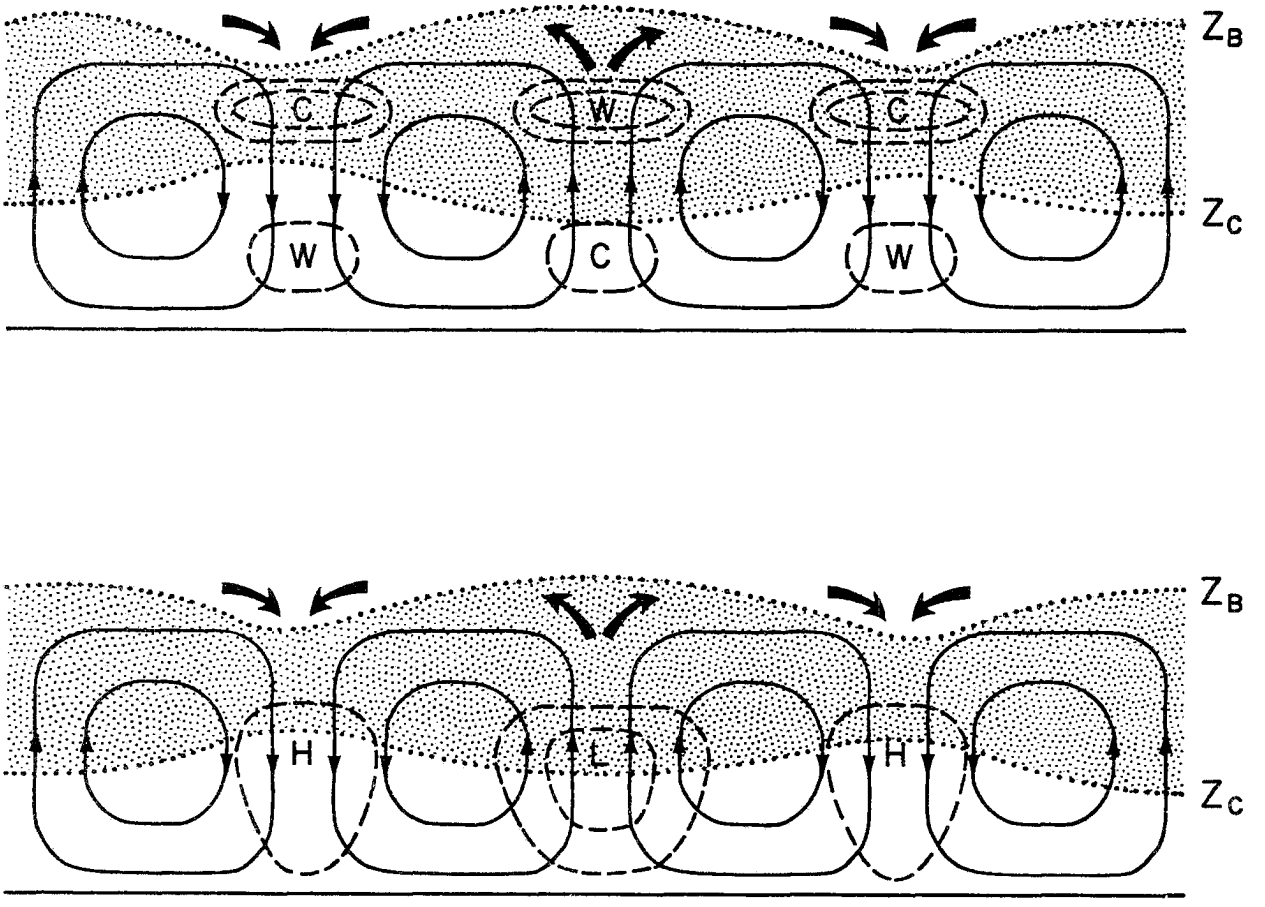

Figure 22. Schematic depiction of the motion field of a convective element along with its associated cloud base, cloud top, temperature (top), and nonhydrostatic pressure (bottom) fields. Note that the updraft has positive buoyancy in the cloud layer and negative buoyancy below. To accelerate surface air upward into the updraft requires the non-hydrostatic pressure shown. Since $\overline{w'p'} < 0$ at cloud base, the cloud layer does work on the subcloud layer.

the convective scale vertical motion field, one finds $(\overline{w'p'})_{z=z_c} < 0$. In other words, the work done on the subcloud layer by the cloud layer maintains the convective motions of the subcloud layer.

The horozontally homogeneous steady state solutions we have just discussed must be applied with caution to real physical situations. This fact will become clear in the next section where we will show that certain aspects (especially cloud top) of the solutions found under steady state horizontally advective situations can be far from their steady state horizontally homogeneous values.

4. Horizontally inhomogeneous solutions

In this section we present results of the numerical integration of the system (2.33) - (2.44) using the procedure described in section 2.3. We are concerned with the variation of the dependent variables (left column of Table 7) under varying externally specified parameters (right column of Table 7), primarily varying sea surface temperature and large-scale divergence. The results presented here can be interpreted either in a Lagrangian sense (i.e. as the downstream modification following a parcel along its trajectory) or in a locally steady state horizontally inhomogeneous sense (i.e. assuming $\frac{\partial}{\partial t} = 0$ and interpreting the substantial derivative $\frac{d}{dt}$ as $V \frac{\partial}{\partial x}$). To facilitate both interpretations we have labeled figures with both distance and time.

Since the system (2.33) - (2.44) contains three first order differential equations, we must specify initial conditions on h_M, $(q+\ell)_M$ and z_B. In all cases we have initialized the model with the relevant steady state horizontally homogeneous solution. The only finite differencing procedure needed to solve (2.33) - (2.44) is a time differencing scheme for (2.42) - (2.44). Because of its accuracy we have chosen to use the classical fourth order Runge-Kutta scheme.

Table 9 outlines the sea surface temperature, wind speed, and large-scale divergence used in the six experiments we shall now discuss. The first four experiments are idealized situations which are based on the eastern North Pacific maps of Neiburger et al. (1961) and Miller and Stevenson (1974). The mean July maps of Neiburger et al. (figures 23-25) show resultant streamlines and isotachs, sea surface temperature, and

TABLE 9. Externally specified parameters for various model experiments. Experiments 1-5 use the mean July Oakland sounding for $h(z_{B+})$, $q(z_{B+})$ and $F_L^{\downarrow}(z_{B+})$. Experiment 6 uses a typical AMTEX sounding. (See figures 10-13).

	Sea Surface Temperature, T_S	Wind Speed, V	Divergence, D
Experiment 1: Movement from cold to warm water with a constant divergence field.	T_S linearly increases from 15°C to 20°C over 1000 km.	7 ms^{-1}	4 x $10^{-6}s^{-1}$
Experiment 2: Movement from warm to cold water with a constant divergence field.	T_S linearly decreases from 16°C to 14°C over 1000 km.	7 ms^{-1}	4 x $10^{-6}s^{-1}$
Experiment 3: Movement from low divergence to high divergence with a constant sea surface temperature field.	15°C	7 ms^{-1}	D linearly increases from 2 x $10^{-6}s^{-1}$ to 6 x $10^{-6}s^{-1}$ over 1000 km.
Experiment 4: Movement from high divergence to low divergence with a constant sea surface temperature field.	15°C	7 ms^{-1}	D linearly decreases from 6 x $10^{-6}s^{-1}$ to 2 x $10^{-6}s^{-1}$ over 1000 km.
Experiment 5: Movement over a discontinuous 2°C increase in sea surface temperature.	T_S changes discontinuously from 14°C to 16°C.	7 ms^{-1}	4 x $10^{-6}s^{-1}$
Experiment 6: Simulation of a wintertime cold air outbreak over the East China Sea, 16 February 1975.	$T_S(x) = T_o + \Delta T \tanh \frac{x-x_o}{d}$	12 ms^{-1}	10.2 x $10^{-6}s^{-1}$

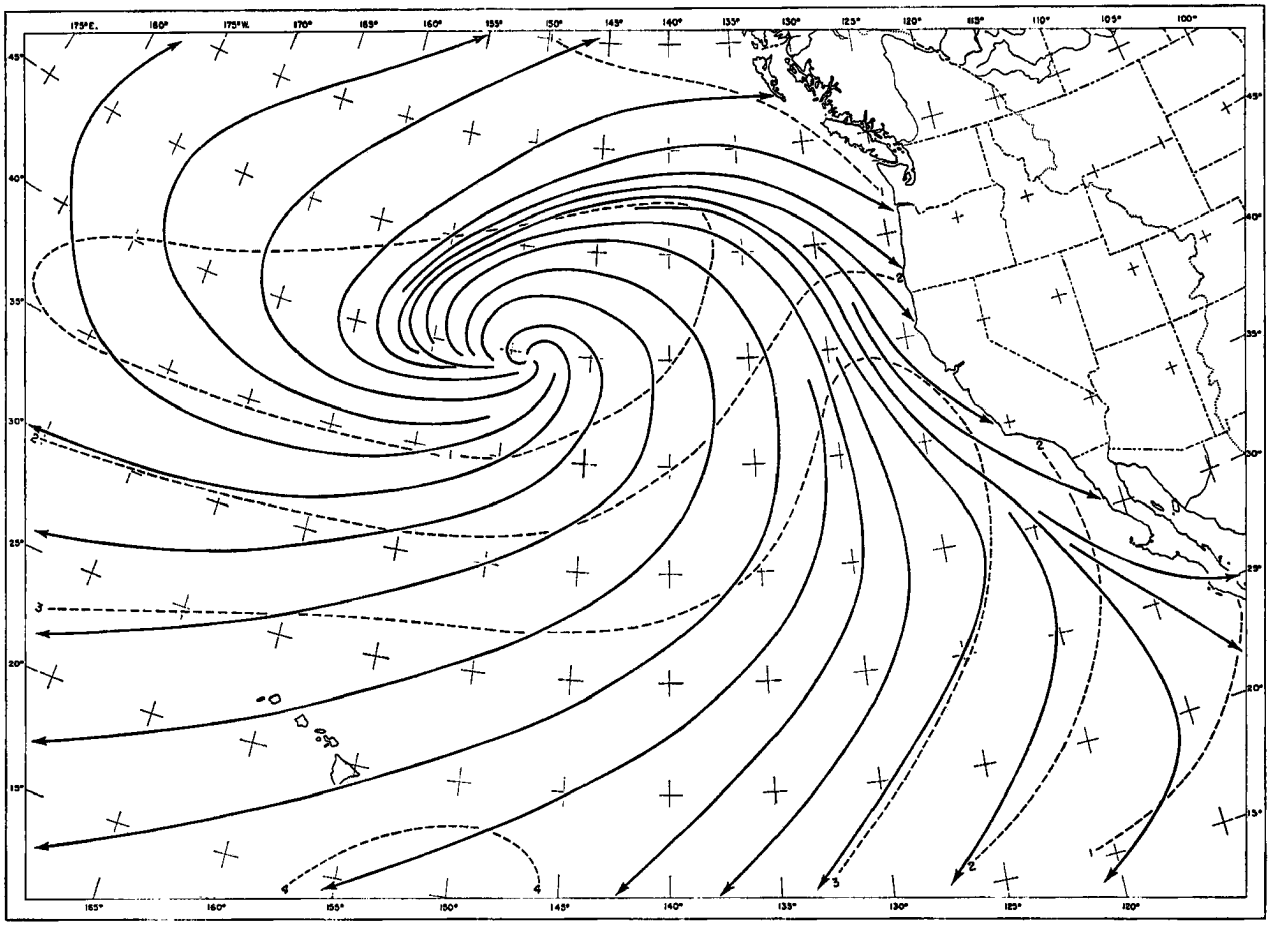

Figure 23. Resultant surface wind streamlines and isotachs for July. After Neiburger et al. (1961).

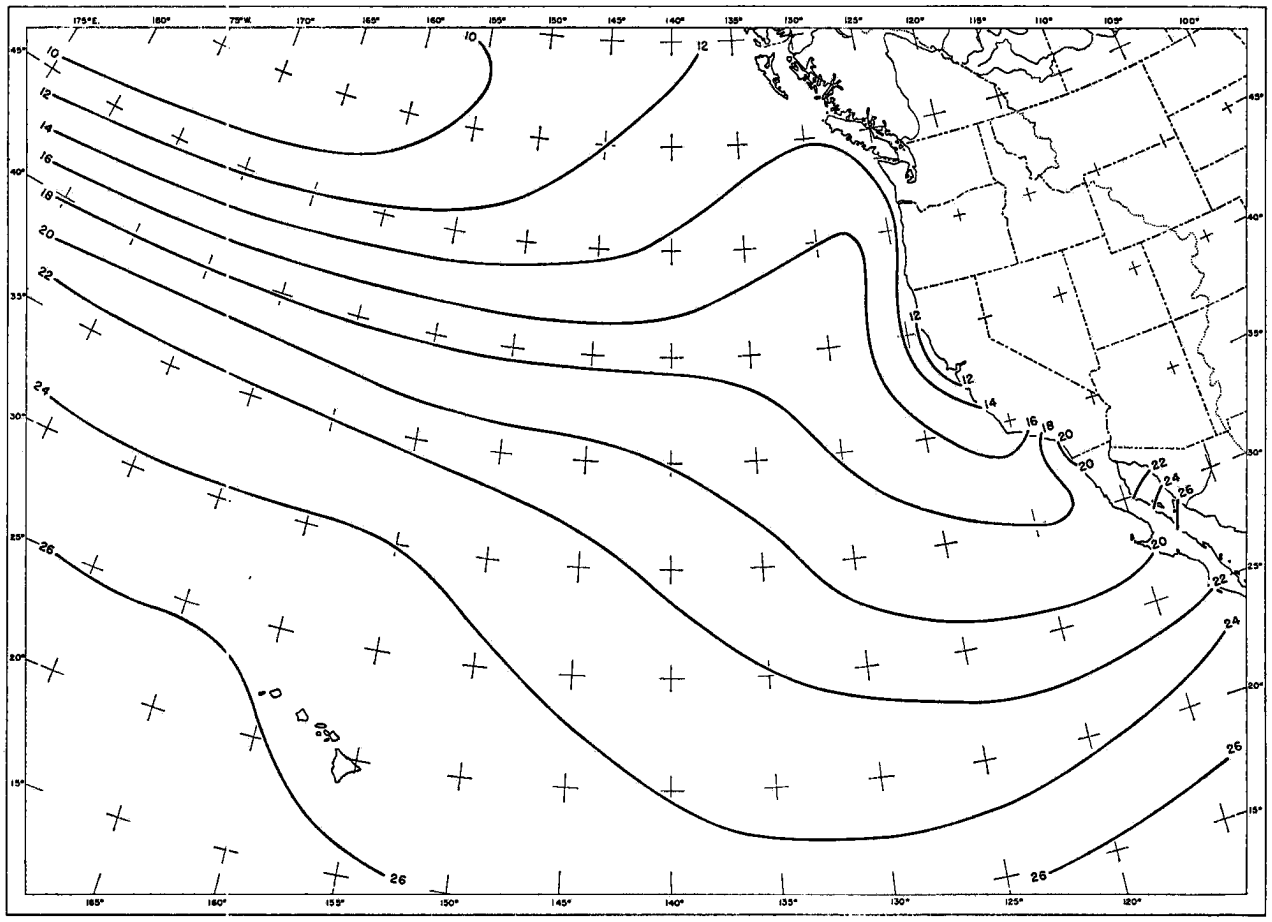

Figure 24. Mean sea surface temperature for July (°C). After Neiburger et al. (1961).

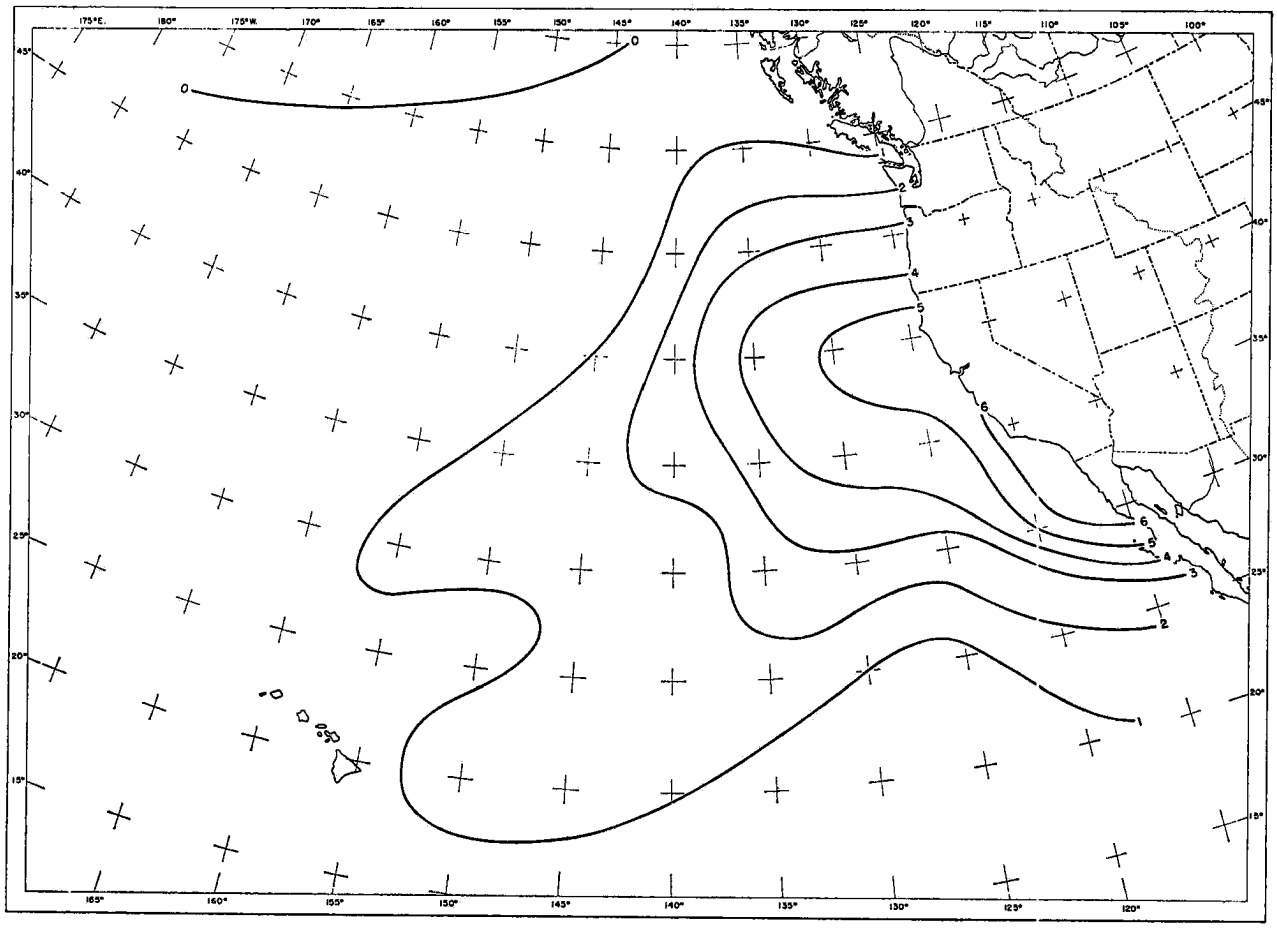

Figure 25. Divergence of resultant surface winds for July ($10^{-6}s^{-1}$). After Neiburger et al. (1961).

large-scale divergence. One deficiency of figure 23 is that it displays resultant wind speed, i.e. the speed of the vector averaged wind. What should probably be used for V in the model is the average wind speed. Miller and Stevenson's diagram of mean July 1961-74 surface pressure, resultant wind direction, resultant wind speed and average wind speed is shown in figure 26. Note the large differences between resultant wind speed and average wind speed. These maps indicate that there is a large region southwest of San Francisco where marine layer air passes from cold to warm sea surface temperature and from high to low divergence. The maps also indicate that there is a region northwest of San Francisco where the air passes from warm to cold sea surface temperature and from low to high divergence. Experiments 1-4 have been designed to isolate the influence of varying sea surface temperature and varying divergence in these two regions. Thus, we have used the mean July Oakland sounding (figures 12 and 13) for $h(z_B+)$, $q(z_B+)$, and $F_L^{\downarrow}(z_B+)$ in Experiments 1-4.

Experiment 5 is an attempt to illustrate the different adjustment time for h_M and $(q+\ell)_M$ as opposed to that for z_B. In Experiment 5 we have again used the mean Oakland sounding for $h(z_B+)$, $q(z_B+)$, and $F_L^{\downarrow}(z_B+)$.

Experiment 6 is an attempt to simulate the rapid changes which occur in a cold air outbreak over the Kuroshio Current. Our sea surface temperature pattern takes the form

$$T_S(x) = T_o + \Delta T \tanh \frac{x-x_o}{d}, \qquad (4.1)$$

where we have chosen T_o as 14°C, ΔT as 7°C, x_o as 500 km, and d as 70 km. Equatior (4.1) is an attempt to fit the mean February sea surface temperature

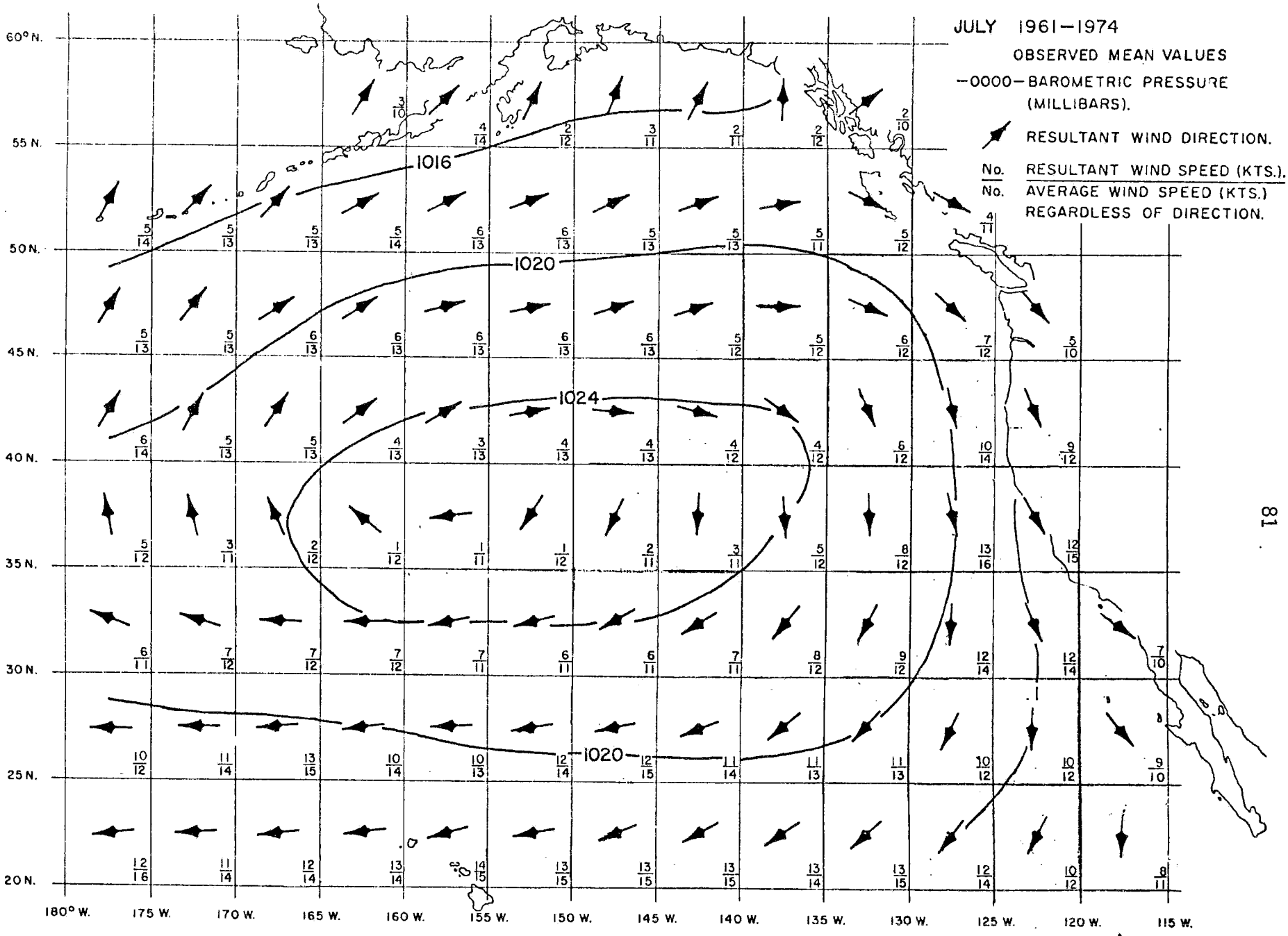

Figure 26. Mean July (1961-74) surface pressure, resultant wind direction, resultant wind speed (numerator), and average wind speed (denominator). After Miller and Stevenson (1974).

pattern, assuming approximately northwesterly surface flow. The mean February pattern (reproduced from Lenschow, 1972), along with the surface winds for 00Z-06Z 16 February 1975, was shown in figures 10b and 10c. The divergence, surface wind speed, and profiles of $h(z_B+)$, $q(z_B+)$ and $F_L^{\downarrow}(z_B+)$ shown in figures 12 and 13 are taken from the 00Z and 06Z AMTEX soundings for 16 February 1975 (see Management Committee for AMTEX, 1976). A DMSP satellite image for 0255Z 16 February 1975 was shown in figure 10a.

Let us now discuss the results of these six experiments.

4.1 Influence of varying sea surface temperatures

The first two experiments are designed to illustrate mixed layer behavior under conditions of constant wind speed (7 ms^{-1}), constant divergence (4 x $10^{-6}s^{-1}$), and varying sea surface temperature. In Experiment 1 (figure 27) air moves along a trajectory toward warmer water, with the sea surface temperature gradient being 5°C/1000 km. In Experiment 2 (figure 28) air moves toward colder water, with the sea surface temperature gradient being -2°C/1000 km.

The results of Experiment 1 show that advection over warmer water produces increases in z_B, h_M, $(q+\ell)_M$, and the fluxes of h and $q+\ell$. In addition, the increase in h_M and $(q+\ell)_M$ is such that the subcloud layer is warmed enough for z_C to rise, even though the marine layer is moistening. The cold advection very quickly produces a positive $(\overline{w's_v'})_S$. After 500 km about 50% of the buoyant production of turbulence kinetic energy (figure 27f) is coming from the subcloud layer, while after 1000 km about 60% is coming from the subcloud layer. Some of the

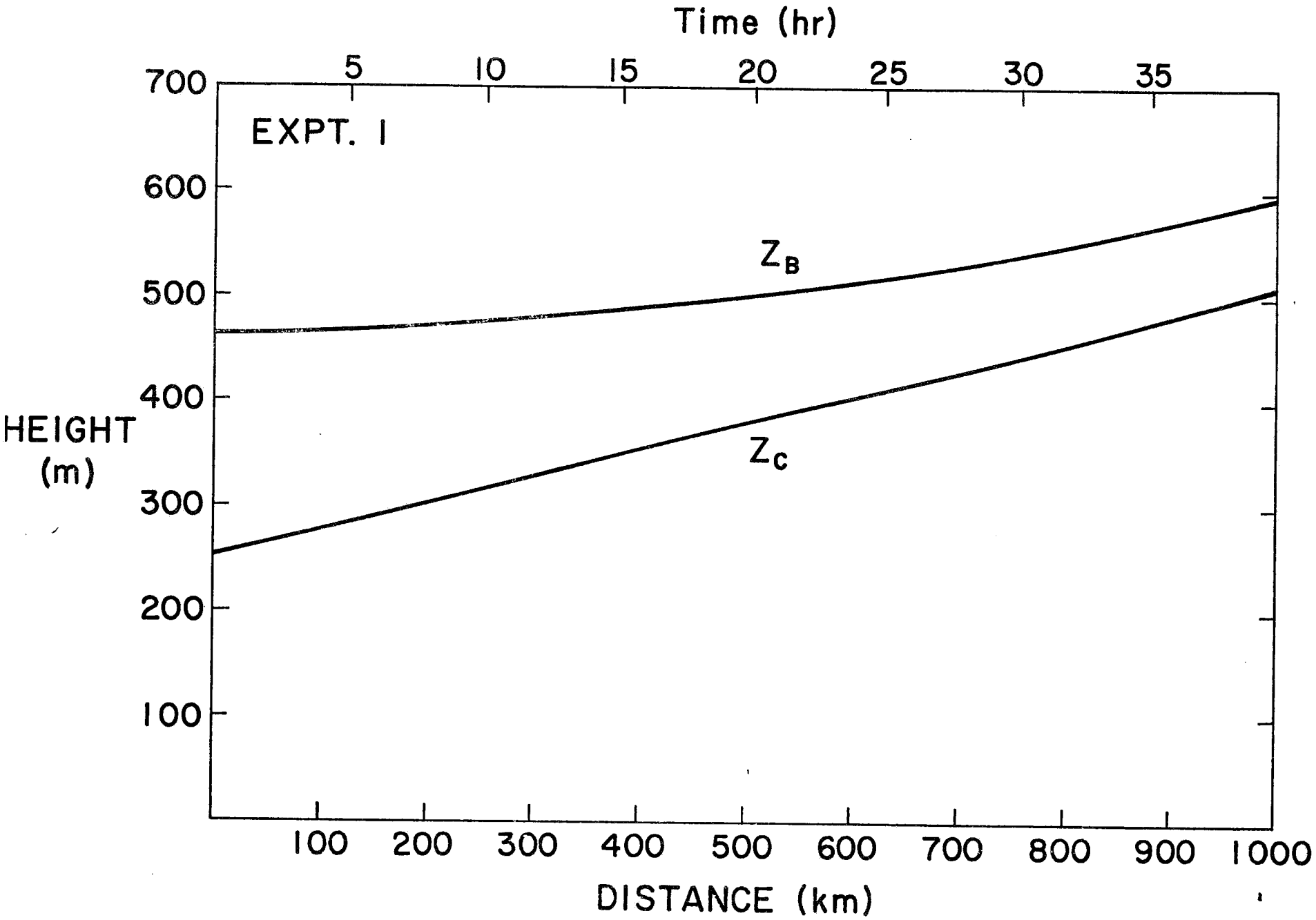

Figure 27a. Results for Experiment 1 (constant divergence, increasing sea surface temperature).

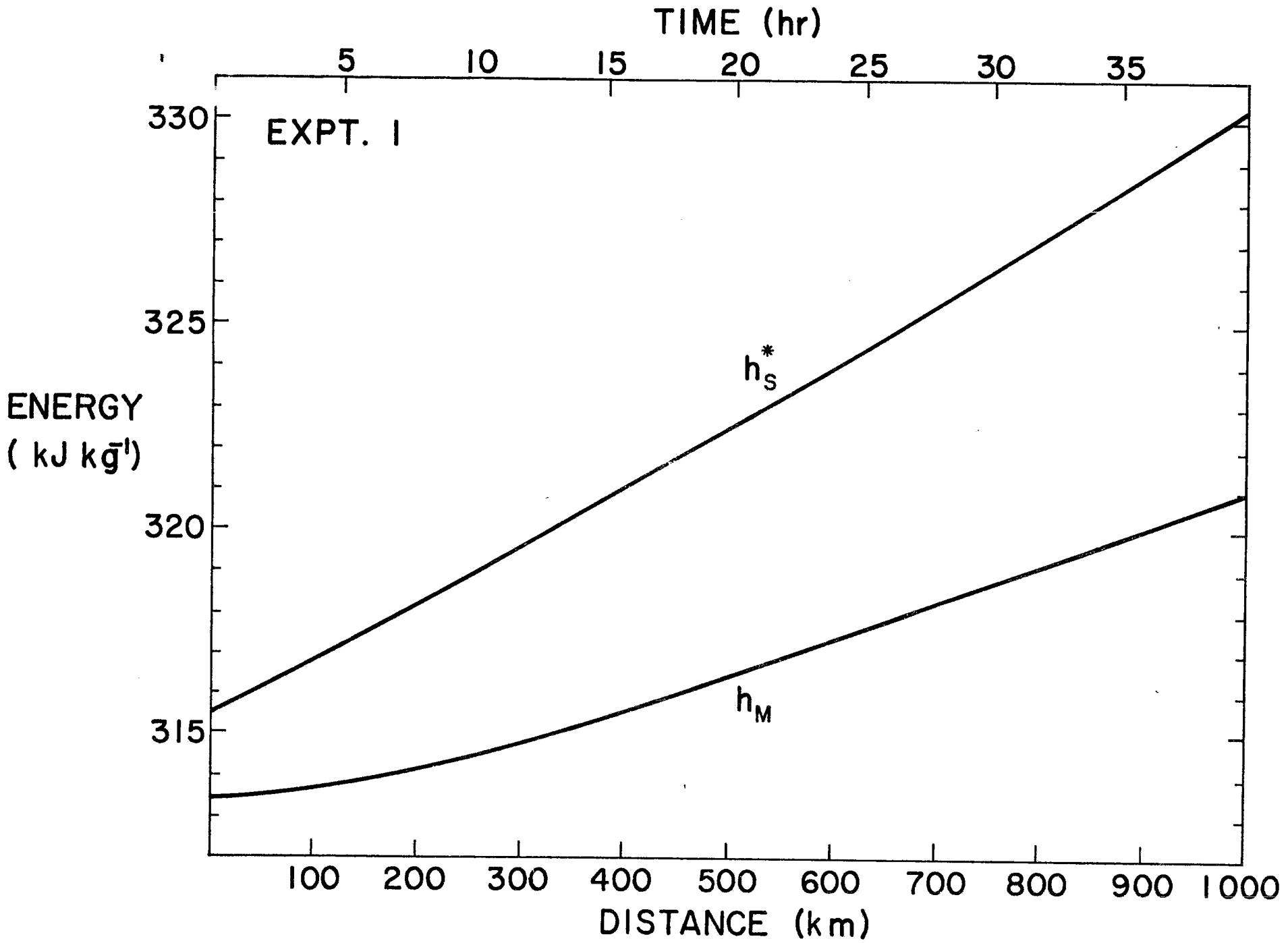

Figure 27b. Results for Experiment 1 (constant divergence, increasing sea surface temperature).

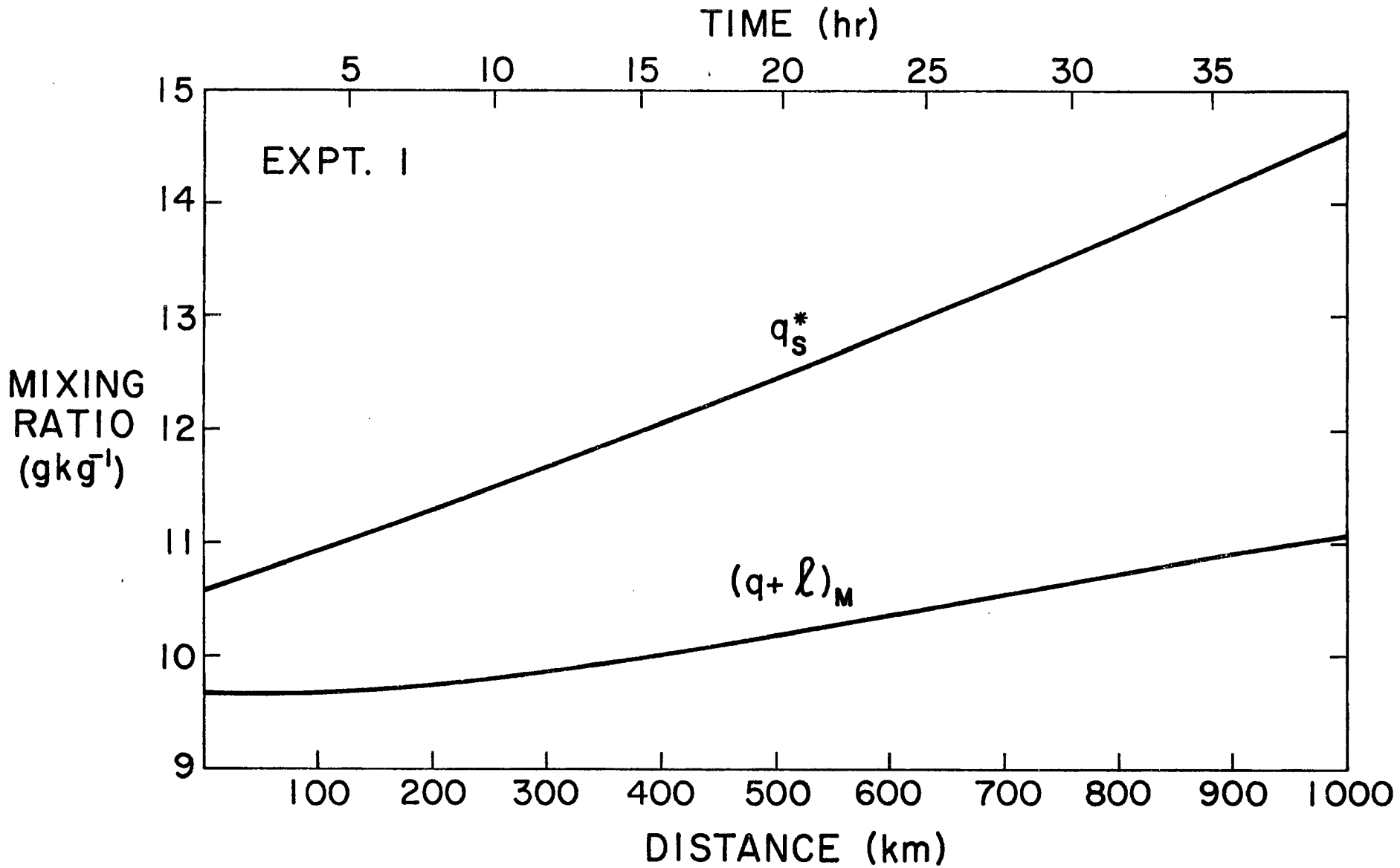

Figure 27c. Results for Experiment 1 (constant divergence, increasing sea surface temperature).

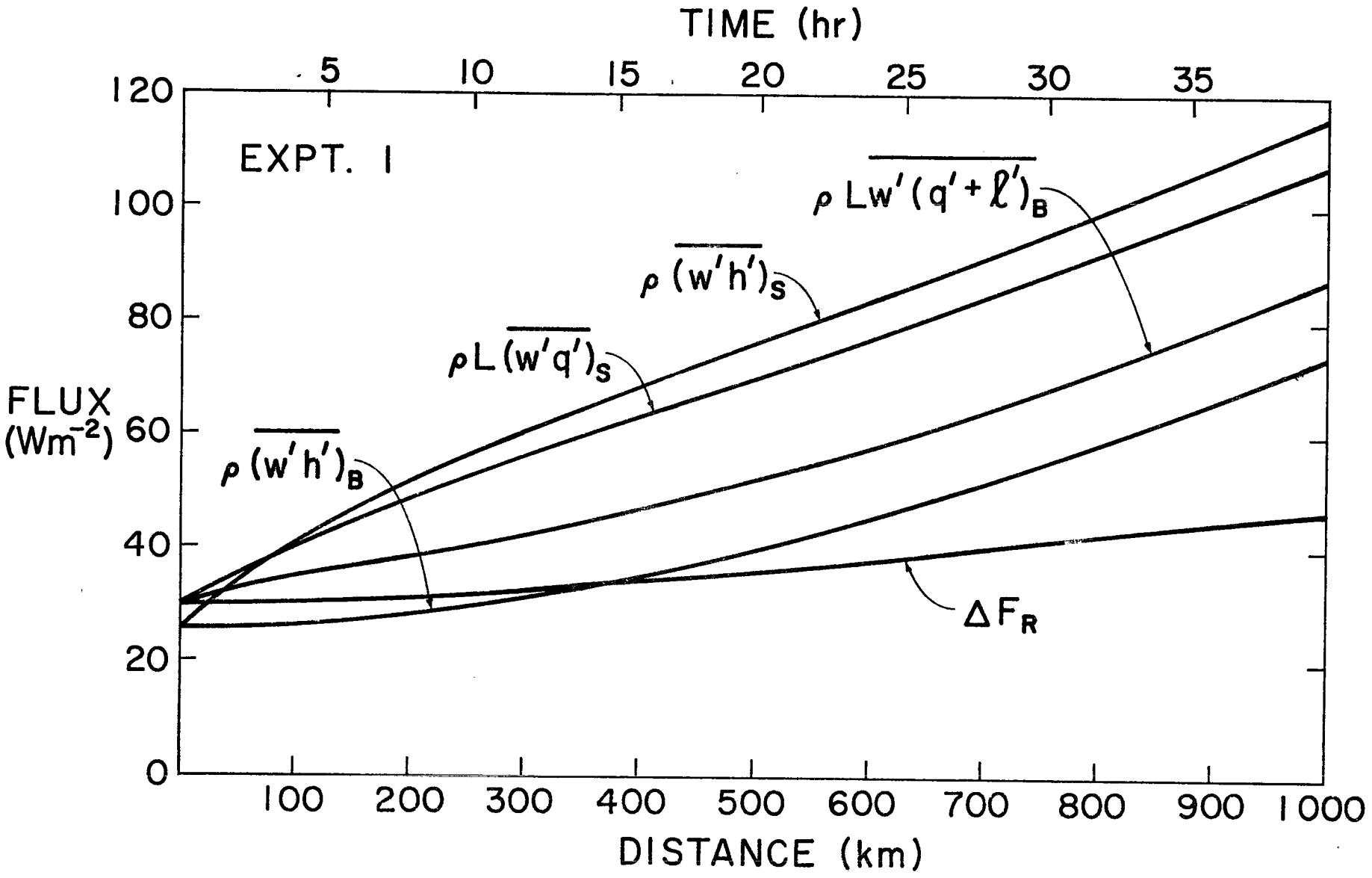

Figure 27d. Results for Experiment 1 (constant divergence, increasing sea surface temperature).

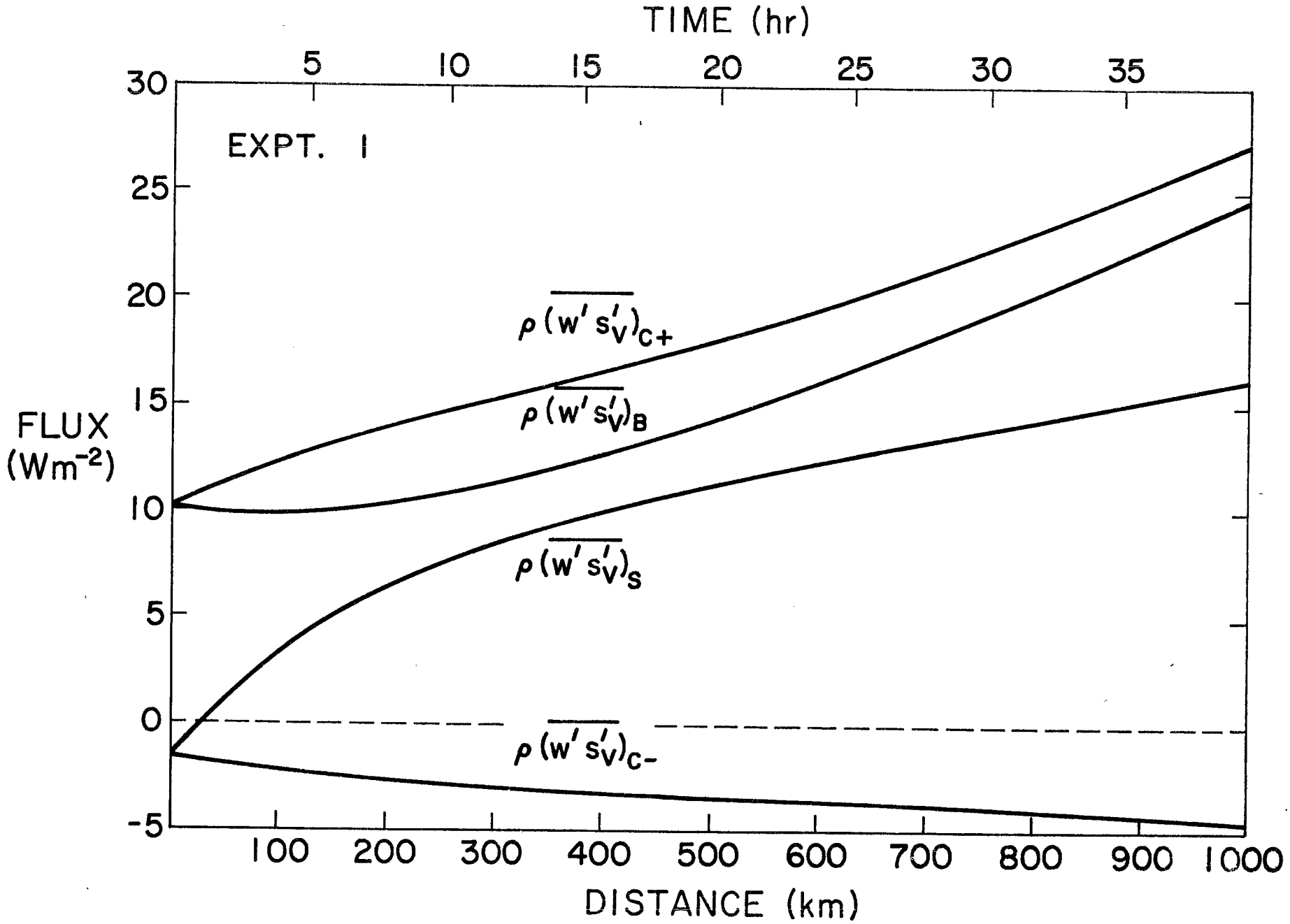

Figure 27e. Results for Experiment 1 (constant divergence, increasing sea surface temperature).

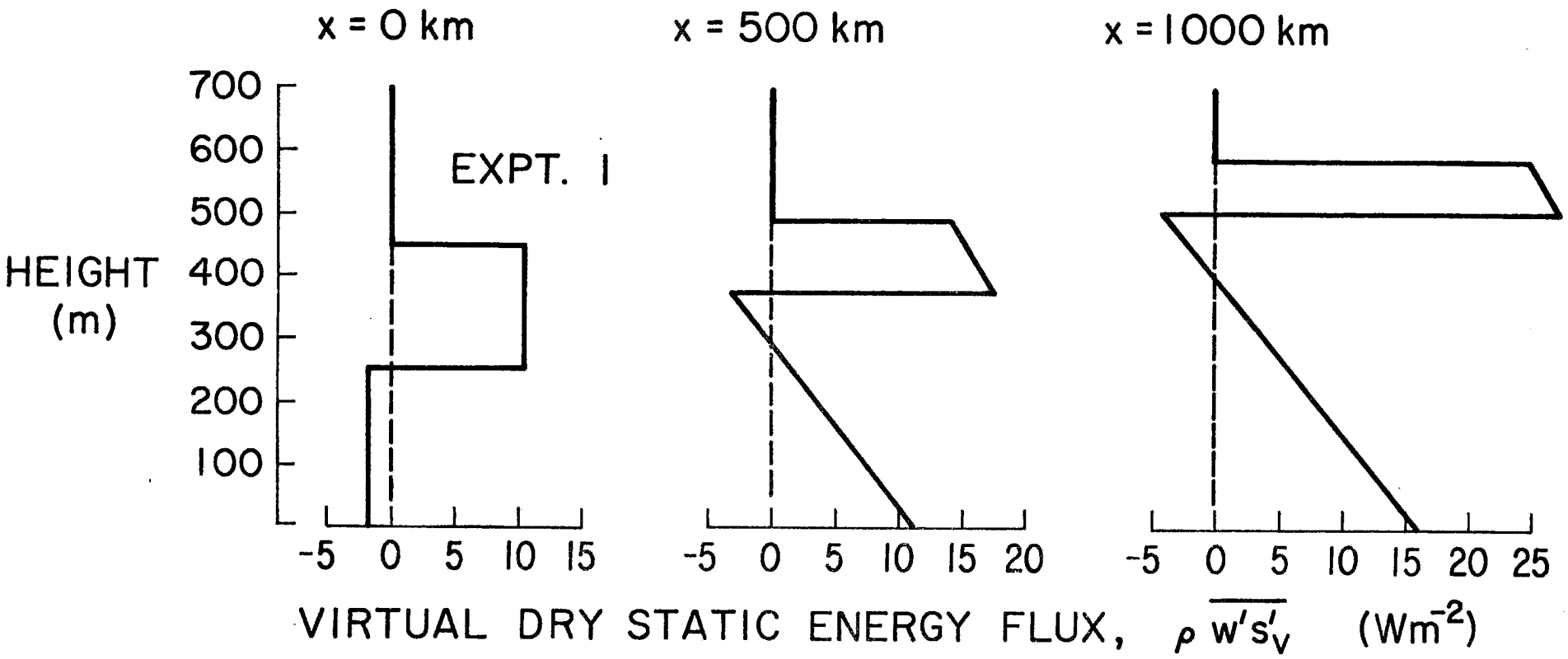

Figure 27f. Results for Experiment 1 (constant divergence, increasing sea surface temperature).

differences between Experiment 1 at 600 km or about 24 hr and the steady state horizontally homogeneous solutions of the last section are shown in Table 10. As might be expected, in this cold advection situation the cloud top and cloud base tend to be lower, h_M and $(q+\ell)_M$ tend to be smaller, and the surface fluxes tend to be larger. But perhaps most interesting is the large difference in cloud top heights. The cloud top after 600 km is only 515 m, which is considerably lower than the steady state horizontally homogeneous value of 872 m. We shall later attempt to explain this in terms of the slow adjustment time for z_B.

TABLE 10. Comparison of the steady state horizontally inhomogeneous solution after 600 km (i.e. where T_S is 18°C) of Experiment 1 with the steady state horizontally homogeneous solution.

	Horizontally Inhomogeneous	Horizontally Homogeneous
z_B (m)	515	872
z_C (m)	405	511
h_M ($kJkg^{-1}$)	317.38	319.14
$(q+\ell)_M$ (gkg^{-1})	10.37	10.59
$\rho(\overline{w'h'})_S$ (Wm^{-2})	83	60
$\rho L(\overline{w'q'})_S$ (Wm^{-2})	76	69

The results of Experiment 2 show that advection over colder water causes z_B, z_C, h_M, $(q+\ell)_M$, and the fluxes of h and $q+\ell$ to decrease. The descent of cloud base indicates a tendency to produce a fog at the

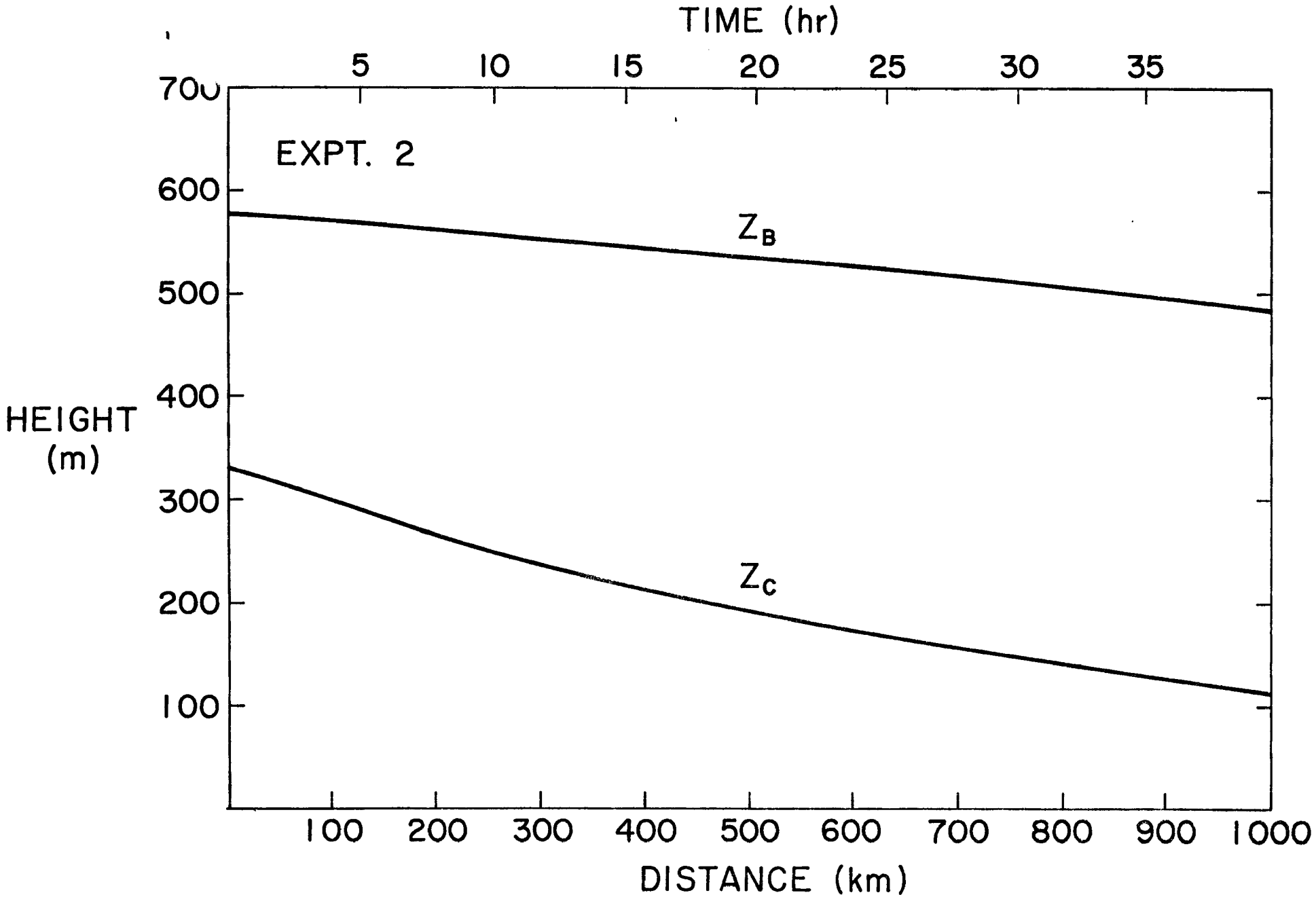

Figure 28a. Results for Experiment 2 (constant divergence, decreasing sea surface temperature).

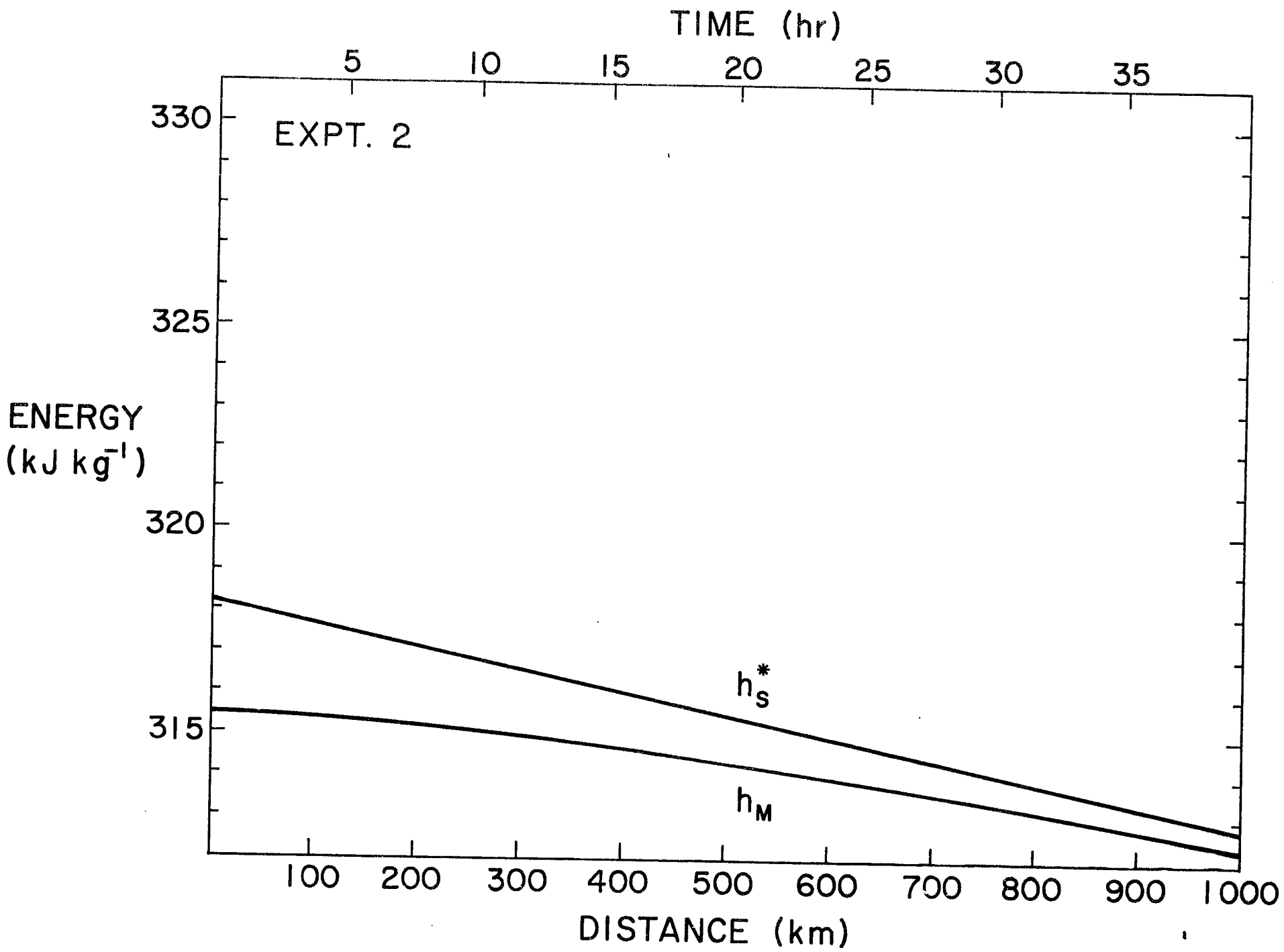

Figure 28b. Results for Experiment 2 (constant divergence, decreasing sea surface temperature).

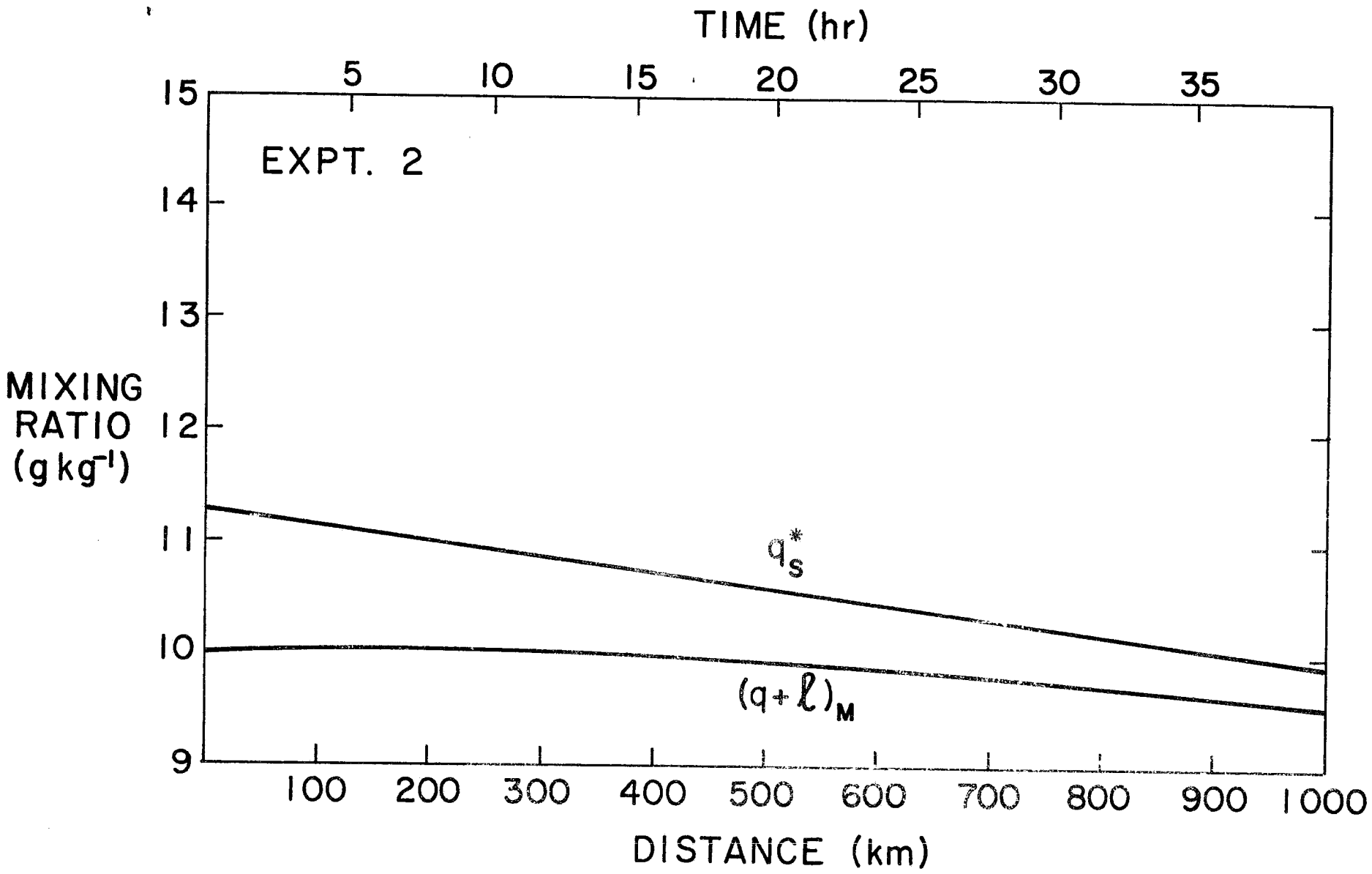

Figure 28c. Results for Experiment 2 (constant divergence, decreasing sea surface temperature).

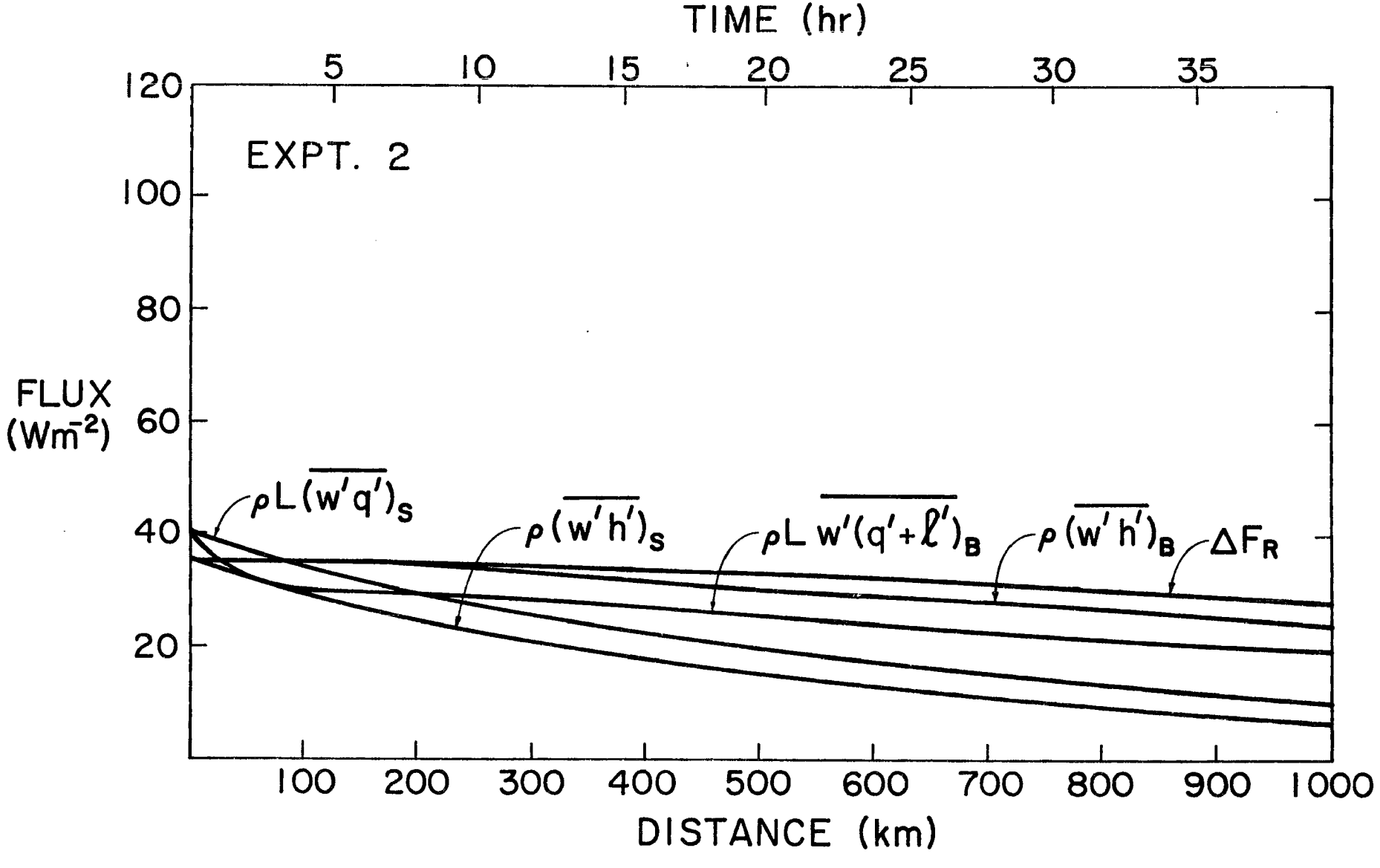

Figure 28d. Results for Experiment 2 (constant divergence, decreasing sea surface temperature).

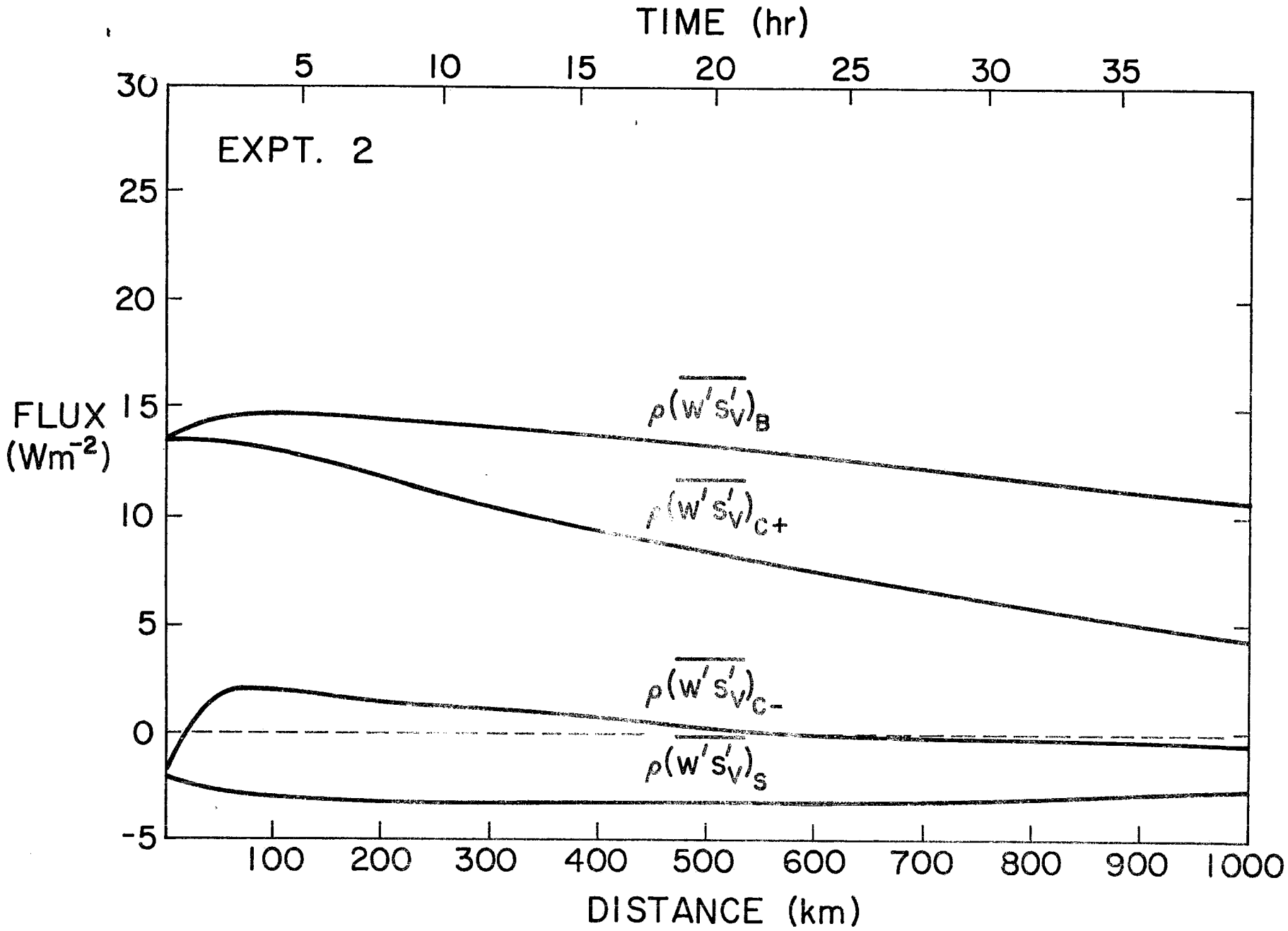

Figure 28e. Results for Experiment 2 (constant divergence, decreasing sea surface temperature).

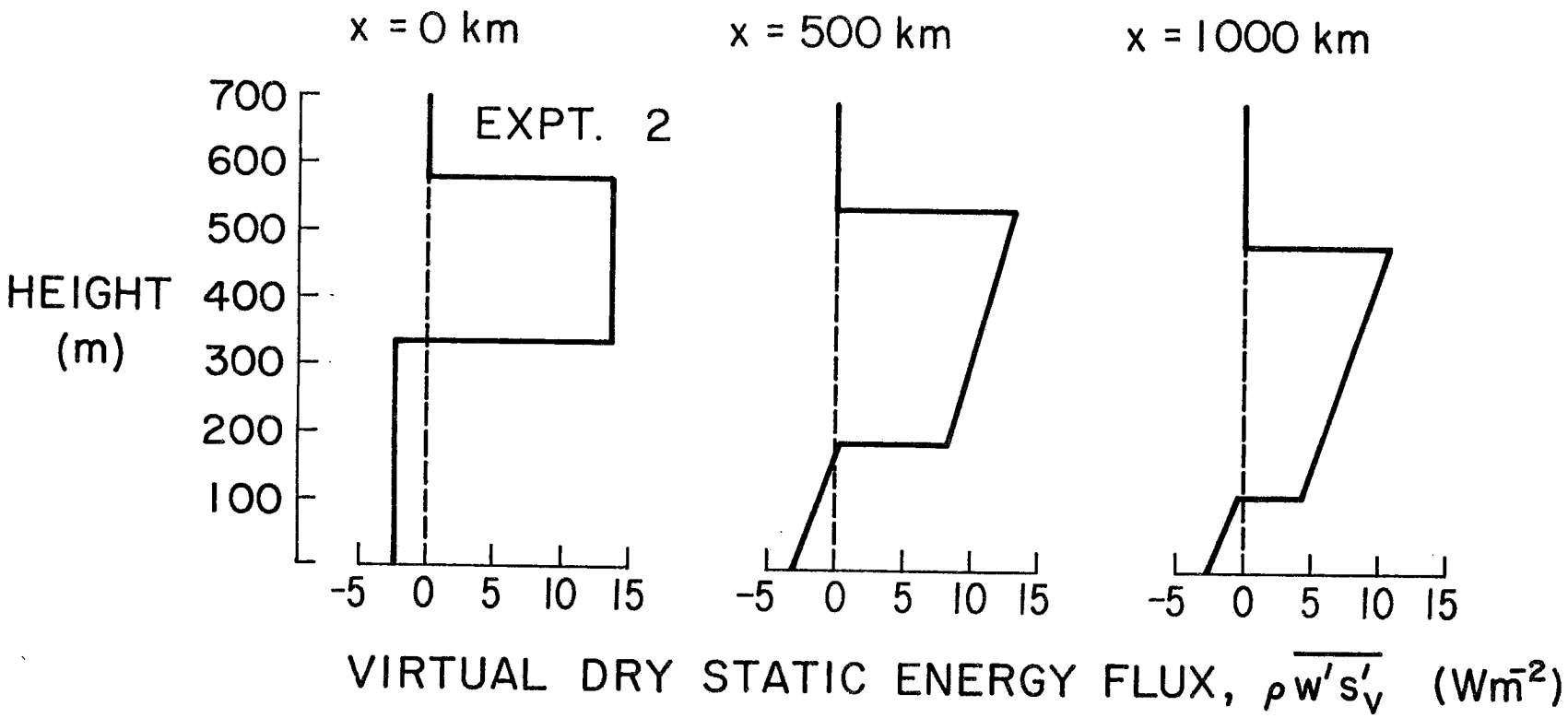

Figure 28f. Results for Experiment 2 (constant divergence, decreasing sea surface temperature).

surface. In two other experiments (not shown) in which we changed the sea surface temperature gradient from -2°C/1000 km to -3°C/1000 km and -4°C/1000 km (leaving the initial conditions unchanged) cloud base descended to the surface in 990 km and 570 km respectively. Figures 23 and 24 indicate that northwest of San Francisco summertime cold advective situations stronger than -4°C/1000 km are quite common. Thus, the northern California and southern Oregon coasts must be regions of frequent summertime fog. That this is indeed the case is illustrated in Table 11, which shows the average number of days per month with visibility less than a half mile for coastal Oregon and California stations. The table was constructed using data from U. S. Naval Weather Service (1969). The most interesting feature of the table is the summertime high incidence of low visibility in northern California as opposed to the low incidence in southern California.

4.2 Influence of varying large-scale divergence

Experiments 3 and 4 are designed to illustrate mixed layer behavior under conditions of constant wind speed (7 ms^{-1}), constant sea surface temperature (15°C), and varying large-scale divergence. In Experiment 3 (figure 29) air moves toward higher divergence, with the gradient being $4 \times 10^{-6} s^{-1}$/1000 km. In Experiment 4 (figure 30) air moves toward lower divergence with the gradient being $-4 \times 10^{-6} s^{-1}$/1000 km.

The most apparent general feature of figures 29 and 30 is that there is practically no variation of any model variable except z_B. Although it may at first sight seem surprising, this feature is consistent with figures 14-18, which show that in the steady state horizontally

TABLE 11. The average number of days in the specified month on which there was at least one observation of visibility less than 0.5 mile. Except for the omission of San Francisco[1], the stations along the Oregon and California coasts listed here are the same as those listed in Table 2.

Station	Per. of Rec.	Latitude	Longitude	Elev.	Jan	Feb	Mar	Apr	May	Jun	Jul	Aug	Sep	Oct	Nov	Dec	Year
Astoria, Oregon	12 years	46.2°N	123.9°W	3 m	4.2	2.6	1.4	2.0	1.3	1.1	1.1	4.1	5.2	6.1	3.3	5.4	37.8
North Bend, Oregon	12 years	43.4°N	124.2°W	4 m	3.0	4.3	3.1	3.9	3.7	4.1	5.7	10.7	12.6	11.7	7.1	5.9	75.8
Crescent City, California	6 years	41.8°N	124.2°W	17 m	2.4	2.6	2.0	3.6	5.4	5.8	10.0	15.3	12.8	11.9	6.0	1.8	79.6
Eureka, California	12 years	40.8°N	124.1°W	2 m	2.7	3.4	2.1	4.3	4.2	6.4	12.5	13.2	13.0	12.7	9.5	5.5	89.5
Monterey Peninsula, California	12 years	36.6°N	121.9°W	68 m	2.8	2.8	2.0	2.3	1.8	2.8	6.4	7.3	6.6	8.1	4.0	2.6	49.5
Los Angeles Int'l Airport, California	12 years	33.9°N	118.4°W	39 m	4.4	4.0	4.7	3.1	1.4	1.6	1.8	2.6	4.7	5.3	6.1	6.5	46.2
San Diego Int'l Airport, California	12 years	32.7°N	117.2°W	5 m	4.0	3.4	3.0	2.2	0.5	1.0	1.2	0.8	4.1	4.4	5.5	6.1	36.2

[1]The San Francisco area has been omitted because the available stations are not well exposed to open ocean conditions.

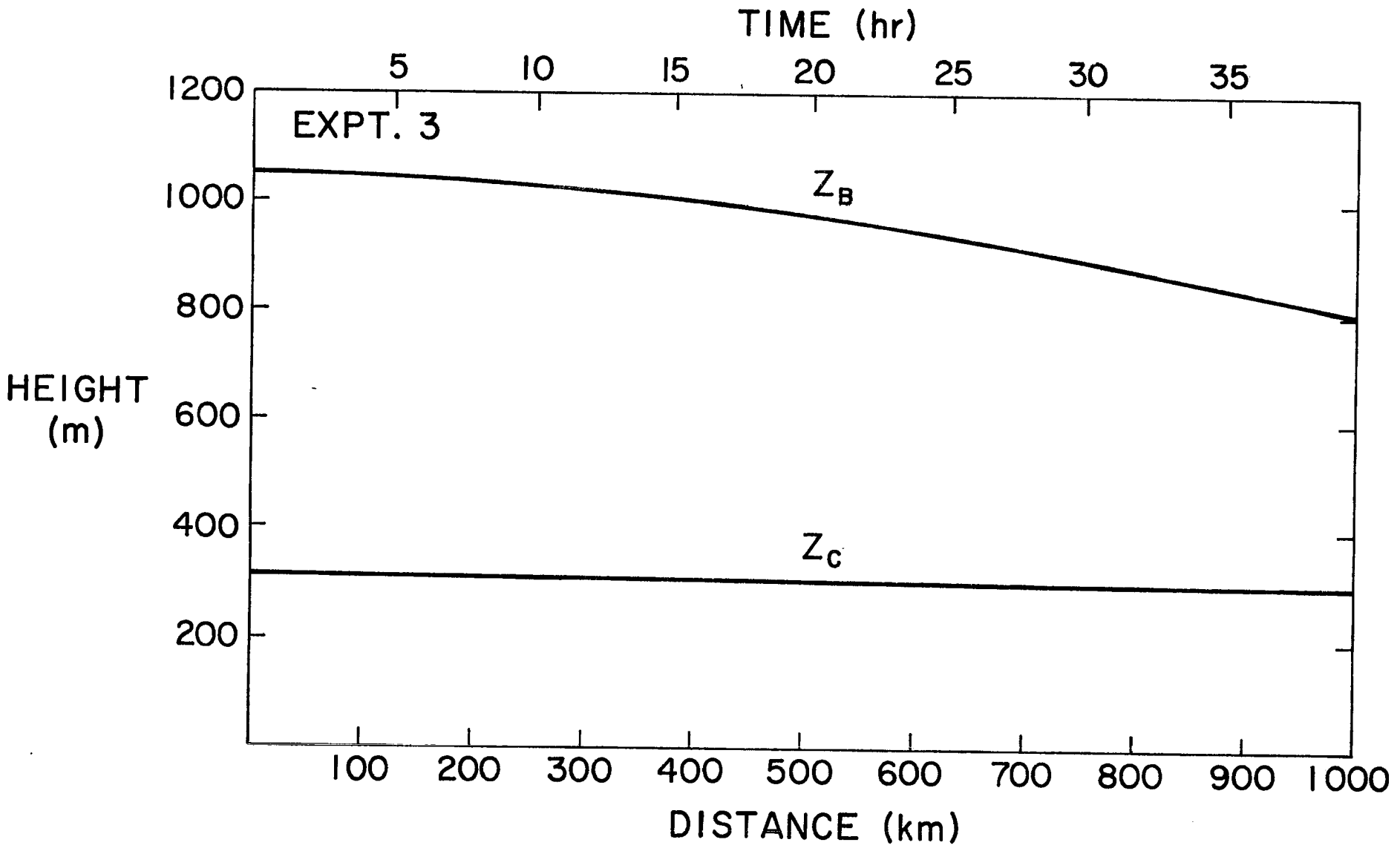

Figure 29a. Results for Experiment 3 (increasing divergence, constant sea surface temperature).

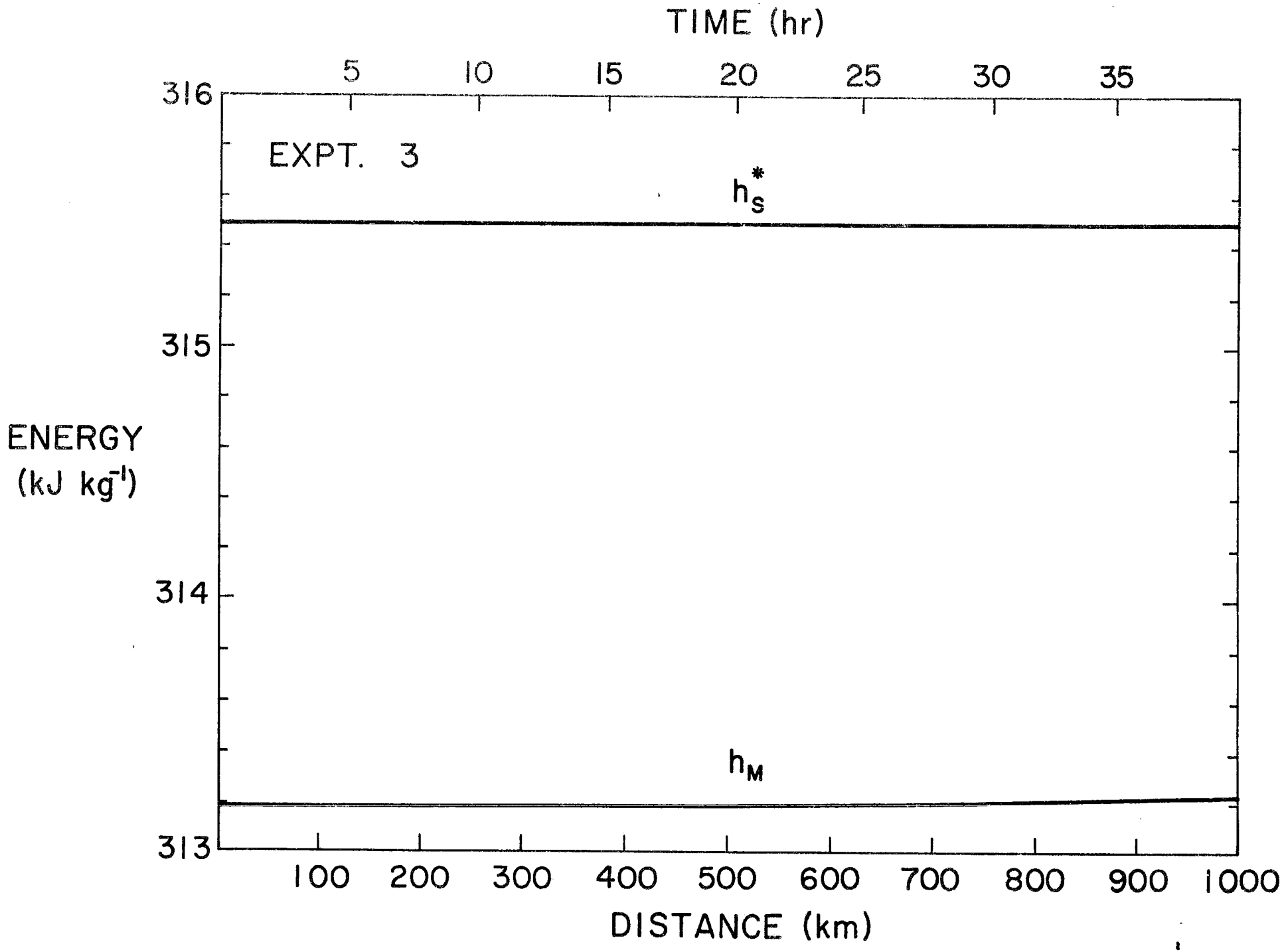

Figure 29b. Results for Experiment 3 (increasing divergence, constant sea surface temperature).

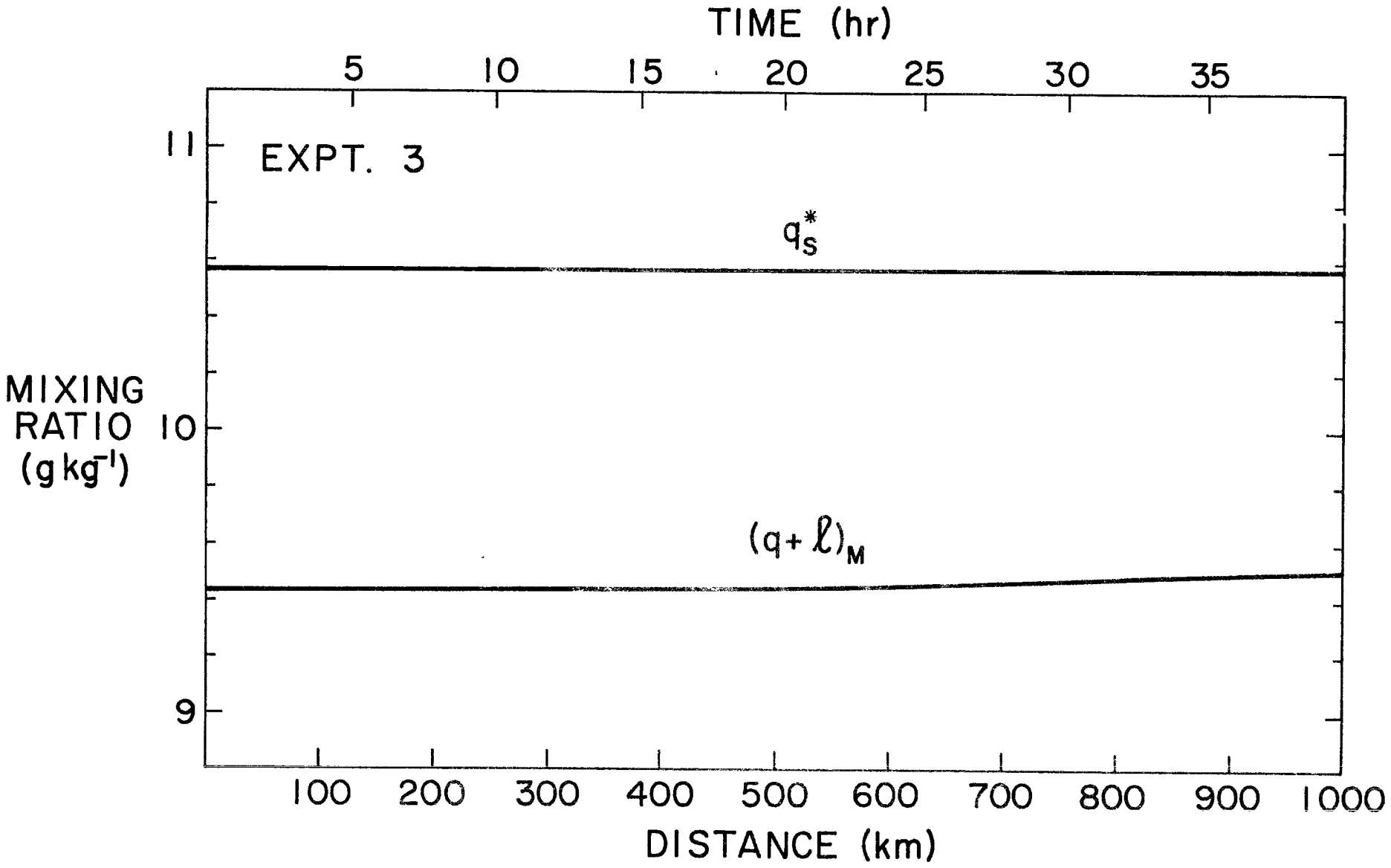

Figure 29c. Results for Experiment 3 (increasing divergence, constant sea surface temperature).

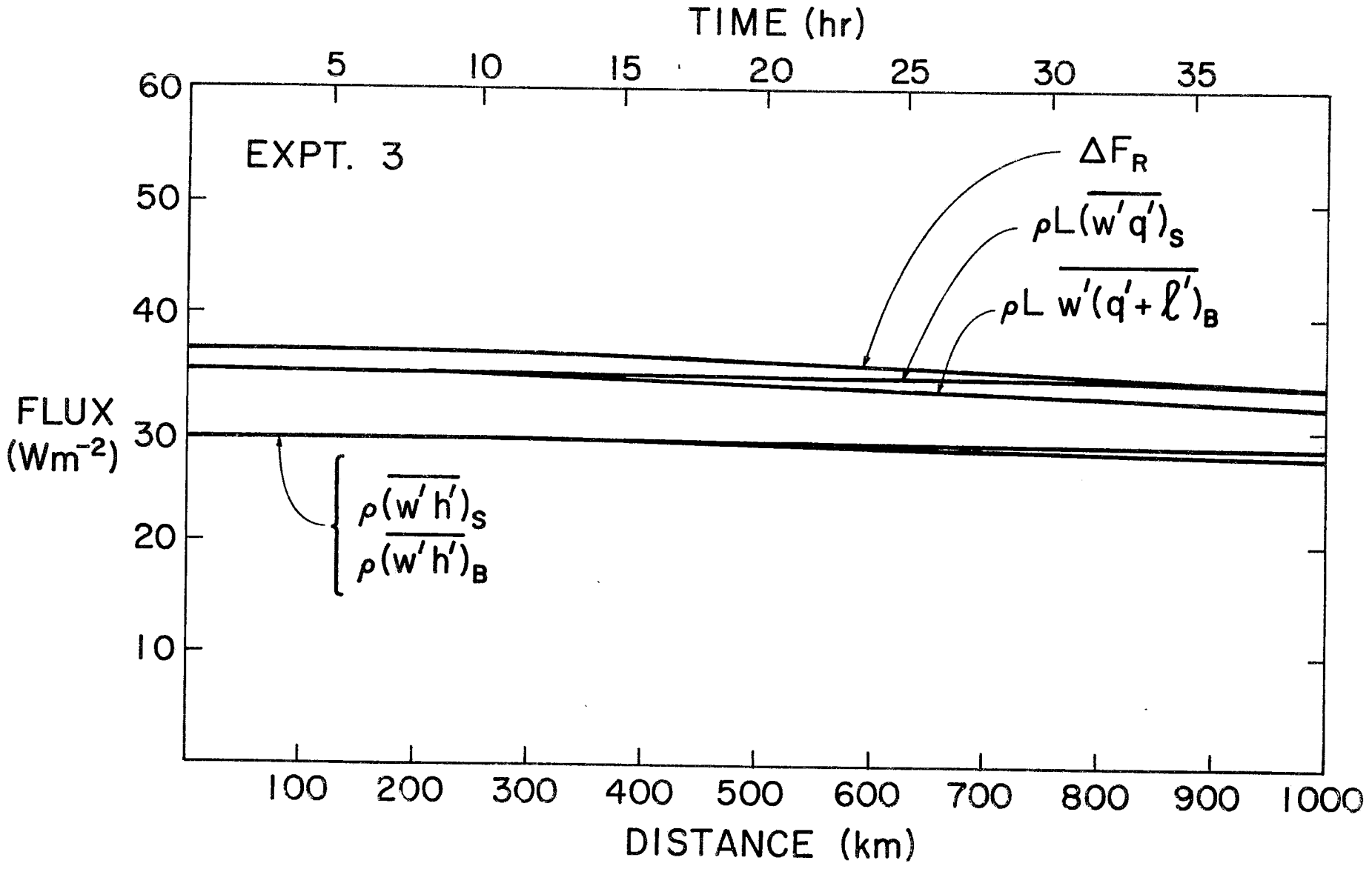

Figure 29d. Results for Experiment 3 (increasing divergence, constant sea surface temperature).

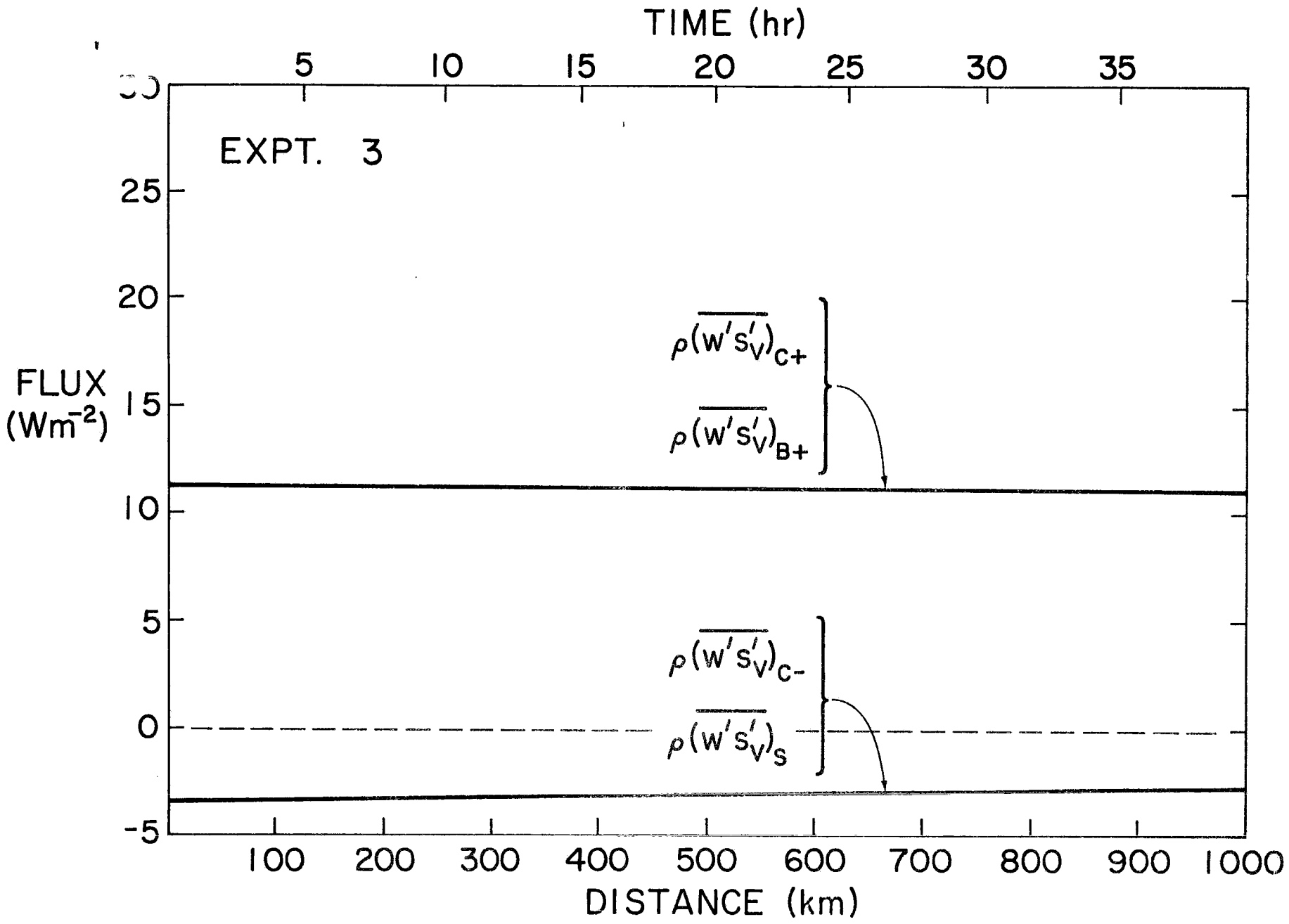

Experiment 29e. Results for Experiment 3 (increasing divergence, constant sea surface temperature).

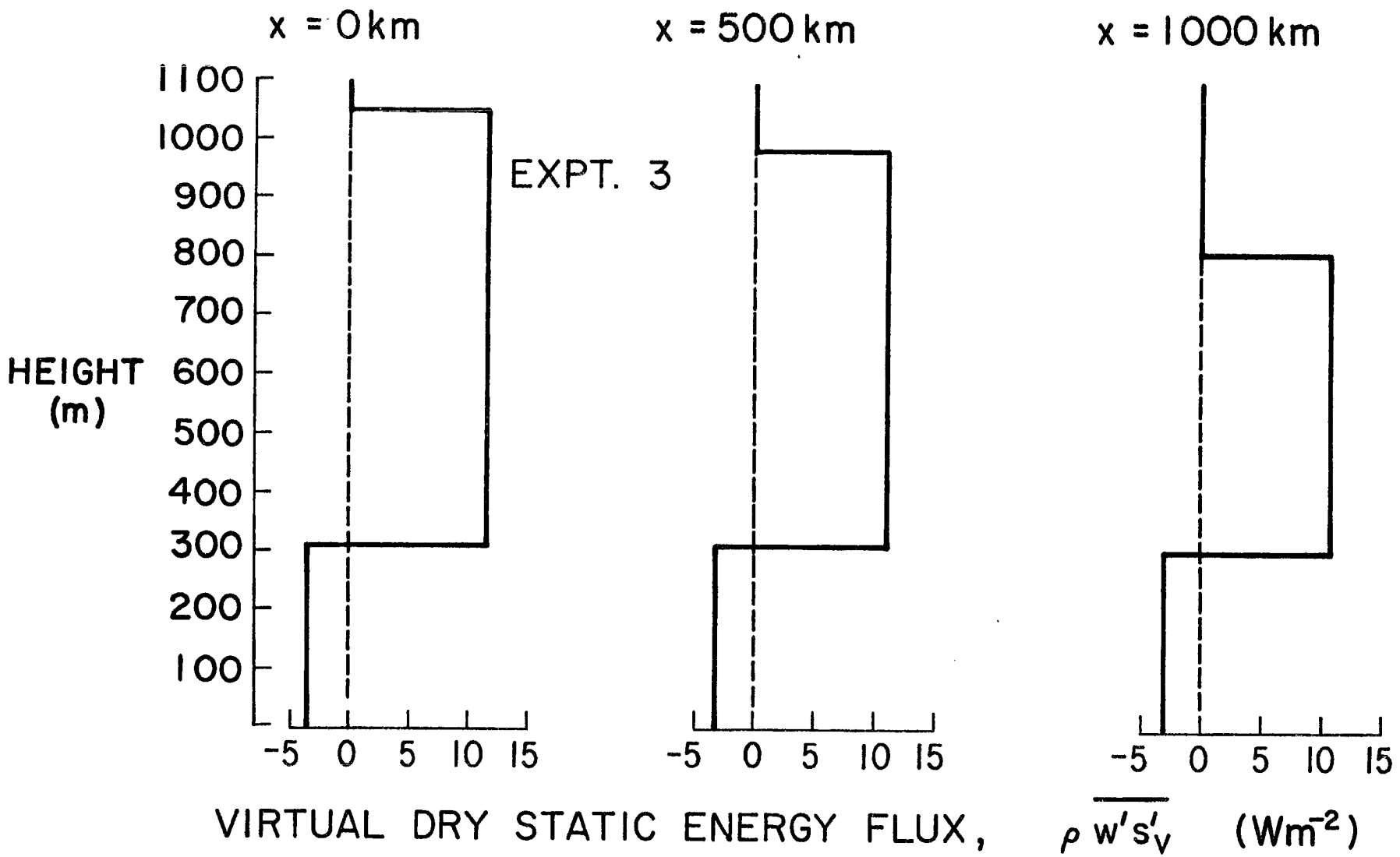

Figure 29f. Results for Experiment 3 (increasing divergence, constant sea surface temperature).

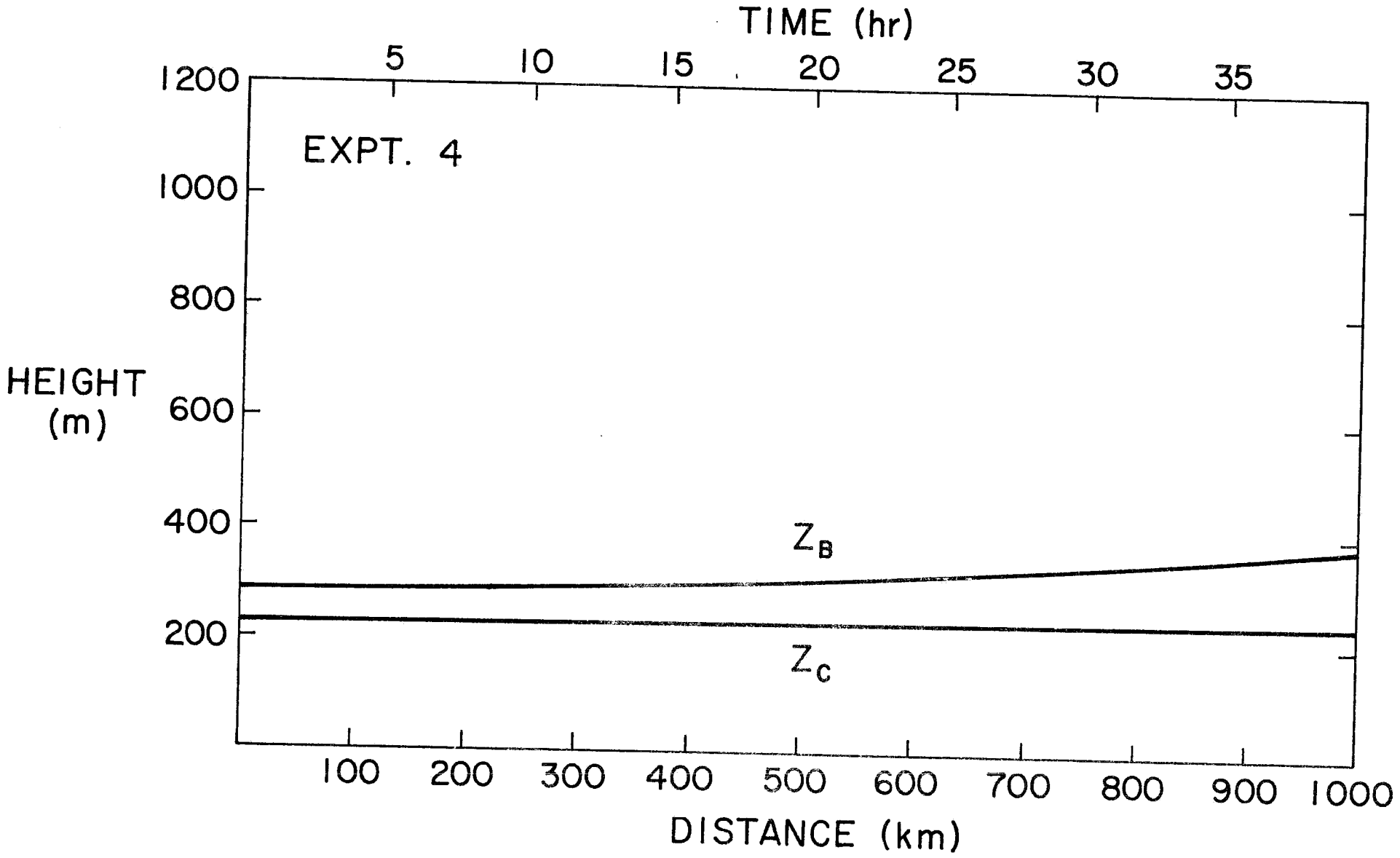

Figure 30a. Results for Experiment 4 (decreasing divergence, constant sea surface temperature).

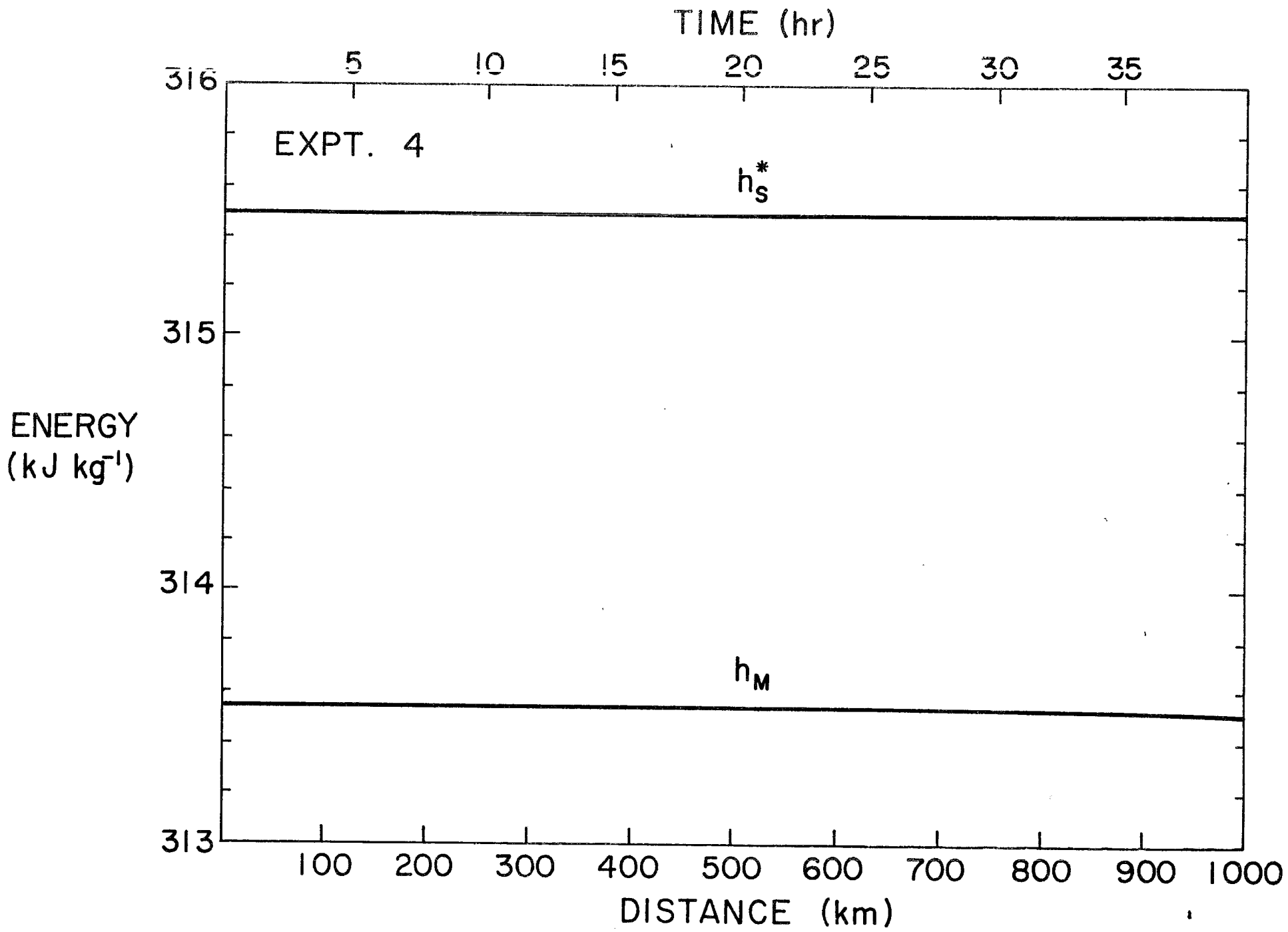

Figure 30b. Results for Experiment 4 (decreasing divergence, constant sea surface temperature).

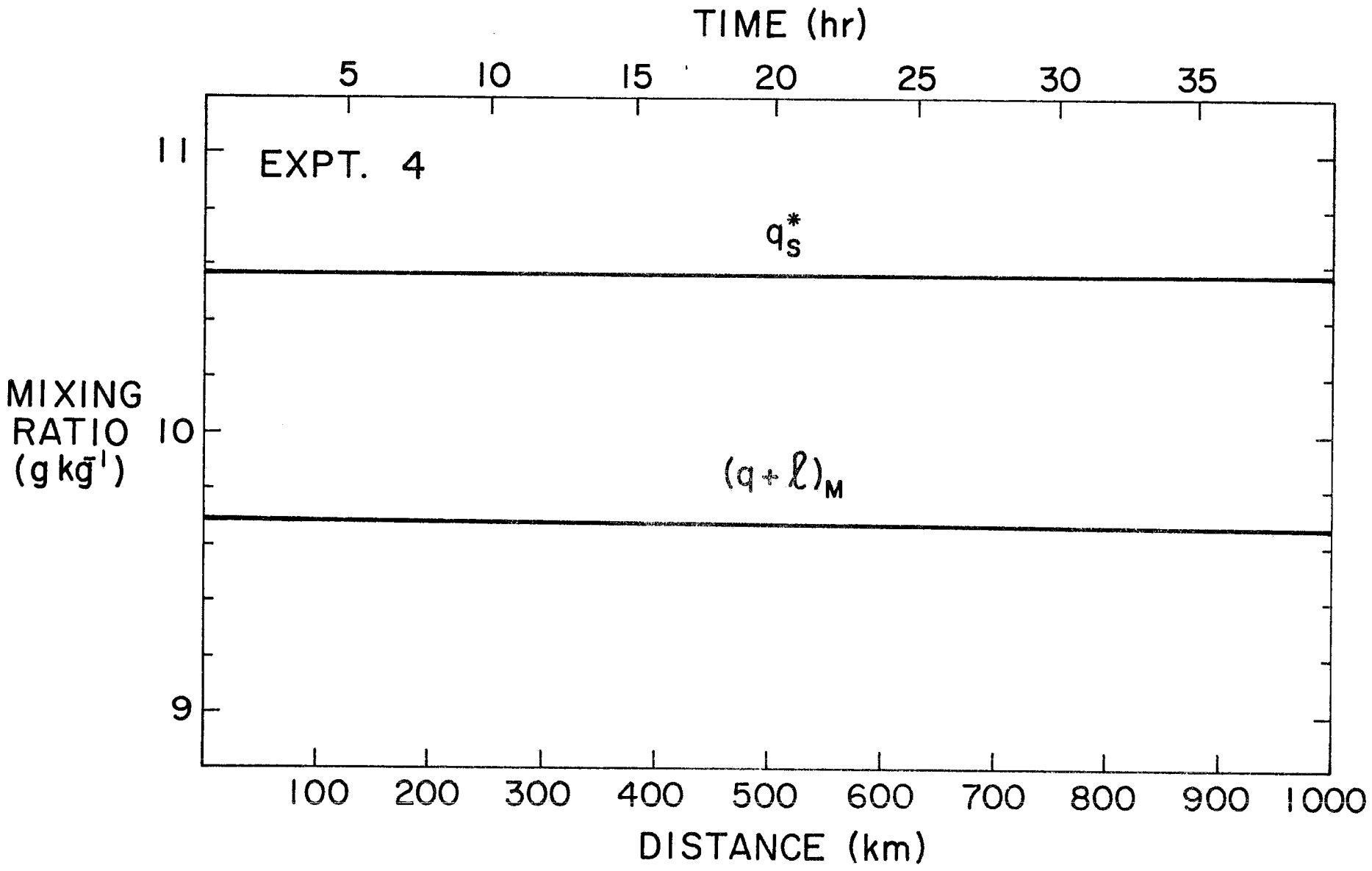

Figure 30c. Results for Experiment 4 (decreasing divergence, constant sea surface temperature).

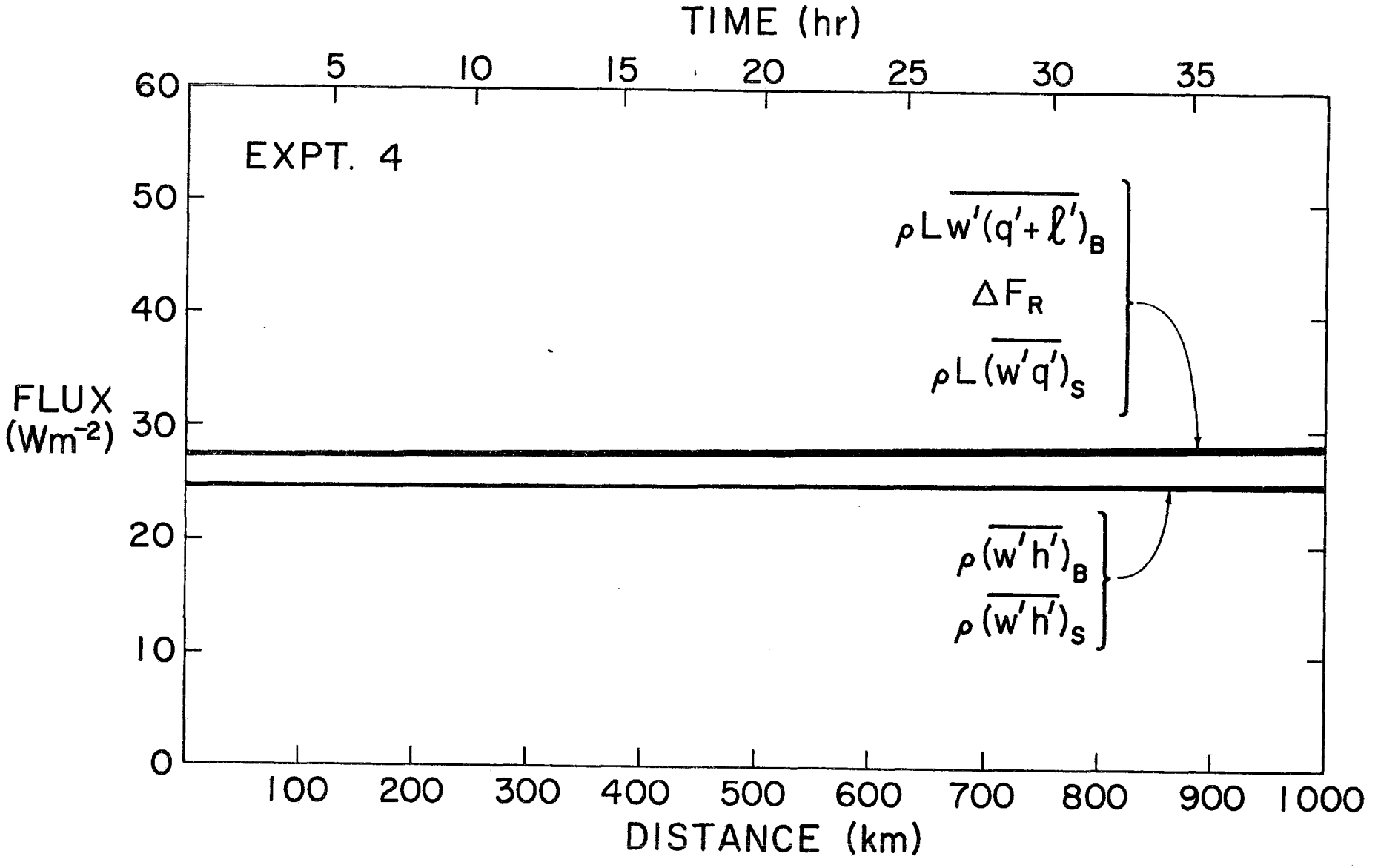

Figure 30d. Results for Experiment 4 (decreasing divergence, constant sea surface temperature).

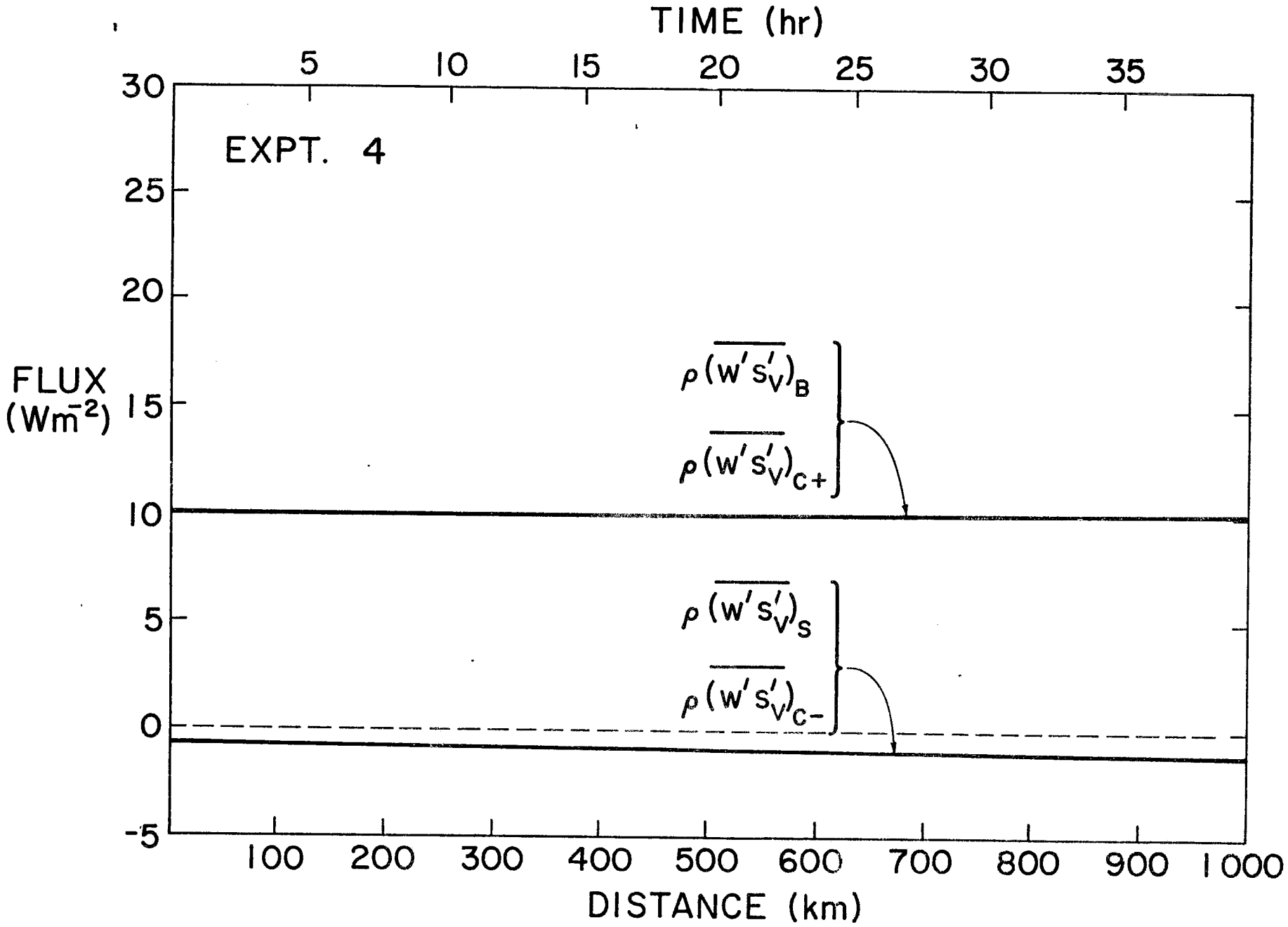

Figure 30e. Results for Experiment 4 (decreasing divergence, constant sea surface temperature).

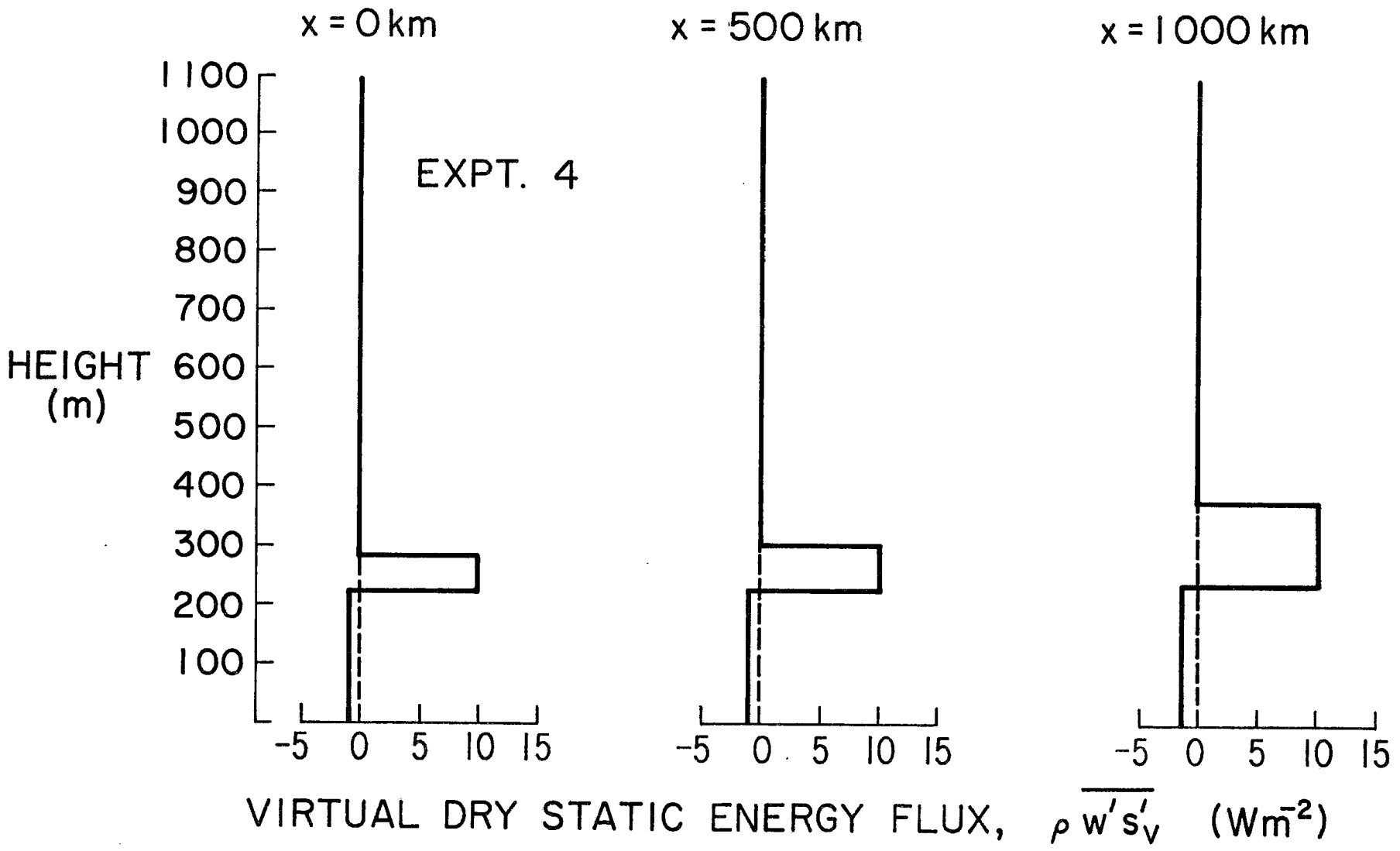

Figure 30f. Results for Experiment 4 (decreasing divergence, constant sea surface temperature).

homogeneous case, of the variables z_B, z_C, h_M, $(\overline{q+\ell})_M$, $\overline{w'h'}$, and $\overline{w'(q'+\ell')}$, only z_B has a strong dependence on divergence in the range $2 \times 10^{-6}s^{-1}$ to $6 \times 10^{-6}s^{-1}$.

Another interesting feature of these two experiments is the slow adjustment of cloud top. If z_B after 1000 km in Experiment 3 were in a horizontally homogeneous steady state, it would be the same as the initial value of z_B in Experiment 4. Conversely, if z_B after 1000 km in Experiment 4 were in a horizontally homogeneous steady state, it would be the same as the initial value of z_B in Experiment 3. Thus, even in weak advective situations we might expect to find z_B rather far from its horizontally homogeneous steady state value.

4.3 Adjustment times

In Experiment 5 (figure 31) mixed layer air, after flowing for a long period over water with a temperature of 14°C, instantaneously encounters water of 16°C. As expected an adjustment to the new conditions occurs. Cloud top and cloud base become higher, h_M and $(q+\ell)_M$ increase, and the fluxes of h and $q+\ell$ adjust to nearly double their original values. For z_B to change 63% of the way to its asymtotic value requires 80 hours, while for h_M and $(q+\ell)_M$ to change 63% of the way to their asymtotic values requires only 4 hours. This large difference in the adjustment time for z_B as opposed to that for h_M and $(q+\ell)_M$ appears to be a general feature of the model under typical eastern ocean situations. We shall offer an explanation of this phenomenon in section 5.

4.4 Wintertime air mass transformation

The gradients of sea surface temperature used in Experiments 1 and 2 are characteristic of marine stratocumulus of the eastern oceans. When

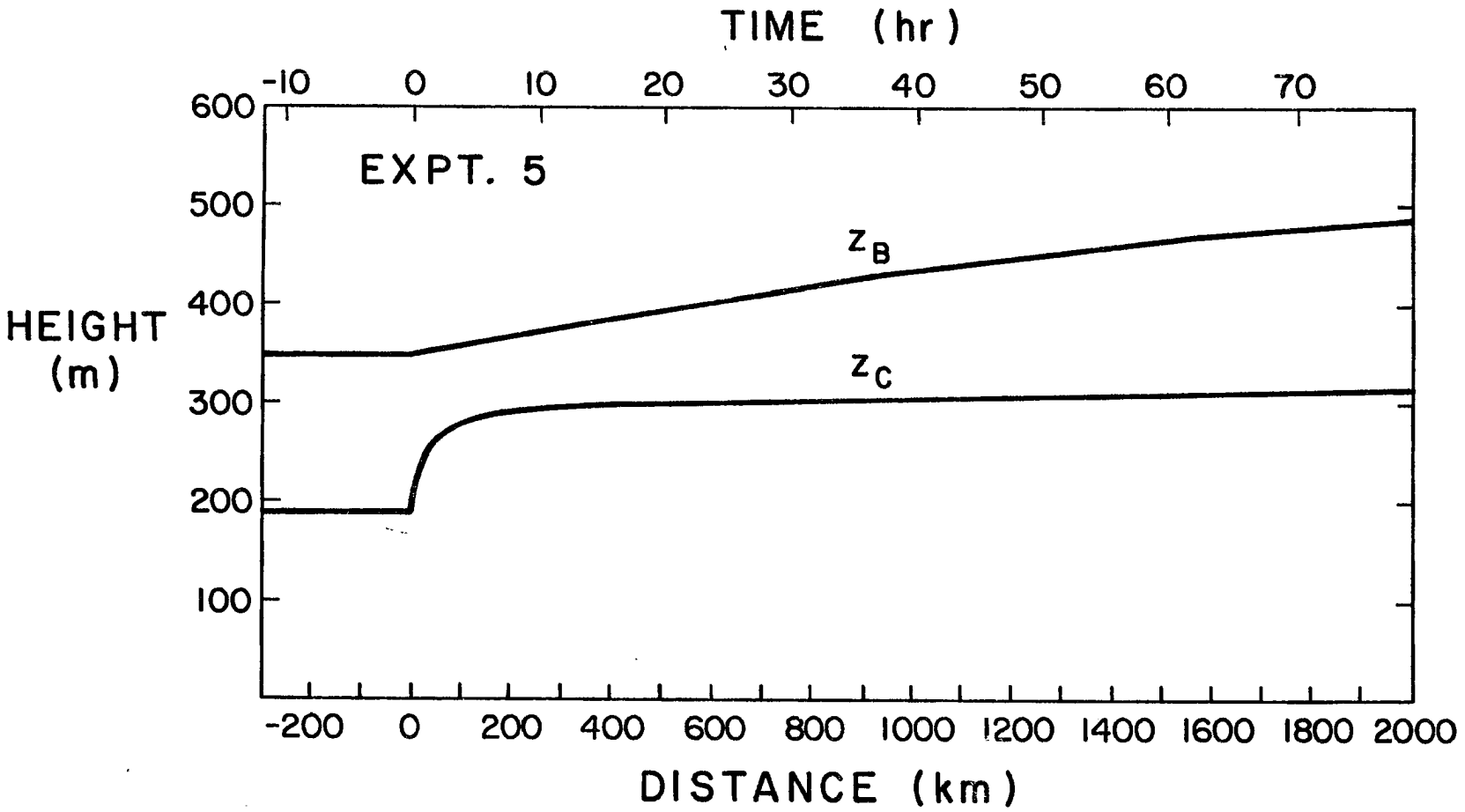

Figure 31a. Results for Experiment 5 (constant divergence, instantaneous 2°C increase in sea surface temperature).

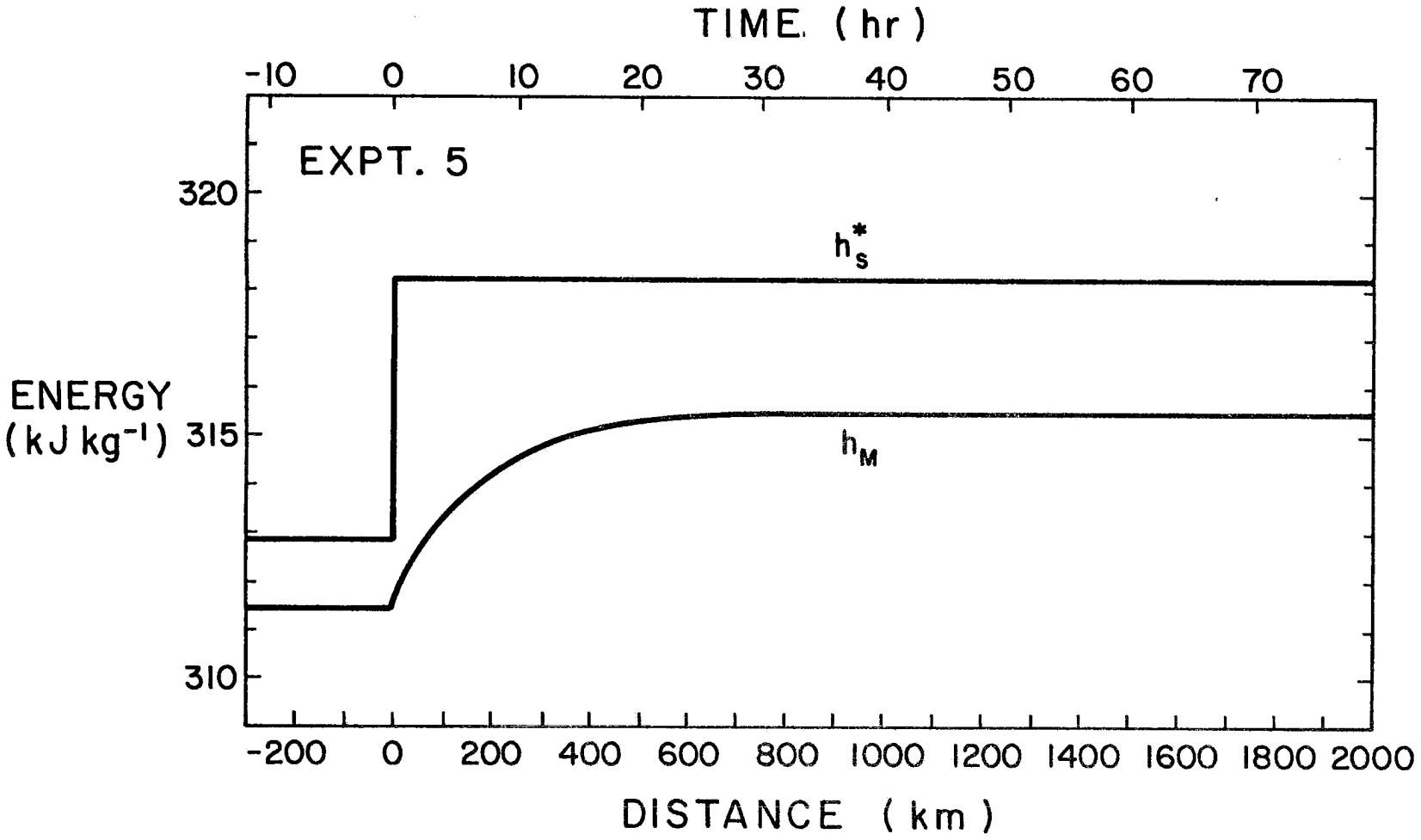

Figure 31b. Results for Experiment 5 (constant divergence, instantaneous 2°C increase in sea surface temperature).

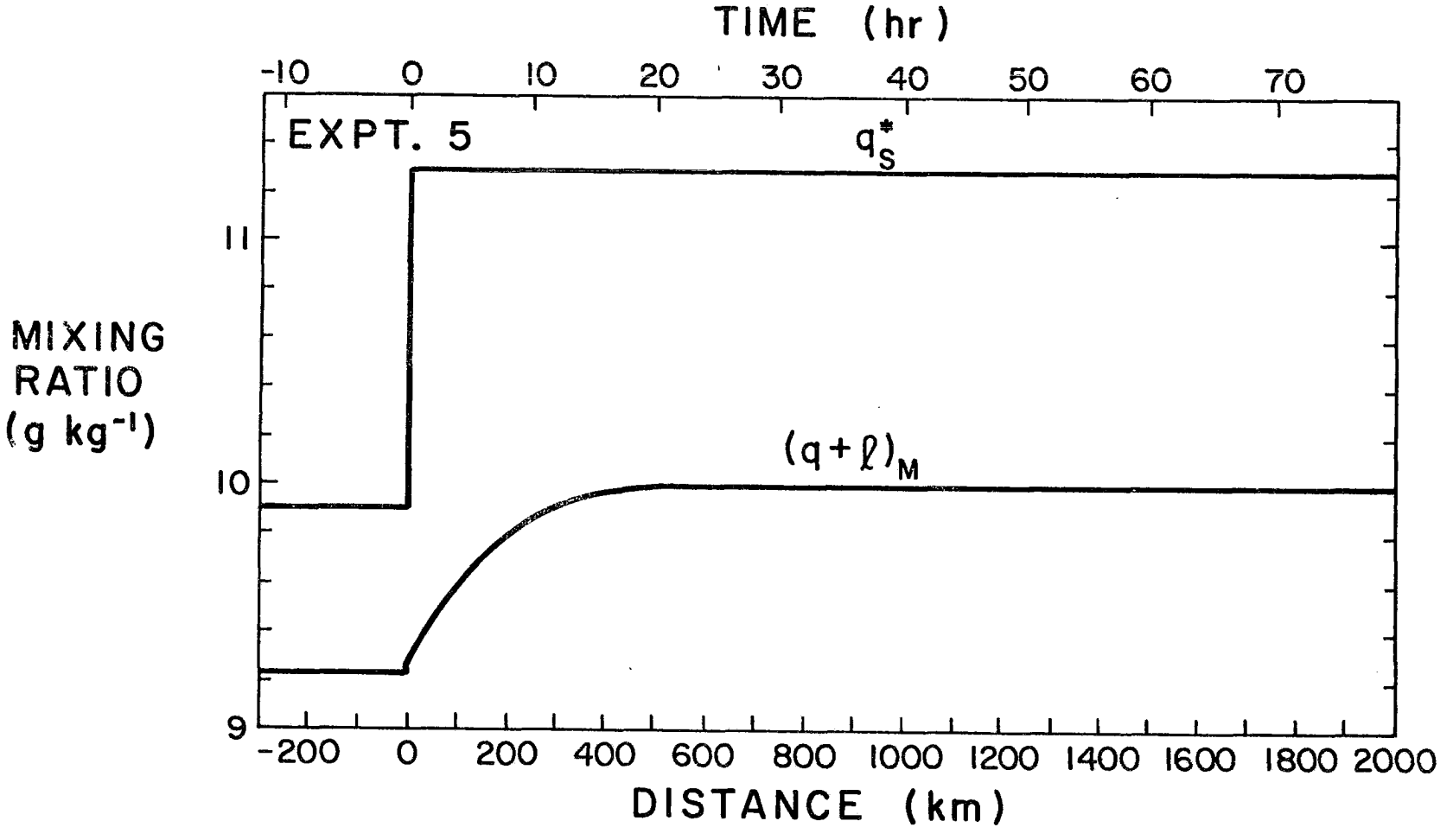

Figure 31c. Results for Experiment 5 (constant divergence, instantaneous 2°C increase in sea surface temperature).

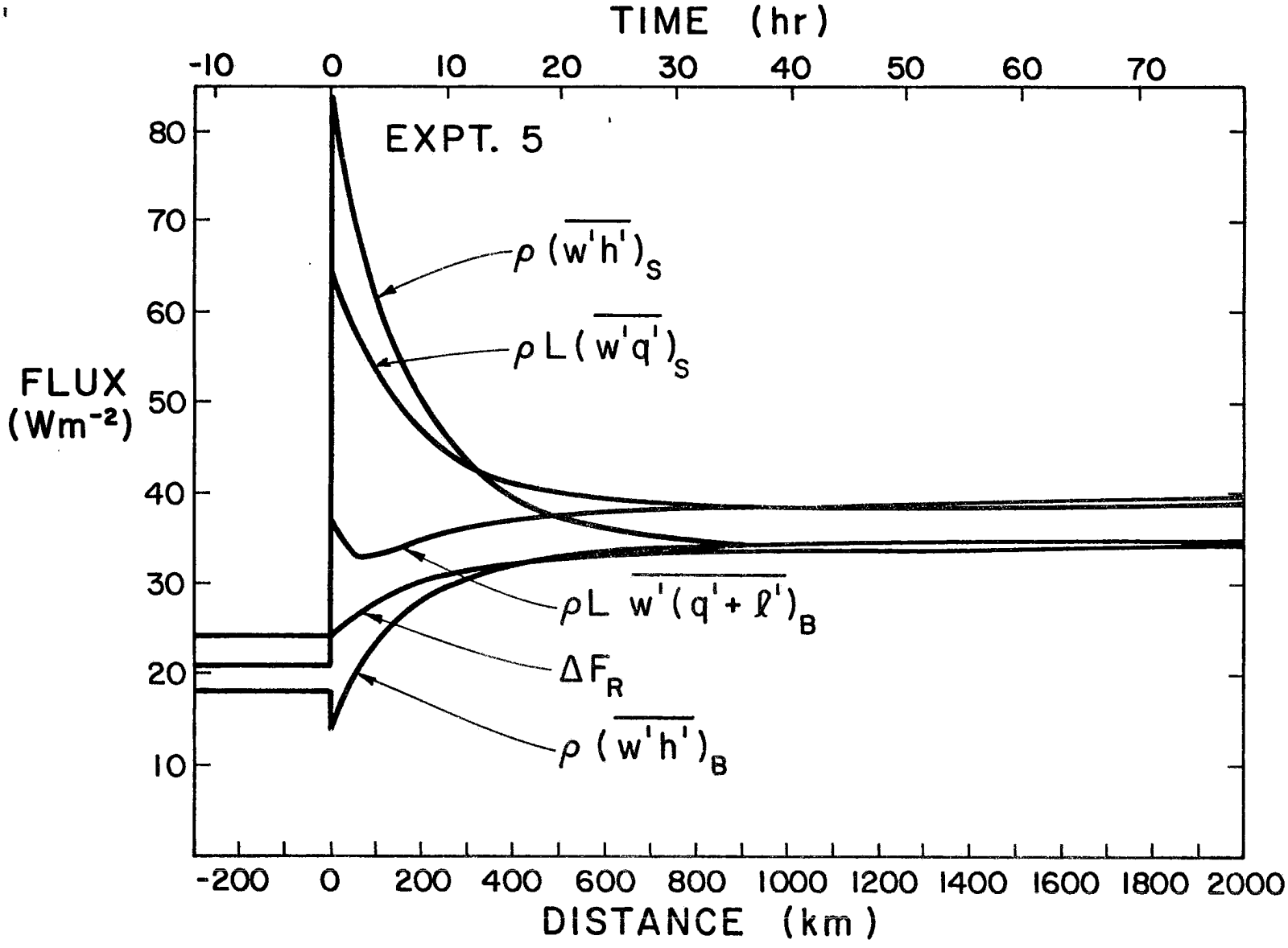

Figure 31d. Results for Experiment 5 (constant divergence, instantaneous 2°C increase in sea surface temperature).

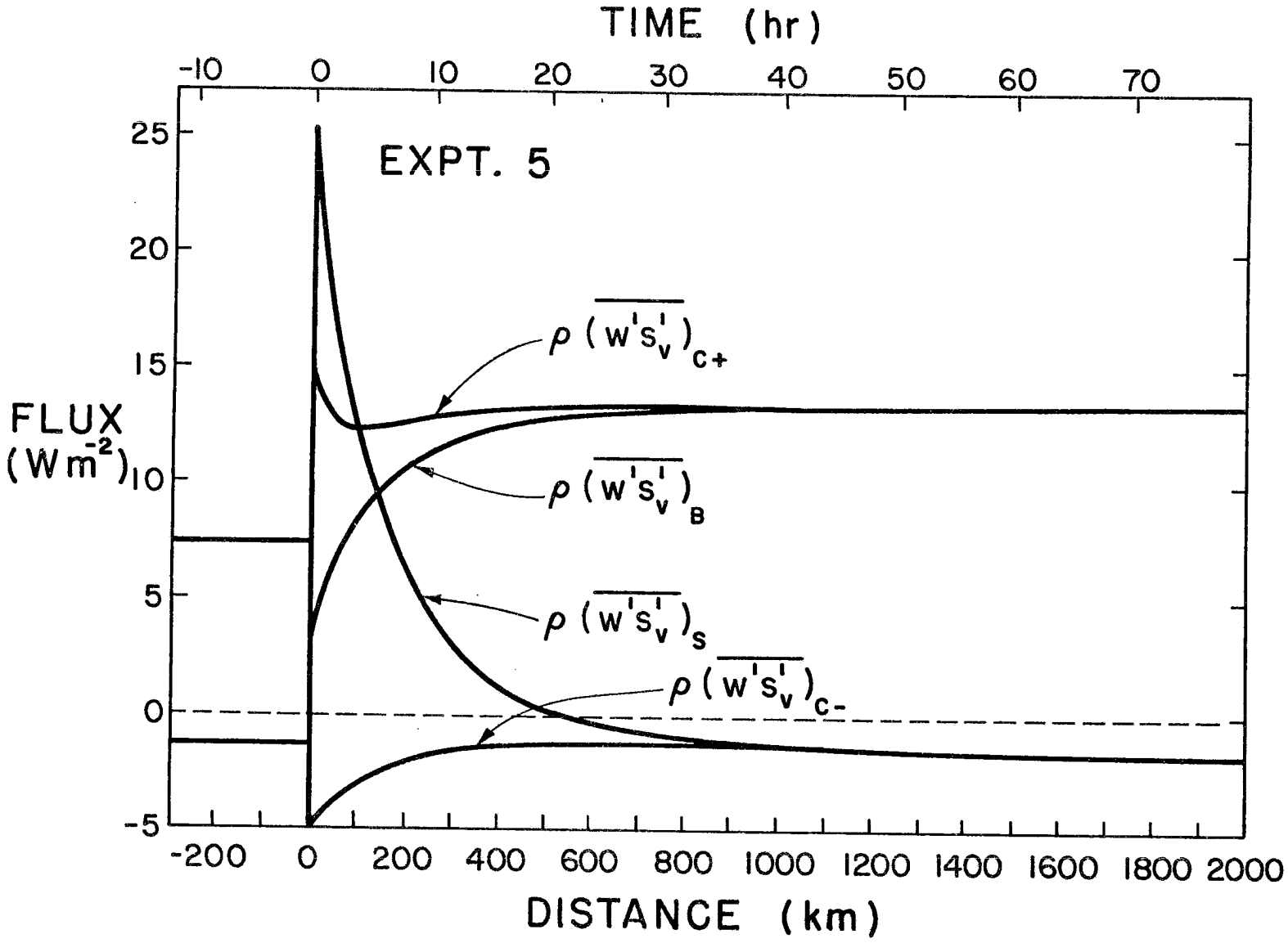

Figure 31e. Results for Experiment 4 (constant divergence, instantaneous 2°C increase in sea surface temperature).

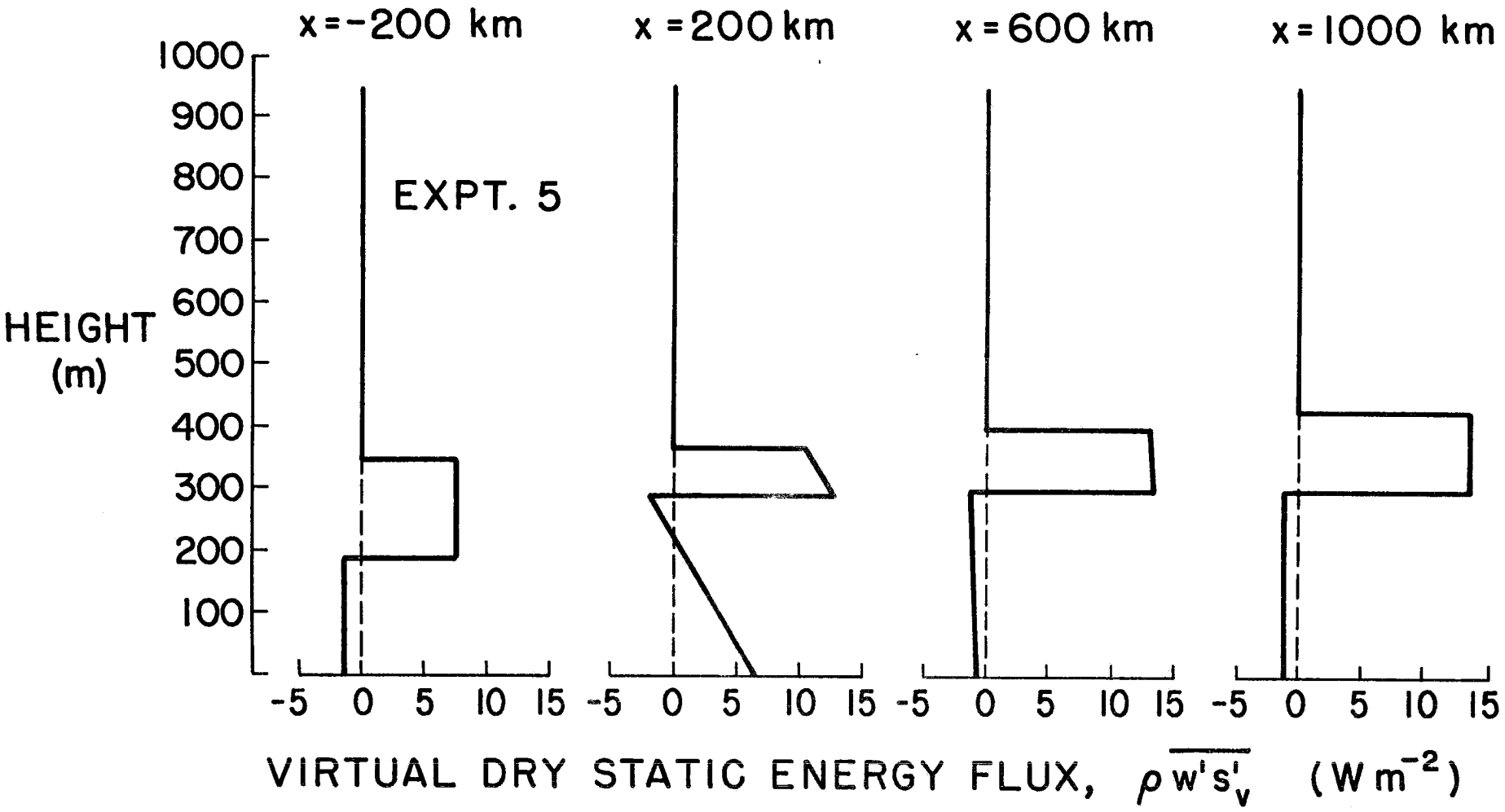

Figure 31f. Results for Experiment 5 (constant divergence, instantaneous 2°C increase in sea surface temperature).

wintertime cold air outbreaks occur in the eastern North Atlantic or in the East China Sea trajectories may cross regions of very intense sea surface temperature gradients associated with the Gulf Stream or the Kuroshio Current as was shown in figure 10. In Experiment 6 (figure 32) we attempt to simulate such air mass transformation by imposing the sea surface temperature field given by (4.1).

Figure 32a reveals the remarkable deepening of the mixed layer predicted by the model. The predicted deepening agrees reasonably well with the observed deepening (figure 10b). Since h_M (figure 32b) increases while $(q+\ell)_M$ (figure 32c) remains nearly unchanged, the cloud base height z_c increases. The turbulent fluxes (figures 32d-f) are very large by eastern ocean standards. As might be expected there is a tendency for the largest fluxes to occur just after the largest sea surface temperature gradient is encountered. Note that at about 1750 km the $\rho(\overline{w'h'})_S$ and $\rho L(\overline{w'q'})_S$ curves cross, i.e. the air-sea temperature difference vanishes. Thus, the mixed layer temperature has warmed up to the sea surface temperature while the mixed layer moisture has changed little. This will be discussed further in section 5.

4.5 Generalized method for horizontally inhomogeneous solutions

So far we have discussed idealized horizontally inhomogeneous solutions. In order to construct the steady state horizontally inhomogeneous properties of the mixed layer as a function of longitude and latitude we need to solve the governing set of equations for many neighboring trajectories. When solving the governing set of equations we must specify the sea surface temperature and pressure, the large-scale wind speed and divergence, and the temperature and humidity of the

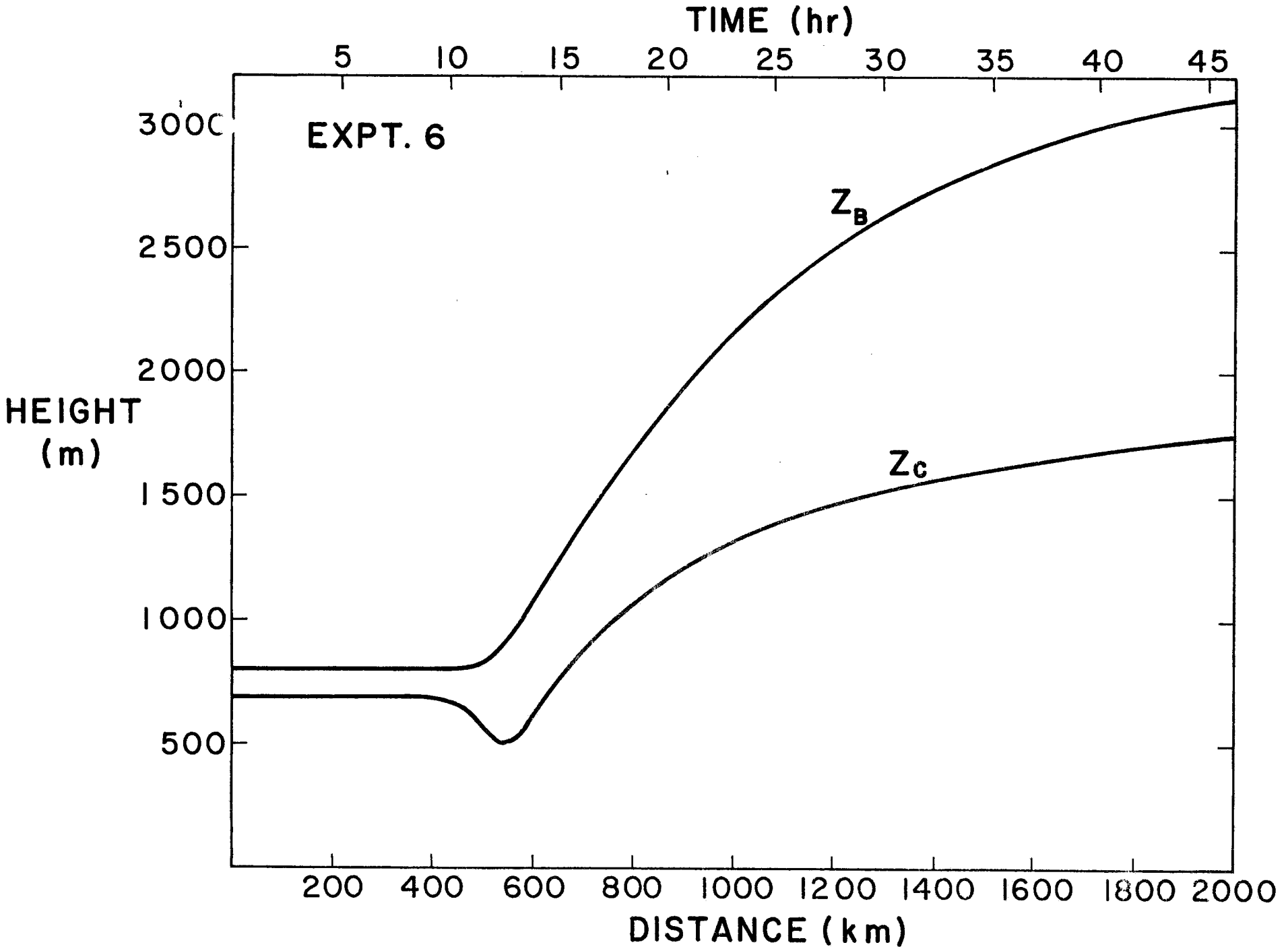

Figure 32a. Results for Experiment 6 (constant divergence, temperature rapidly increasing from 7°C to 21°C).

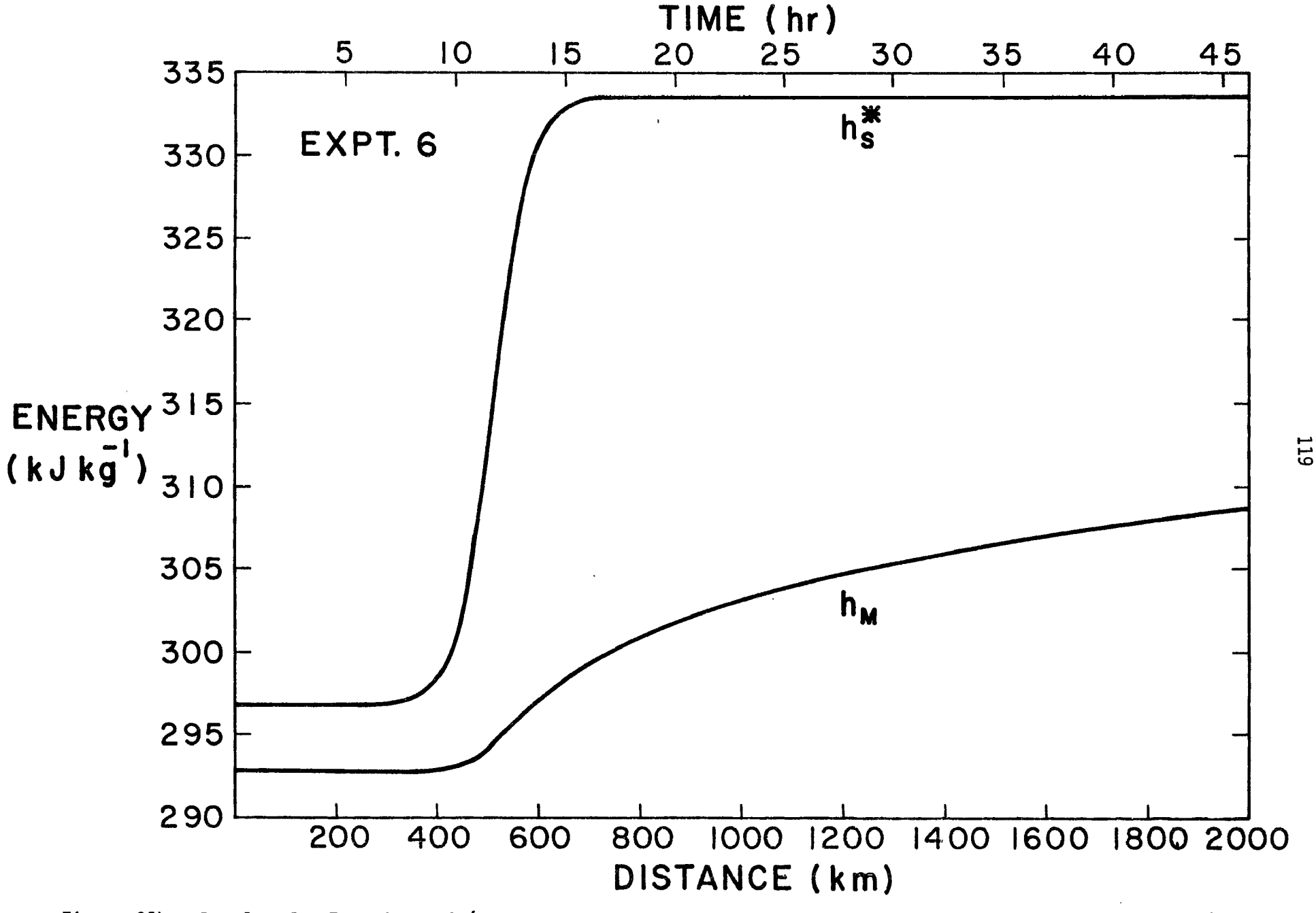

Figure 32b. Results for Experiment 6 (constant divergence, temperature rapidly increasing from 7°C to 21°C).

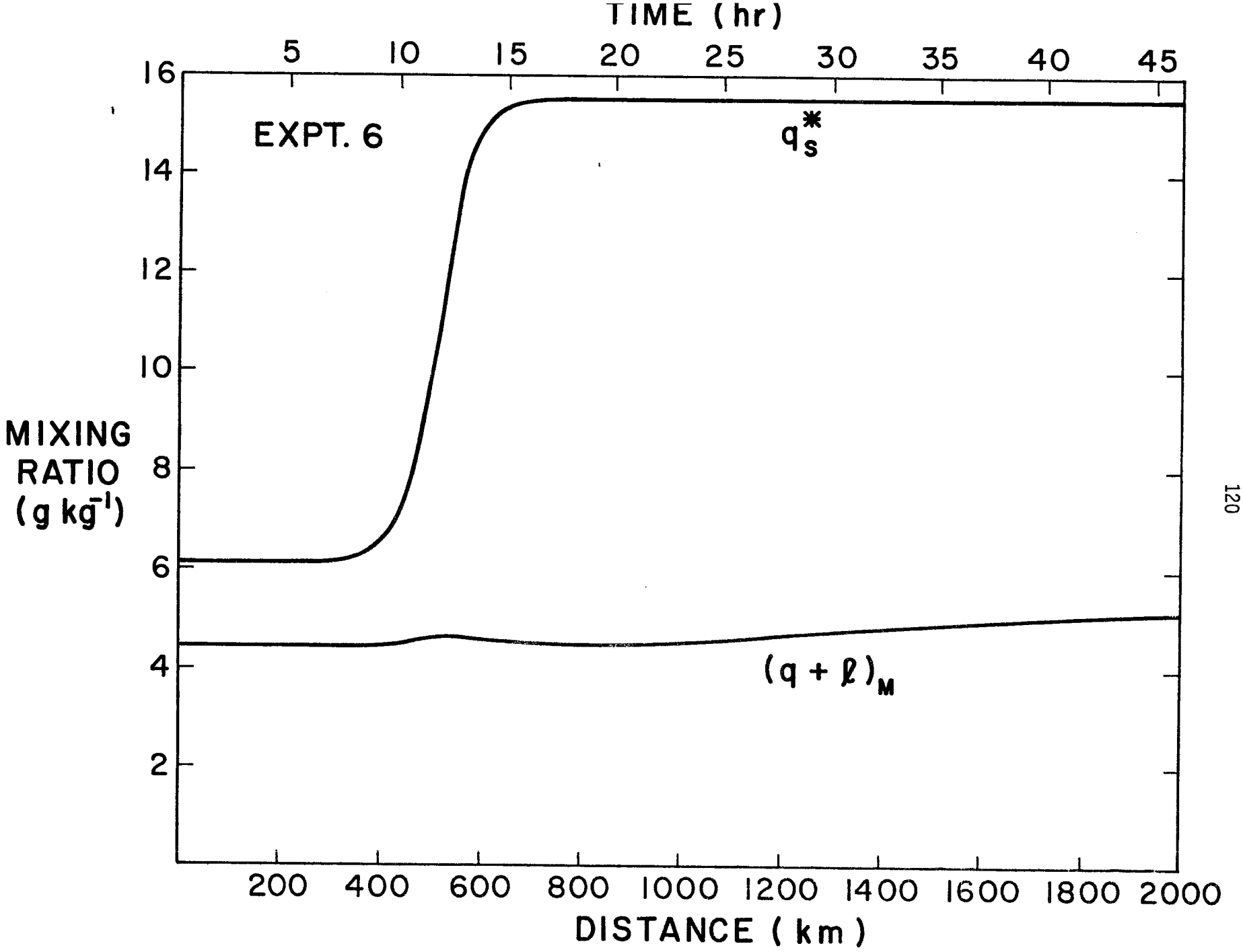

Figure 32c. Results for Experiment 6 (constant divergence, temperature rapidly increasing from 7°C to 21°C).

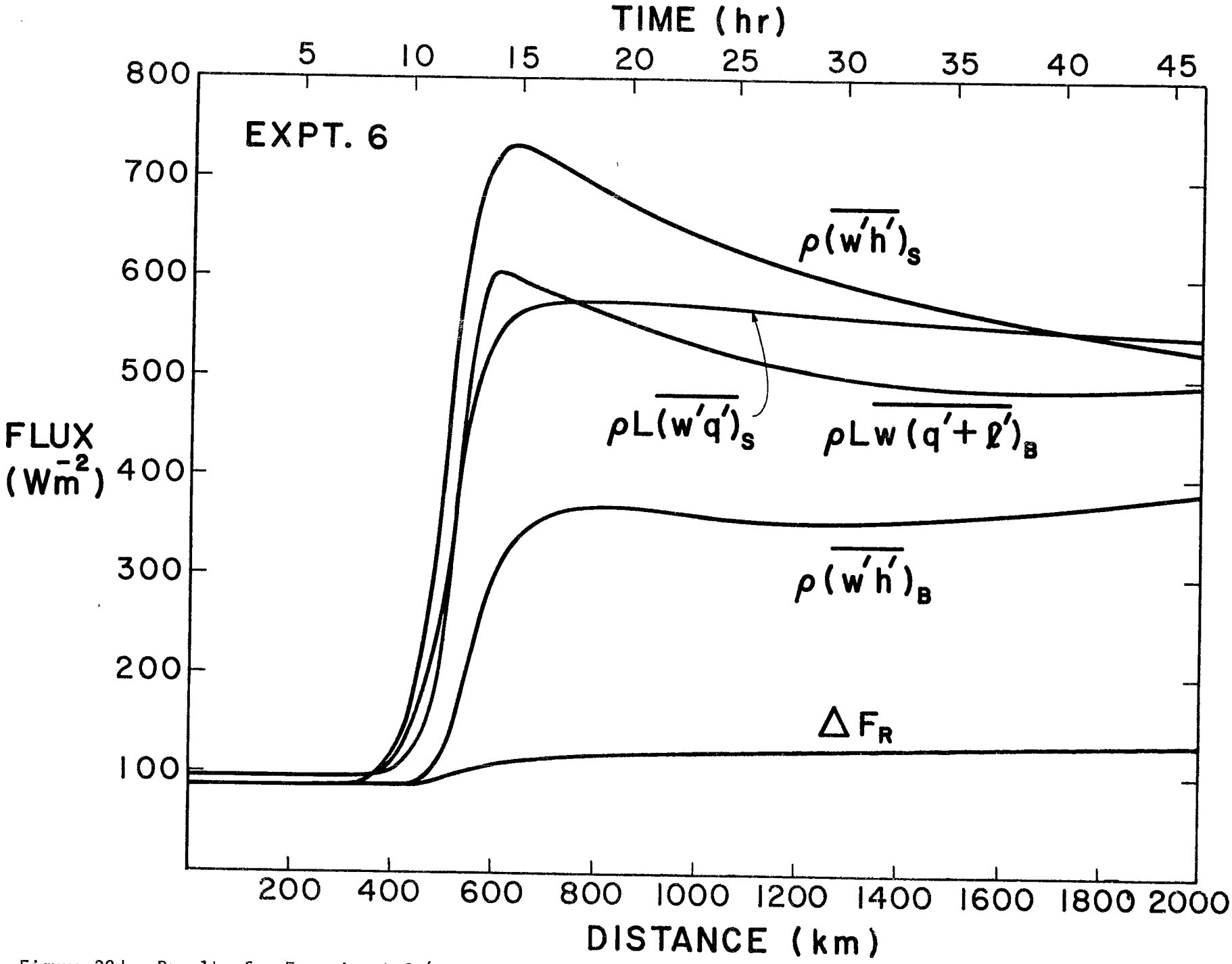

Figure 32d. Results for Experiment 6 (constant divergence, temperature rapidly increasing from 7°C to 21°C).

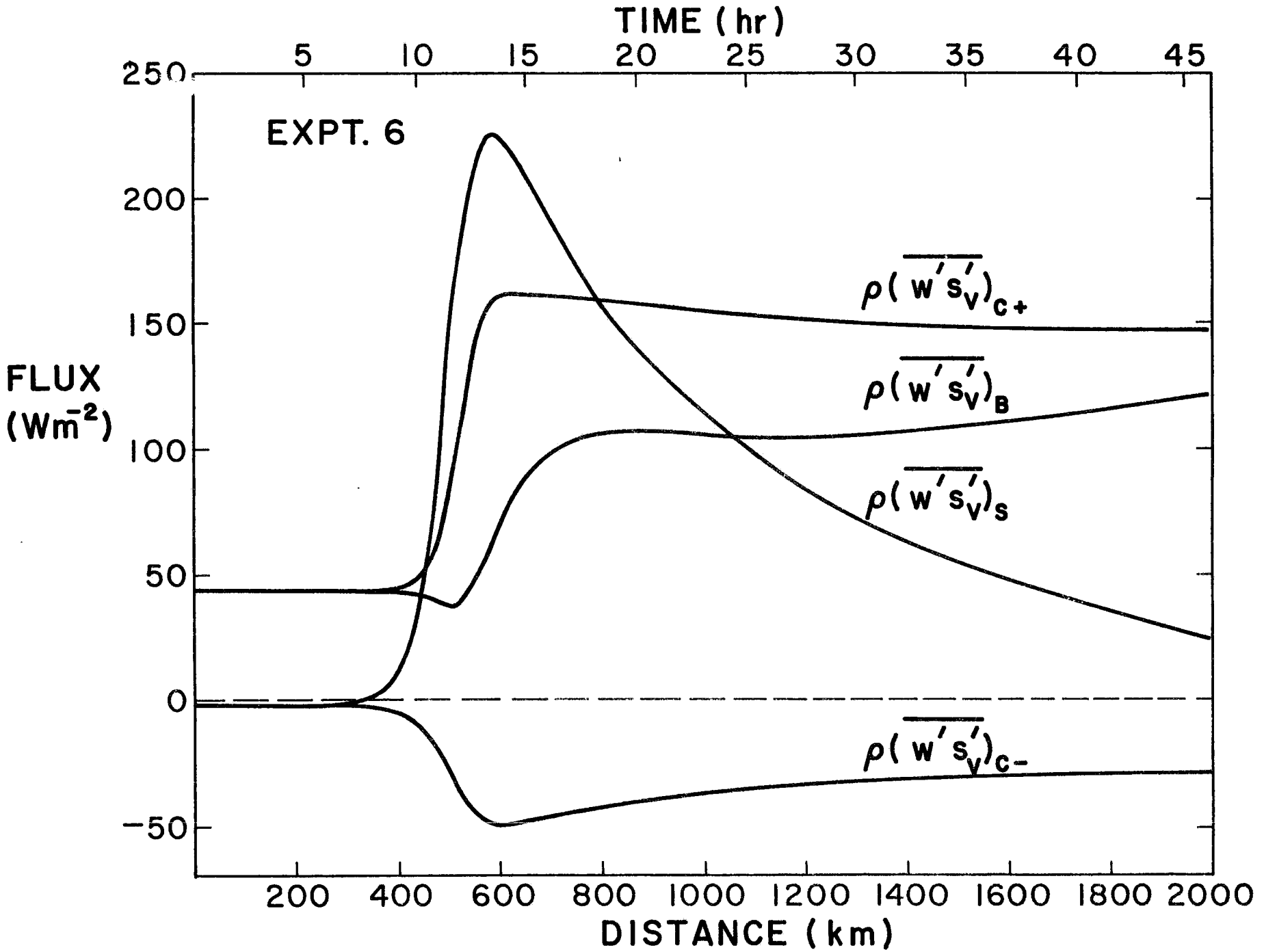

Figure 32e. Results for Experiment 6 (constant divergence, temperature rapidly increasing from 7°C to 21°C).

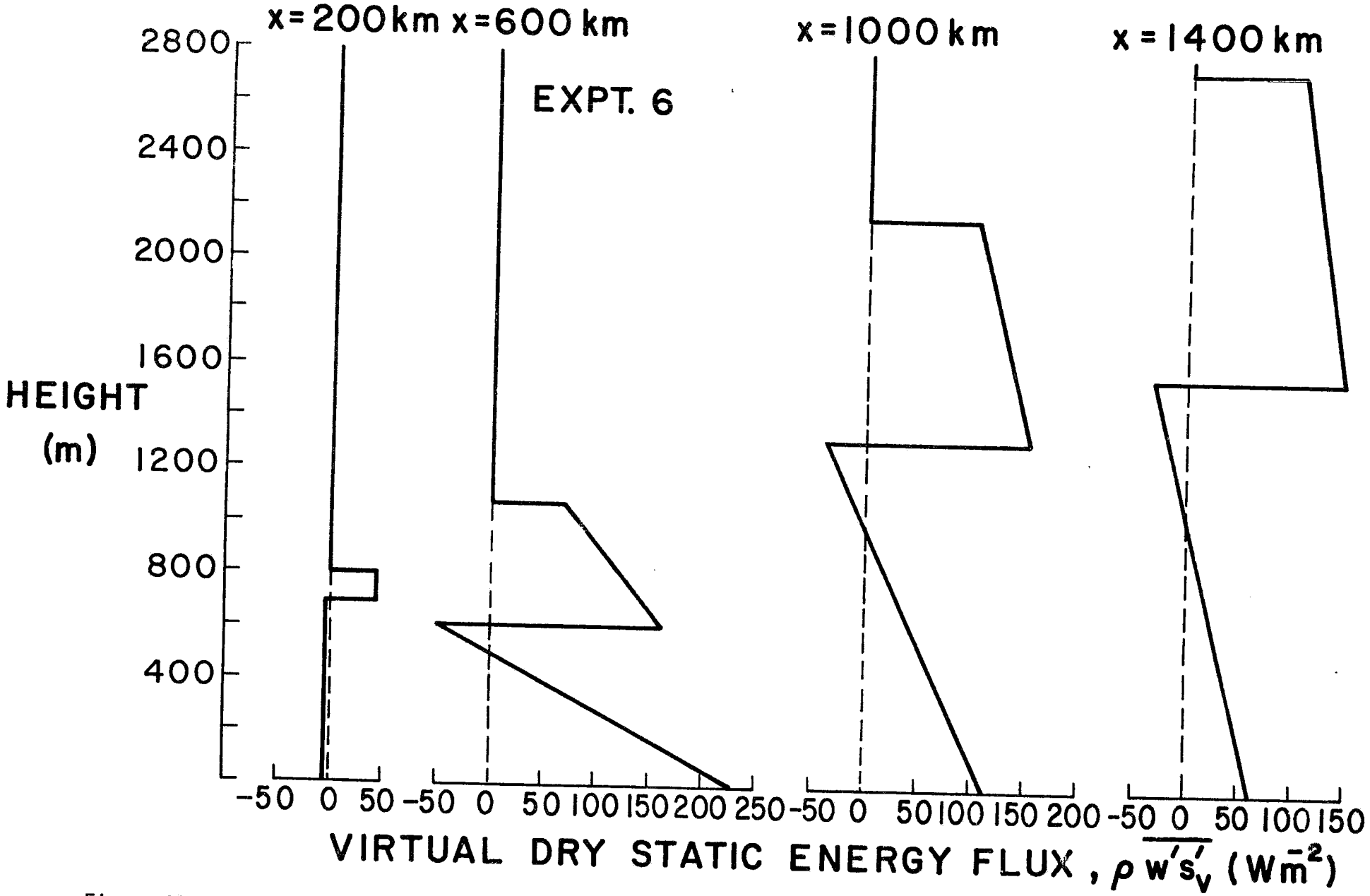

Figure 32f. Results for Experiment 6 (constant divergence, temperature rapidly increasing from 7°C to 21°C).

air above the mixed layer, all as functions of the downstream distance x. Since wind speed and divergence are required along a trajectory, neighboring trajectories must be constructed in a manner consistent with the specified wind speed and divergence. To accomplish this we can begin with two dimensional (longitude, latitude) mean monthly fields of large-scale wind speed and direction (e.g. as given by Neiburger et al., 1961, or Miller and Stevenson, 1974). From the speed and direction we can compute the two dimensional field of large-scale divergence. Beginning at some initial longitude and latitude we can also compute from the speed and direction a sequence of longitude-latitude points which lie along a trajectory, and we can label each point in terms of the elapsed time from the initial point. This problem can be solved by spherical trigenometry considerations as follows.

Suppose we are at the longitude-latitude point (λ_i, ϕ_i) on the trajectory and wish to proceed downwind in the direction α_i to the next longitude-latitude point $(\lambda_{i+1}, \phi_{i+1})$ as shown in figure 33. The three great circles connecting the three pairs of points (λ_i, ϕ_i) and $(\lambda_{i+1}, \phi_{i+1})$, the north pole and (λ_i, ϕ_i), and the north pole and $(\lambda_{i+1}, \phi_{i+1})$ form the sides of a spherical triangle. The cosine law for sides states that the cosine of a side of a spherical triangle is equal to the product of the cosines of the other two sides plus the product of the sines of those two sides multiplied by the cosine of their included angle. Applying the cosine law for sides to the great circle connecting the north pole and $(\lambda_{i+1}, \phi_{i+1})$ we obtain

$$\sin \phi_{i+1} = \sin \phi_i \cos\left(\frac{d}{a}\right) + \cos \phi_i \sin\left(\frac{d}{a}\right) \cos \alpha_i. \qquad (4.2)$$

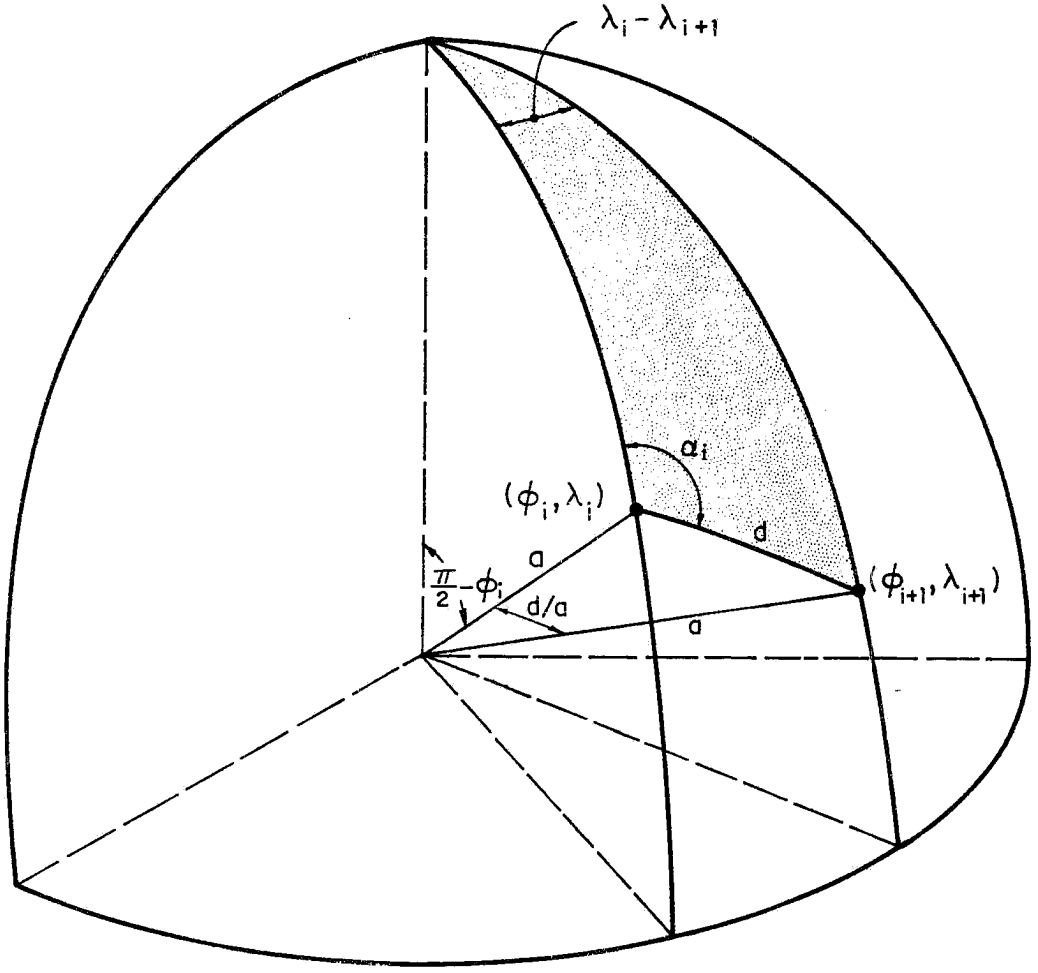

Figure 33. Schematic diagram illustrating the method used for a trajectory calculation.

Applying the cosine law for sides to the great circle connecting (λ_i, ϕ_i) and $(\lambda_{i+1}, \phi_{i+1})$ we obtain

$$\cos\left(\frac{d}{a}\right) = \sin\phi_i \sin\phi_{i+1} + \cos\phi_i \cos\phi_{i+1} \cos(\lambda_i - \lambda_{i+1}), \quad (4.3)$$

which can also be wirtten as

$$\cos(\lambda_i - \lambda_{i+1}) = \frac{\cos\left(\frac{d}{a}\right) - \sin\phi_i \sin\phi_{i+1}}{\cos\phi_i \cos\phi_{i+1}}. \quad (4.4)$$

The time elapsed in the air travel distance d is

$$t_{i+1} - t_i = \frac{d}{V_i}. \quad (4.5)$$

Knowing the coordinates (λ_i, ϕ_i), the wind direction α_i, the wind speed V_i, and the specified downstream space increment d, the latitude of the next downstream point can be computed from (4.2), its longitude from (4.4), and the time increment between points from (4.5).

Model output derived using the above method can be compared to mean monthly maps of inversion height, air-sea temperature difference, etc. Although the method is open to the criticism that the response to average conditions is not necessarily the average response, it is probably the best that can be done with presently available data. The method has been used by Steiner and Schubert (1977) to compute the properties of the stratocumulus regime off the west coast of South America.

5. Approximate analytic solutions

In this section we shall derive approximate analytic solutions to the governing equations. Assuming that w_B is given by $-Dz_B$, we can eliminate $(\overline{w'h'})_S$ and $(\overline{w'h'})_B$ from (2.1), (2.3) and (2.5) to obtain

$$\frac{dh_M}{dt} + \left[\frac{C_T V}{z_B} + D + \frac{1}{z_B}\frac{dz_B}{dt}\right]h_M = \frac{C_T V}{z_B} h_S^* + \left[D + \frac{1}{z_B}\frac{dz_B}{dt}\right] h(z_{B+}) - \frac{\Delta F_R}{\rho z_B} \quad . \tag{5.1}$$

Similarly, we can eliminate $(\overline{w'q'})_S$ and $\overline{w'(q'+\ell')}_B$ from (2.2), (2.4) and (2.6) to obtain

$$\frac{d(q+\ell)_M}{dt} + \left[\frac{C_T V}{z_B} + D + \frac{1}{z_B}\frac{dz_B}{dt}\right](q+\ell)_M = \frac{C_T V}{z_B} q_S^* + \left[D + \frac{1}{z_B}\frac{dz_B}{dt}\right] q(z_{B+}) \quad . \tag{5.2}$$

Equations (5.1) and (5.2) can be regarded as differential equations which give the variation of h_M and $(q+\ell)_M$ along the trajectory if the variations of z_B and ΔF_R along the trajectory are known. The solutions to (5.1) and (5.2) are

$$h_M(t) = h_M(o) + \int_o^t a(t,t') \left\{ \frac{C_T V(t')}{z_B(t')} \left[h_S^*(t') - h_M(o)\right] \right.$$

$$\left. + \left[D(t') + \frac{1}{z_B(t')}\frac{dz_B}{dt'}\right]\left[h(z_{B+}(t')) - h_M(o)\right] - \frac{\Delta F_R(t')}{\rho z_B(t')} \right\} dt' \quad , \tag{5.3}$$

and

$$(q+\ell)_M(t) = (q+\ell)_M(o) + \int_o^t a(t,t') \left\{ \frac{C_T V(t')}{z_B(t')} \left[q_S^*(t') - (q+\ell)_M(o) \right] \right.$$

$$\left. + \left[D(t') + \frac{1}{z_B(t')} \frac{dz_B}{dt'} \right] \left[q(z_{B+}(t')) - (q+\ell)_M(o) \right] \right\} dt' \ , \qquad (5.4)$$

where

$$a(t,t') = \exp \left\{ -\int_{t'}^t \left[\frac{C_T V(t'')}{z_B(t'')} + D(t'') + \frac{1}{z_B(t'')} \frac{dz_B}{dt''} \right] dt'' \right\} . \qquad (5.5)$$

The solutions (5.3) and (5.4) show that the effects of upstream conditions are gradually forgotten as the result of the three terms in the integrand of (5.5), i.e. surface transfer ($\frac{C_T V}{z_B}$), entrainment due to mean subsidence (D), and entrainment due to boundary layer deepening in the downstream direction ($\frac{1}{z_B} \frac{dz_B}{dt}$). The integrand of (5.5) is always positive since both $\frac{C_T V}{z_B}$ and $D + \frac{1}{z_B} \frac{dz_B}{dt}$ (which is directly proportional to the net mass flow across the top of the mixed layer) are always positive. How fast are upstream conditions on h_M and $(q+\ell)_M$ forgotten? As an example let us consider Experiment 5 of the last section. Even after the instantaneous sea surface change, the quantities $\frac{C_T V}{z_B} : D : \frac{1}{z_B} \frac{dz_B}{dt}$ do not vary much along the trajectory and have typical values of 28 : 4 : 2 in units of $10^{-6} s^{-1}$. Thus, a(t,t') can be roughly approximated by $\exp \left\{ -\frac{C_T V}{z_B} (t - t') \right\}$, which is shown in figure 34. In this case it appears that, as far as h_M and $(q+\ell)_M$ are concerned, conditions more than 24 hours upstream are more than 90% forgotten. As a second example let us consider Experiment 6. At 600-700 km

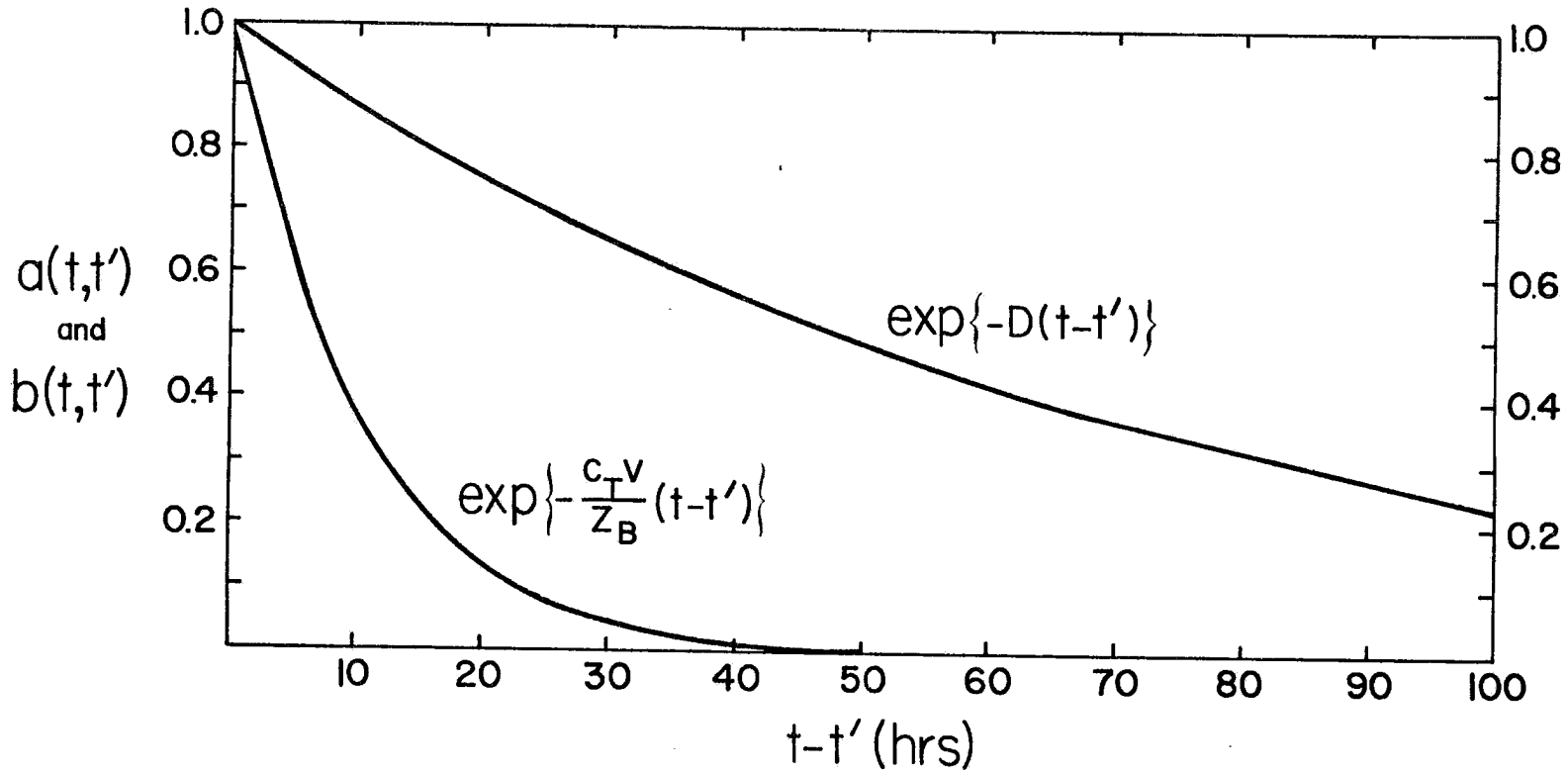

Figure 34. The functions $\exp\{-\frac{C_T V}{z_B}(t-t')\}$ and $\exp\{-D(t-t')\}$ are approximations to $a(t,t')$ and $b(t,t')$, respectively. The curves are based on Experiment 5, in which $C_T = 0.0015$, $V = 7\ ms^{-1}$, $D = 4 \times 10^{-6} s^{-1}$, and $z_B \simeq 375$ m.

the quantities $\frac{C_T V}{z_B} : D : \frac{1}{z_B}\frac{dz_B}{dt}$ have the values 15 : 10 : 32 in units of $10^{-6}s^{-1}$, while at 1600-1700 km they have the values 6 : 10 : 3. These figures are in sharp contrast to Experiment 5, indicating that the AMTEX situation is one in which mixing across cloud top plays a very important role. According to (5.3) this mixing across cloud top will tend to increase h_M, but according to (5.4) it will tend to decrease $(q+\ell)_M$. Thus, in the AMTEX situation so much dry air is entrained across cloud top that the mixed layer does not moisten. However, the atmospheric column as a whole is rapidly moistening due to the increase in z_B.

To determine the variation of z_B along the trajectory we could combine (2.3), (2.4), (2.5), (2.6), (2.10), (2.22), (2.31), (2.32), (5.3) and (5.4) into a single differential equation for z_B. Although this can in principle be done, it leads to an extremely complicated equation for z_B. Here we shall consider only the minimum entrainment case and assume that the minimum $\overline{w's_v'}$ occurs at the surface.[1] The assumption that $(\overline{w's_v'})_S$ vanishes decouples the cloud base relation (2.10) from the entrainment relation, so that we have simply

$$h_M - (1-\varepsilon\delta)L(q+\ell)_M = s^*_{vs} \quad . \tag{5.6}$$

Using (5.1), (5.2) and (5.6) we can easily obtain

$$\frac{dz_B}{dt} + \left\{ D - \frac{1}{[s_v(z_{B+})-s^*_{vs}]}\frac{ds^*_{vs}}{dt} \right\} z_B = \frac{\Delta F_R}{\rho[s_v(z_{B+})-s^*_{vs}]} \quad , \tag{5.7}$$

[1]The minimum occurs at the surface in Experiments 2, 3 and 4 of the last section.

which is a differential equation for z_B provided ΔF_R and $s_v(z_{B+})$ are known. The solution of (5.7) is

$$z_B(t) = z_B(0) + \int_0^t b(t,t') \left\{ \frac{1}{[s_v(z_{B+}(t')) - s^*_{vs}(t')]} \left[\frac{\Delta F_R(t')}{\rho} + \frac{ds^*_{vs}}{dt'} \right] - D(t') z_B(0) \right\} dt' \quad , \tag{5.8}$$

where

$$b(t,t') = \exp\left\{ -\int_{t'}^t \left[D(t'') - \frac{1}{s_v(z_{B+}(t'')) - s^*_{vs}(t'')} \frac{ds^*_{vs}}{dt''} \right] dt'' \right\} . \tag{5.9}$$

After the instantaneous sea surface temperature change of Experiment 5, $\frac{ds^*_{vs}}{dt}$ is zero so that $b(t,t')$ can be written $\exp\{-D(t-t')\}$, which is also shown in figure 34. Since $\frac{C_T V}{Dz_B}$ for Experiment 5 is about seven, the memory time for z_B is about seven times the memory time for h_M and $(q+\ell)_M$.

Although we have derived (5.7) - (5.9) using the assumption that $(\overline{w's_v'})_S$ vanishes, our experience with numerical solutions indicates that the longer adjustment time for z_B compared to h_M and $(q+\ell)_M$ is a general feature, at least under typical eastern ocean situations. Perhaps additional analytic progress on this problem could be made with the two time scale procedure described by Cole (1968).

6. An observational program

With Lilly's work and the extensions of his work which have followed it seemed to us that the state of the theory of marine stratocumulus convection was considerably more advanced than the observations. This indicated the need for an observational program taking advantage of modern aircraft turbulence measuring techniques. Such a program could probably be carried out at any of the five regions discussed in section 1 and, were it an ideal program, would measure all the model input and output quantities listed in the first and third columns of Table 7. An ideal program seems to be almost within reach[1] of the NCAR Electra aircraft measurement capabilities, which are summarized in Table 12. The inertial navigation system allows accurate determination of the velocity of the aircraft with respect to the earth, while the airspeed, attack angle, and sideslip angle measurements allow computation of the velocity of the air with respect to the aircraft. The difference of these two is the velocity of the air with respect to the earth. This velocity, in combination with the air temperature, water vapor, and liquid water measurements in principle allows the computation of heat, water vapor, and liquid water fluxes. In addition, radiation, sea surface temperature, and mean profile measurements are possible. In June 1976 a program of five NCAR Electra flights totaling about thirty hours was carried out off the California coast. A more detailed discussion of this program is given in Wakefield and Schubert (1976). An example of cloud conditions and mean profile data

[1]The large-scale divergence appears to be too small to measure using only an aircraft.

TABLE 12. Summary of NCAR Electra measurement capabilities.

Parameter Measured	Instrument
1. Aircraft pitch and roll	Inertial Navigation System
2. Aircraft heading and ground speed	Inertial Navigation System
3. Aircraft vertical velocity	Inertial Navigation System
4. Aircraft latitude and longitude	Inertial Navigation System
5. Angles of attack and sideslip	Fixed and rotating vanes
6. Airspeed	Wingtip and boom pilot-static tubes
7. Altitude	Radio and pressure altimeters
8. Air temperature	Platinum resistance wire, tungsten resistance wire, wet bulb thermistor, bolometric radiometer (PRT-6)
9. Water vapor content	Thermoelectric hygrometer, Lyman-alpha hygrometer, microwave refractometer
10. Liquid water content	Hot-wire flowmeter, Knollenberg Forward Scattering Spectrometer Probe
11. Radiation	Upward and downward looking pyrgeometers and pyranometers
12. Sea surface temperature	Bolometric radiometer (PRT-5)

for the last flight was shown in figures 4 and 5. On this flight many ten minute crosswind legs were made in the subcloud and cloud layers in an attempt to determine the various turbulent fluxes. The results will be presented in a future paper.

To make a more complete observational study would appear to require a large increase in effort and cost. For example, to measure large-scale divergence and thus be able to compute turbulent fluxes as residuals from the large-scale heat and moisture budget equations would require an array of ships with tethered balloons. Such a program has already been proposed as part of the Global Atmospheric Research Program.

7. Summary and conclusions

We have reviewed the climatology of the various marine stratocumulus regimes and presented a combined convective-radiative model for their study. Both horizontally homogeneous and horizontally inhomogeneous solutions to the model have been investigated. How could the model be further improved? One possibility is to include the momentum equations so that surface winds and divergence are no longer externally specified quantities but are dependent variables of the model. One might then specify only the sea surface temperature and pressure fields. Another possibility for improvement is to generalize the model to include both stratocumulus and trade cumulus convection. Then trajectories could be followed closer to the ITCZ, and one could study the transition from stratocumulus to trade cumulus convection. Such a model has recently been developed by Albrecht (1977) along lines first proposed by Betts (1973).

ACKNOWLEDGMENTS

We have benefited greatly from the comments of many colleagues including B. Albrecht, A. Arakawa, A. K. Betts, J. W. Deardorff, J. Hack, D. Lenschow, D. K. Lilly and P. Silva Dias. We are also indebted to Dorothy Chapman and Sandra Wunch for their help in preparing this paper. The research reported here has been supported by the GARP Section of the Office of Climate Dynamics, National Science Foundation, Grants ATM 76-09370 and OCD 74-21678.

REFERENCES

Albrecht, B.A., 1977: A time-dependent model of the trade-wind boundary layer. Ph.D. Dissertation, Department of Atmospheric Science, Colorado State University.

Arakawa, A., 1975: Modeling clouds and cloud processes for use in climate models. Report of the international study conference on the physical basis of climate modeling, Stockholm, 29 July - 10 August 1974. GARP Publication Series No. 16.

Arnason, G., R.S. Greenfield and E.A. Newburg, 1968: A numerical experiment in dry and moist convection including the rain stage. J. Atmos. Sci., 25, 404-415.

Betts, A.K., 1973: Nonprecipitating cumulus convection and its parameterization. Quart. J. Roy. Meteor. Soc., 99, 178-196.

Cole, J.D., 1968: Perturbation Methods in Applied Mathematics. Blaisdell Publishing Co., Waltham, Massachusetts, 260 pages.

Cox, S.K., 1973: Infrared heating calculations with a water vapor pressure broadened continuum. Quart. J. Roy. Meteor. Soc., 99, 669-679.

Deardorff, J.W., 1974a: Three dimensional numerical study of the height and mean structure of a heated planetary boundary layer. Boundary-Layer Meteorology, 7, 81-106.

_____, 1974b: Three dimensional numerical study of turbulence in an entraining mixed layer. Boundary-Layer Meteorology, 7, 199-226.

_____, 1976: On the entrainment rate of a stratocumulus-topped mixed layer in a strong inversion. Quart J. Roy. Meteor. Soc., 102, 563-582.

Flohn, H., M. Hantel and E. Ruprecht, 1968: Air-mass dynamics or subsidence processes in the Arabian Sea summer monsoon? J. Atmos. Sci., 25, 527-529.

Gunther, E.B., 1977: Eastern north Pacific tropical cyclones of 1976. Mon. Wea. Rev., 105, 508-522.

Japanese Oceanographic Group, 1975: Outline of oceanographic conditions in AMTEX '74 and AMTEX '75. Scientific Report of the Fourth AMTEX Study Conference (AMTEX Report No. 8).

Kraus, E.B., 1968: What do we not know about the sea-surface wind stress? Bull. Amer. Meteor. Soc., 49, 247-253.

LaViolette, Paul E., 1974: A satellite-aircraft thermal study of the upwelled waters off Spanish Sahara. J. Phys. Oceanogr., 4, 676-684.

REFERENCES (Continued)

Leetmaa, A., 1972: The response of the Somali Current to the southwest monsoon of 1970. Deep Sea Res., 19, 319-325.

LeMone, M.A., and W.T. Pennel, 1976: The relationship of trade wind cumulus distribution to subcloud layer fluxes and sturcture. Mon. Wea. Rev., 104, 524-539.

Lenschow, D.H., 1972: The Air Mass Transformation Experiment (AMTEX). Bull. Amer. Meteor. Soc., 53, 353-357.

_____, 1973: Two examples of planetary boundary layer modification over the Great Lakes. J. Atmos. Sci., 30, 568-581.

_____, and E.M. Agee, 1976: Preliminary results from the Air Mass Transformation Experiment (AMTEX). Bull. Amer. Meteor. Soc., 57, 1346-1355.

Lilly, D.K., 1968: Models of cloud-topped mixed layers under a strong inversion. Quart. J. Roy. Meteor. Soc., 94, 292-309.

Management Committee for AMTEX, 1976: AMTEX '75 Data Report. Volume 2, Aerological Data. [Available from D.H. Lenschow, National Center for Atmospheric Research, Boulder, Colorado].

Miller, D.B., and R.G. Feddes, 1971: Global atlas of relative cloud cover 1967-1970. Joint production by U.S. Dept. of Commerce and U.S. Air Force, Washington, D.C. [Available from NTIS, Springfield, Va., AD739 434].

Miller, F.R., and M.R. Stevenson, 1974: Comparison of cloud top temperatures from satellites and sea surface temperatures along Baja California. Paper presented at V Congreso Nacional de Oceanografia, October 1974. [Available from the authors at Scripps Institution of Oceanography, LaJolla, California].

Neiburger, M., D.S. Johnson and C.W. Chien, 1961: Studies of the structure of the atmosphere over the Eastern Pacific Ocean in summer, I: The inversion over the Eastern North Pacific Ocean. Univ. of Calif. Publ. Meteor., 1, No. 1.

Ninomiya, K., 1975: Large-scale aspects of air mass transformation over the East China Sea during AMTEX '74. J. Meteor. Soc. Japan, 53, 285-303.

_____, 1976: Note on synoptic situation of AMTEX '75. J. Meteor. Soc. Japan, 54, 334-337.

Nitta, T., 1976: Large-scale heat and moisture budgets during the Air Mass Transformation Experiment. J. Meteor. Soc. Japan, 54, 1-14.

REFERENCES (Continued)

Ogura, Y., and N.A. Phillips, 1962: Scale analysis of deep and shallow convection in the atmosphere. J. Atmos. Sci., 19, 173-179.

Paltridge, G.W., 1974: Infrared emissivity, shortwave albedo and the microphysics of stratiform water clouds. J. Geophys. Res., 79, 4053-4058.

Pennel, W.T., and M.A. LeMone, 1974: An experimental study of turbulence structure in the fair weather trade wind boundary layer. J. Atmos. Sci., 31, 1308-1323.

Platt, C.M.R., 1976: Infrared absorption and liquid water content in stratocumulus clouds. Quart. J. Roy. Meteor. Soc., 102, 553-561.

Ramage, C.S., 1966: The summer atmospheric circulation over the Arabian Sea. J. Atmos. Sci., 23, 144-150.

Randall, D., 1976: The interaction of the planetary boundary layer with large-scale circulations. Ph.D. Dissertation, Department of Meteorology, University of California at Los Angeles.

Riehl, H., T.C. Yeh, J.S. Malkus and N.E. LaSeur, 1951: The northeast trade of the Pacific Ocean. Quart. J. Roy. Meteor. Soc., 77, 598-626.

Schubert, W.H., 1976: Experiments with Lilly's cloud-topped mixed layer model. J. Atmos. Sci., 33, 436-446.

Steiner, E.J., and W.H. Schubert, 1977: Stratocumulus convection off the west coast of South America. Atmos. Sci. Paper 270, Colorado State University, 97 pages. [Available from Department of Atmospheric Science, Colorado State University, Fort Collins, Colorado 80523].

Trewartha, G.T., 1961: The earth's problem climates. University of Wisconsin Press, Madison, Wisconsin, 334 pages.

_____, 1968: An Introduction to Climate. McGraw-Hill Book Company, 408 pages.

U.S. Dept. of Commerce, Weather Bureau, 1959: World Weather Records, 1941-50. U.S. Government Printing Office, Washington, D.C.

U.S. Dept. of Commerce, Environmental Science Services Administration, Environmental Data Service, 1968: World Weather Records, 1951-60. U.S. Government Printing Office, Washington, D.C.

U.S. Dept. of Commerce, Environmental Science Services Administration, Environmental Data Service, 1967-70: Climatological Data, National Summary. U.S. Government Printing Office, Washington, D.C.

REFERENCES (Continued)

U.S. Naval Weather Service, 1969: World-wide airfield summaries. Volume VIII, Part I - United States of America. [Available from NTIS, Springfield, Va., No. AD 688 472].

Wakefield, J.S., and W.H. Schubert, 1976: Design and execution of the marine stratocumulus experiment. Atmos. Sci. Paper 256, Colorado State University, 74 pages. [Available from Dept. of Atmos. Sci., Colorado State University, Fort Collins, Colorado 80523].

Warren, B., H. Stommel and J.C. Swallow, 1966: Water masses and patterns of flow in the Somali Basin during the southwest monsoon of 1964. Deep Sea Res., 13, 825-860.

BIBLIOGRAPHIC DATA SHEET	1. Report No. CSU-ATSP-273	2.	3. Recipient's Accession No.

4. Title and Subtitle

Marine Stratocumulus Convection

5. Report Date: July 1977

6.

7. Author(s) Wayne H. Schubert, Joseph S. Wakefield, Ellen J. Steiner, Stephen K. Cox

8. Performing Organization Rept. No. 273

9. Performing Organization Name and Address

Department of Atmospheric Science
Colorado State University
Fort Collins, Colorado 80523

10. Project/Task/Work Unit No.

11. Contract/Grant No. ATM 76-09370

12. Sponsoring Organization Name and Address

National Science Foundation

13. Type of Report & Period Covered

14.

15. Supplementary Notes

16. Abstracts

Large areas of persistent low level marine stratocumulus clouds occur primarily over the cool eastern oceans in the strong subsidence to the east of the subtropical oceanic high pressure cells. The climatology of these areas is reviewed, after which we present a coupled convective-radiative boundary layer model of such stratocumulus convection. The model is a slight generalization of the cloud-topped mixed layer model of Lilly (1968). Assuming horizontally homogeneous steady state conditions we first investigate the dependence of the model variables on the large-scale divergence and sea surface temperature. Next, assuming horizontally inhomogeneous conditions we investigate by numerical integration the downstream variations which occur as boundary layer air flows through regions of varying divergence and sea surface temperature. In addition, approximate analytic solutions are given. Finally, the design of an observational program to more completely test the theory is briefly discussed.

17. Key Words and Document Analysis. 17a. Descriptors

Boundary Layer
Cloud-topped Mixed Layer
Marine Layer
Marine Stratocumulus
Mixed Layer
Stratocumulus
Stratus

17b. Identifiers/Open-Ended Terms

17c. COSATI Field/Group

18. Availability Statement

19. Security Class (This Report) UNCLASSIFIED

21. No. of Pages 140

20. Security Class (This Page) UNCLASSIFIED

22. Price